UC Berkeley
UC Berkeley Electronic Theses and Dissertations

Title
Engineering Collective Behaviors

Permalink
https://escholarship.org/uc/item/84k6p2fw

Author
Cohen, Daniel Joseph

Publication Date
2013

Peer reviewed|Thesis/dissertation

Engineering Collective Behaviors

by

Daniel Joseph Cohen

A dissertation submitted in partial satisfaction of the

requirements for a degree of

Joint Doctor of Philosophy

with the University of California, San Francisco

in

Bioengineering

in the

Graduate Division

of the

University of California, Berkeley

Committee in charge:

Professor Michel M. Maharbiz, Chair
Professor Tejal Desai
Professor Evan Variano

Fall 2013

Engineering Collective Behaviors

Copyright 2013

by

Daniel Joseph Cohen

Abstract

Engineering Collective Behaviors

by

Daniel Joseph Cohen

Joint Doctor of Philosophy
with the University of California, San Franicsco in Bioengineering

University of California, Berkeley

Professor Michel M. Maharbiz, Chair

Much of the world consists of many small things, animate or inanimate, interacting with each other to produce something larger than, and different from themselves. Comprising murders of crows, armies of ants, schools of fish, dunes of sand, and various organs in your body, the collective behaviors of these systems embody a different approach to engineering than we currently employ. This thesis explores three examples where principles from collective behaviors are deployed as engineering tools. The first example presents how the collective phenomenon of 'percolation' can be leveraged to rapidly produce a low-cost, best-in-class strain gauge (100% strain with a linear output and gauge factor of 1) using collectives of carbon nanotubes. The second example discusses how a modified inkjet printer can be used to simulate morphogenetic inputs and thereby manipulate the spatiotemporal patterns of gene expression in bacterial colonies. The final example explores control of collective motion (canonical 'swarming') through the use of bioelectric cues to herd epithelial cells in a manner analogous to how a sheepdog herds sheep.

ACKNOWLEDGEMENTS

"I don't know half of you half as well as I should like; and I like less than half of you half as well as you deserve."[1]
After much contemplation, I believe both parts of this to be compliments, and I intend them as such, although you may interpret them however you wish. Let the bestowing of gratitude commence.

To the National Science Foundation's Graduate Research Fellowship and the ASEE's NDSEG fellowship—I was extraordinarily fortunate to have been collectively funded by these organizations for nearly my entire Ph.D. This was a wonderful opportunity as it allowed me to pursue my own areas of interest and I am thrilled that society values science enough to provide such opportunities.

Michel Maharbiz—I appreciate having had the complete independence to roam across any and every field that struck my fancy. It was invaluable, and a choir of homunculi shall forever sing your praises. I also appreciate being able to discuss any and every field, from Samarkand to CERN. We had fun, and will hopefully continue to do so. Perhaps we will complete the thousand-and-one-cell-dream-machine some fine day when the apricots come.

Steve Conolly—I don't know how you put up with my constant visits and 'groupie status', but I'm exceedingly grateful. Your input, support, and friendship were integral to my trajectory. Like a good magnet, you draw people in need and help them out.

Bob Full—Many thanks for the advice, pokes, and prods that oriented me in the right direction. I'm graduating, so it looks like they worked out. However, don't think you've escaped my pestering and crazy ideas.

James Nelson—Our serendipitous meeting and your timely advice delivered over a barbecue changed my course. Of the two things you told me I needed, I think that covers the 'epiphany' part. For the other part, you walked right into that one, and I'm exceptionally glad that you did. Onwards and upwards.

To my friends in and out of lab—including: Tim, John, Deb, Eric, Patrick, Frankie, Kyle, David, Alba, Carolina, and those of you who know you should be on this list—I got by with *a whole lot* of help from my friends, as the song should have said. You gave me homes and labs away from home/lab, enabled all my nefarious experiments, and ensured that I never felt alone. I can't thank you enough, and I wouldn't have finished without you. Imagine me saying that while tearing up and wearing dinosaur slippers and you'll get the picture.

To my lab(s)—you guys were great—emotional support, scientific support, imbibing support, etc. I am still amazed that you tolerated my messy experimental practices with nary a peep. Tweezer-Thief, I absolve you of your misdeeds. Tape-thief, you must find someone else's yellow tape on which to prey.

---

[1] Bilbo on the occasion of his 111th birthday

To the piratical lagomorphs

"The fox knows many things, while the hedgehog knows one, big thing."
-Archilochus

Contents

Chapter 1
Introduction to Collective Behaviors

"Ex pluribus unum facere"
From many is made one

1.1 The Birds and the Bees

What do percolating carbon nanotubes, bacterial colony genetics, collective cell migration, flocking birds, swarming bees, marching penguins, ant colonies, neurons, and the culture of major cities have in common? That's right: they are each examples of **collective behaviors** (and the first three happen to be the primary focus of this thesis). The salient characteristics of these collectives—the agility of flocking birds, the 'swarm intelligence' of bees and ants, consciousness resulting from neuronal communication, and so forth—are examples of a phenomenon called emergence. Ephemeral, elusive, and aesthetic, emergence itself can crudely be defined as describing how interacting "parts" give rise to a collective "whole" with new properties distinct from those of the parts. Collective behaviors are coming to be recognized as potent engineering tools— the exploration of which forms the basis of this thesis. Collective behaviors in natural systems typically involve self-organization across multiple length-scales, resulting in the sophisticated behaviors seen in natural systems. Insights into these systems (e.g. the idea of the 'Swarm') have enabled advances spanning data technology, transportation, robotics, healthcare, materials science, urban planning, and more[1–3].

As we come to better understand the underlying principles of emergent behaviors, we will improve our ability to leverage them as engineering tools. This field of "collective engineering" is nascent, but even now it is clear that opportunities abound across disciplines if we incorporate this incongruous engineering paradigm into our traditional design approaches. At its core, this thesis represents an exploration of three different aspects of collective engineering where the collective properties of aggregates were used to enable assorted engineering goals. Before addressing these, we must first attempt to clarify terminology, as our long history of grappling with the ideas of emergence and collective behavior has muddied the waters. The remainder of this chapter will discuss this, briefly explore some of the history and philosophical issues at hand, and discuss how collective methods have been, and can be, incorporated into our engineering practices.

1.2 Collectivity: Context and Controversy

1.2.1 Definitions and terminology

Despite the obvious aesthetic qualities of many collective behaviors (e.g. flocking birds), actually defining complexity and emergence is a surprisingly controversial undertaking as there are many schools of thought and schisms in play. While I would prefer to avoid all mention of it here, it has become such a common term these days that there is now backlash against its use, and it seemed best to tackle it head on. **At the heart of the idea of emergence is Aristotle's famous statement: "*The whole is something over and above its parts, and not just the sum of them all....*"**[4] However, actually rooting the concept in a clearer formal definition has resulted in tremendous confusion, controversy, and criticism. The situation was so fraught with controversy a decade ago that an editorial in *Science* described the whole endeavor of defining emergence and complexity as entering a "terminological minefield"[5]. A term that often comes up in discussions of

defining emergence is that it is **ostensively defined** [6,7]. In straightforward terms, an ostensive definition is what happens when an adult defines a dog to a child by pointing at a dog and saying "that is a dog." We may not be very good at defining emergence, but we certainly know it when we see it.

1.2.3   The criteria for collective behaviors

Given the rhetorical delicacy required here, the work described in this thesis will speak exclusively of 'collective behaviors'; their emergence status being left as an exercise for the reader. I have also cobbled together fragments of definitions of emergence, complexity, spontaneous order, and the like to create a blueprint of sorts that lays out the key criteria underlying the collective behaviors we will be discussing.

<u>**Basic criteria for collective behaviors**</u>
(inspired by Goldstein)

i.   *A collective system consists of **many** interacting, individual 'agents' (atoms, cells, birds, humans, etc.) who exhibit some set of neighbor interactions.*

In simple terms, agents are the individual components whose components will interact. Spatially, agents all have neighbors, and neighbors are typically discussed in terms of their proximity—the Nth nearest neighbor, etc. The most important detail to bear in mind is that, as far as collective behaviors are concerned, the internal workings of agents are not intrinsically interesting, nor are individual agents valuable. Rather, only interactions amongst neighbors are important. This begs the question of "how many agents are enough?" While there are quantitative methods that can help answer this, most scenarios rely on some sort gestalt assessment based on how much complexity exists in the system. For instance, in the case of interacting cells, 2-3 are not considered sufficiently complex to afford true collective behavior, but a sheet of several hundred cells is considered sufficiently complex [8].

ii.   *Collective behaviors occur at the global (population) level but derive from local interactions amongst agents executing prescribed behaviors.*

The salient characteristic of any collective system is how the individual agents comprising it interact with each other—this is called **coupling**. This can be qualitatively understood via some canonical examples. When birds flock, they specifically track their relative position to other birds in terms of how many neighbors they can see in a given direction (*not* in terms of physical distances). In the case of starlings, the critical number of neighbors a bird tries to see in any given direction happens to be 7 [9,10]. Hence, flocking birds are coupled by data obtained from visual perception and follow a neighbor-tracking rule. Cells within epithelial sheets, by contrast, are mechanically attached (coupled) to each other. This means that the dominant neighbor interaction boils down to local forces

experienced between cells and their immediate neighbors[11–14]. However, despite the immediacy of the interactions, long-range interactions spanning large groups of cells still emerge at a population level. Given any collective system, it is the coupling behavior that ultimately converts local interactions into coordinated, global behavior.

iii. *Collective behaviors themselves typically do not intuitively follow from understanding the workings of agents in isolation.*

The primacy of coupling and interaction amongst agents over the properties of agents themselves has two, key implications.

1. **Collective systems can be quantified and described without fully understanding the internal properties of an individual agent.** Essentially, we can analyze bulk behavior without inherently needing to know what is going on beneath the surface.

2. **Even if we did fully understand the inner workings of an agent, that knowledge may not obviously help us predict collective behavior.** For instance, knowing everything about how a bird 'works', down to the neuronal level may still not lead us to conclude that birds will flock. For a start, the relevant data (the visual perception limit, etc.) would simply be lost in the noise (everything else about how birds work). More importantly**, knowing how an individual agent works in *isolation* still does not guarantee that we will ask the right questions about how agents interact *collectively*.**

1.3   The scope of this dissertation

There are a variety of reasons why collective engineering is such a young field (definitional difficulties not withstanding). For a start, until relatively recently, we have lacked the analytical tools and computational power to properly study the phenomena, and lack of these tools slowed our acquiring the mindset needed to ask the right questions. By way of example, consider the starling example discussed earlier. At the start of the 20th century, despite having the statistical mechanics tools to begin to think about bird flocking, it was still the province of amateurs. Most notable was Edmund Seluous, who declared that flocking was too sophisticated a behavior to rely on anything other than "thought transference," by which he meant telepathy[15]. While this did not become a mainstream idea, it highlights the level of confusion at the time. What eventually became the mainstream idea was that flocking clearly involved some form of position control, in much the same way that human drivers attempt to regulate the distance between themselves and neighboring cars. This idea became so entrenched that it took the landmark starling paper of 2008 to debunk it. Enabled by full, digitized 3D video of starling flocks with individually tracked birds, the researchers were finally able to quantitatively test the distance hypothesis. It turned out to be false, and they were able to demonstrate that starlings perceive a 'topological' rather than 'metric' distance

in the flock, meaning that they track the number of *visible neighbors* rather than the physical distance to a neighbor.

The point of this story is to emphasize just how recent our abilities to start exploring these multi-agent systems are. This also explains why the majority of research applications to date have targeted relatively few areas: robotics, artificial intelligence and software technology, and so-called "big-data" methods. Ironically, despite the prevalence of collective behaviors in biological systems, only ~4% of the total publication output of engineering and biotechnology research in the last 50 years has applied these principles to engineering biological systems (via ISI database statistics). Nonetheless, given our rapidly growing knowledge and abilities and the power and potential of engineering systems capable of self organization and regulation, it is likely that we begin to incorporate collective engineering principles into more and more aspects of engineering.

Given all of this, the purpose of this thesis is to present three examples of using collective engineering motifs for applications outside of the areas common today. First, we will explore a simple example of how collectivity enables the design of robust, stretchable electrodes that can be incorporated into a new class of highly elastic strain gauge. Next, we will look at how we can tap into an existing biological control mechanism in bacteria using a tool that enables spatiotemporal regulation of genetic activity across a population of cells. Finally, we demonstrate how principles of collective engineering can be used 'herd' tissues and manipulate their migration.

Chapter 2
Leveraging percolation in carbon nanotube collectives to build highly elastic strain sensors

"Our name is Legion, and we are Many."
-Daniel Defoe on the power of standing together (1701)

Chapter Overview

The intent of this chapter is twofold: (1) to present a simple and intuitive case study in collective engineering applied to solving a classic problem in strain sensor design, and (2) to assist and encourage researchers who are new to the field of carbon nanotubes and stretchable sensors in beginning to explore and prototype nanotube-enabled devices and materials. The underlying case study here is the design of a new class of strain gauge capable of reliably transducing strains up to 20X larger than the best contemporary strain gauges. This is a perfect application for collective engineering because the solution presented here relies on a simple emergent behavior known as **percolation** to produce robust, strain-resistant electrodes. Moreover, such sensors (and a variety of others) can be built using 'off-the-shelf' components and equipment, making it suitable as a springboard for researchers who are new to the fields of collective- and nano-engineering. We will begin with an overview of the challenges of sensing large strains and the limitations of status quo devices. Armed with that knowledge, we will then discuss why carbon nanotube percolation is particularly well suited to address the problem, along with how to acquire, prepare, and post-process carbon nanotubes into a sensor. Finally, we will present the full sensor design based on piezocapacitive transduction between percolating electrode plates.

2.1   The challenge of gauging large strains in soft substrates

For decades, the fundamental tool for measuring strain has been the piezoresistive strain gauge. Its simplest form, as shown in Figure 1 (left), is comprised of a rigid, polymeric substrate (such as mylar) onto which has been patterned a thin, metallic, serpentine wire, over which a second polymeric shielding layer is placed. The mechanism of operation is straightforward. First, the sensor is aligned with the direction strain to be monitored in the sample (such as a bridge stay), and then it is rigidly adhered to the substrate. The strength and rigidity of the adherent is selected so as to ensure that any strain in the underlying substrate is directly transmitted to the gauge itself. This planar, uniaxial strain serves to stretch the serpentine wire of the gauge (Fig. 1, right), and thereby increase the resistance of the strain gauge according to Equation 1. The effect of resistance scaling with strain is known as *piezoresistance* and is the fundamental basis of nearly all modern planar strain gauges. Such a gauge is monitored and calibrated using a Wheatstone resistor bridge, and the efficiency of the gauge is measured with respect to the so-called *gauge factor* (*GF*, Equation 2), which is a measure of the percentage change in resistance of the gauge relative to the actual strain it experienced. Gauge factors can be calculated for any arbitrary strain gauge mechanism by taking the ratio of the percentage change in the transduction variable (resistance, capacitance, voltage, etc.) and normalizing by the applied strain. As they are non-dimensional, gauge factors can be compared across different sensors to give a rough sense of the sensitivity, with higher gauge factors connoting increased sensitivity. For reference, most metallic strain gauges have gauge factors ranging from 2-6 [1], while semiconducting strain gauges (relying on a different piezoresistive mechanism) can reach gauge factors of over 100. While a high gauge factor is theoretically desirable, it is a mistake to pick a strain gauge based solely on the gauge factor. Instead, application-specific constraints must be considered. For instance, while semiconducting gauges are sensitive, they typically cannot tolerate strains over 0.05%, nor are they linear over their entire strain range, meaning calibration becomes complicated.

Moreover, sensitivity becomes less important as the magnitude of the strain to be measured increases—the ability to detect a 0.05% strain is only important for micro-strain applications and loses all value for large strains (>1%).
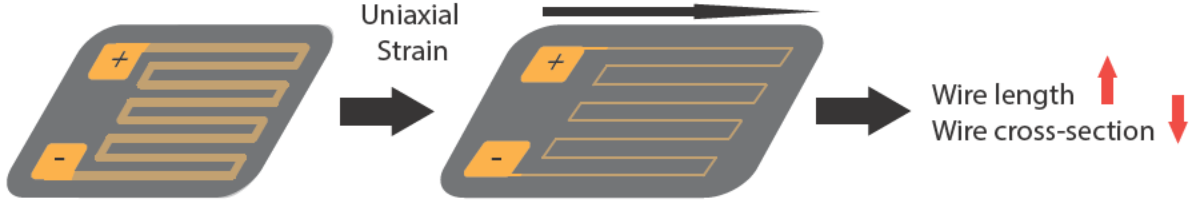
Figure 1: Piezoresistance strain gauge mechanism
Representation of metallic strain gauge with a polymeric backing layer on which a fine metallic serpentine trace has been deposited. Axial strain causes the fine traces to both lengthen and contract in cross-section; both effects serve to increase resistance (see Eqn. 1). Here, N is the number of the long sections in the serpentine, ρ is the resistivity of the metal, L is the length of each long section, A is the cross-section, and ε is the applied strain.

$$R_{strained} = N\rho\left(\frac{L + \Delta L}{A - \Delta A}\right) \qquad (1)$$

$$GF = \frac{\Delta R/R}{\varepsilon} \qquad (2)$$

Given these caveats, metallic strain gauges have become ubiquitous for basic strain monitoring in rigid substrates as they offer a linear output over their entire working range and rigid substrates rarely experience strains beyond the strain limit of metallic gauges (<5%). However, they are phenomenally ill-suited for monitoring soft substrates and large strains. This problem arises directly from the design of the metal foil gauge where both the yield strains (the maximum strain after which a material can elastically recover) of the metal electrodes and the polymeric backing layer are relatively low, contributing to the maximum measurable strain of <5% [1, 2]. Moreover, the material of the gauge itself can be stiffer than that of the substrate being monitored, resulting in local stiffness reinforcement of the substrate that skews the data. Overall, this is a major limitation in the fields of biomechanical monitoring, medical devices, and soft robotics, where large, biologically relevant deformations are typical and the substrates themselves are often both less stiff than traditional sensors and subjected to relatively large strains. For example, many muscles experience contractile strains of at least 25%, while bio-inspired robotics systems increasingly rely on high-strain linkages, compliant joints, and tactile interfaces [3–8]. In order to monitor such systems, both a softer sensor backing layer and a much more resilient electrode material are necessary. Further, as we continue to explore the potential of wearable electronics and mobile health, there should be a growing demand for sensors and devices that move and deform with the body.

2.2   Soft sensor design: Percolation and carbon nanotube electrodes

The first problem in designing a stretchable sensor is to select something that can easily strain at least as far as the sample in question and is close enough to the stiffness of the sample to minimize stress shielding. Given this, the material of choice in most cases tends to be some form of silicone rubber. Biocompatible, inexpensive, highly tunable, and moldable, silicone rubbers are typically ~ 1000X less stiff than the mylar backing found in traditional metal strain gauges, and exhibit yield strains in excess of 100% [9]. As such, silicone is one of the most common substrates used for stretchable strain gauges. The next problem is selecting and incorporating an electrode material with the silicone in order to produce a strain gauge, and the key here is finding an electrode material that is robust under strains larger than 5%, and the key to this constraint appears to lie in the phenomenon of *percolation.*

Formally described as a 'first-order emergent structure arising from shape-interactions amongst agents', percolation describes the connectivity networks that arise in a collection of particles. In other words, as particles are aggregated together, they will begin to overlap. Above a critical density of particles (the **percolation threshold**), this overlapping emerges across the entire collective of particles, meaning that any point in the collective can now be connected to any other point via a chain of contiguous particles. If a percolating network experiences strain, the agent-agent contacts will alter slightly, but the network overall will remain intact. When using electrically conductive particles above the percolation threshold, the resulting network ensures that there is always some contact or overlap between the particles to ensure that conductivity is maintained, even during deformation of the network, although conductive particle densities below the percolation threshold will exhibit no conductivity. The simple model for this type of behavior follows a split-function power-law, as shown in Eqn. 3

$$\sigma = \begin{cases} \sigma_o(\rho - \rho_c)^s & if \ \ \rho > \rho_c \\ 0 & if \ \ \rho < \rho_c \end{cases}$$

(3)

Here, *s* is the conductivity of the system and s_o is the baseline conductivity. The area or volume fraction of the particles is represented by ρ, while ρ_c is the actual percolation threshold, above which conductive networks are capable of forming, giving rise to true percolation. The exponent, *s*, is the critical exponent that controls the scaling rate. We can visualize this in Fig. 2a, where the plot represents the theoretical conductivity of a nanotube percolation network as a function of the space-filling fraction of nanotubes (ρ) with a percolation threshold of $\rho_c = 0.5$ [10, 11].

In practice, percolation efficiency depends strongly on both the baseline conductivity and the aspect ratio of the particles in the network, scaling directly the aspect ratio of the particles (length/width). As far as these parameters are concerned, carbon nanotubes make excellent percolation particles, possessed of both aspect ratios ranging from 100-1000X and high intrinsic conductivities. As a result of the ease with which

carbon nanotubes percolate, the requisite ρ_c is actually relatively low (often far lower than in the simulation in Fig. 2a). By comparison, traditional percolation networks made of pseudo-spherical particles (gold micro-plates and carbon black) cannot percolate as efficiently and exhibit much higher percolation thresholds than carbon nanotube networks [10, 12–19]. Carbon nanotubes' properties are derived from their structure, shown in Fig. 2b. The hexagonal lattice of carbon atoms affords exceptional mechanical properties and high conductivity, and favors particles that are longer than they are wide (high aspect ratio). Taken together these attributes make nanotubes excellent percolating agents.

This percolation efficiency is enormously important in device design for two key reasons. First, lower percolation thresholds reduce the cost of a device by reducing the amount of conducting particles needed, and also allow for transparent electrodes to be produced. A great deal of excellent work has been performed characterizing the applicability and spectral characteristics of nanotubes in transparent, stretchable electronics. While less electrically efficient than traditional transparent electrodes made from Indium-Tin-Oxide (ITO), they are considerably cheaper and can be stretched, something an oxide can never do [11, 20, 21]. Focusing on this stretchability, we see the second key attribute of nanotube percolation networks: strain resistance and piezoresistivity. Fundamentally, when carbon nanotube networks are stretched, they still maintain conductivity. From a binary perspective, percolating nanotube networks can undergo enormous strains (100%+) without losing conductivity. However, the trade-off is that stretching increases the contact resistance between adjacent nanotubes as they are pulled slightly apart from each other. This increased resistance manifests itself as piezoresistance [1, 11, 22] and is depicted in Fig 2c where we see a resting network strained laterally while still maintaining local connectivity (despite the resistance change). This attribute, while ultimately quite difficult to stabilize in nanotube networks, has been the dominant mechanism employed in both traditional metallic strain gauges and nanotube strain gauges. To provide context, the remainder of this section will discuss how such gauges are produced and perform, while Section 5 will explore the benefits of our alternative approach: piezocapacitance.

Typically, there are two main approaches that have been used to produce percolating carbon nanotube electrode networks—3D nanotube/polymer matrix composites and layer-based nanotube electrodes. The former methods are the earliest and a great deal of work has gone into optimizing the material properties of the resulting nanotube network. One of the first methods of this type relied on starting with a polymer matrix base and carefully dispersing carbon nanotubes into the unpolymerized base casting the resulting mixture into a desired shape, and then curing the ensemble [7, 22–27]. While this method can work quite well, it is nontrivial to reliably disperse nanotubes in a viscous prepolymer base without the use of probe sonication, homogenizers, and solvents [7]. Moreover, this method may also stiffen the resulting polymer due to the high percolation threshold concentration needed to obtain decent conductivity in the network [1]. In addition to requiring extended processing, the direct mixing approach also requires many more nanotubes to obtain proper percolation in three dimensions, and this drives the cost up. An alternative process involves infiltrating silicone prepolymer into vertically aligned forests of nanotubes [22, 28]. These methods are effective and can preserve nanotube alignment while maintaing conductivity. However,

they require a great deal of cleanroom processing and have not been demonstrated to be effective for transducing large strains.
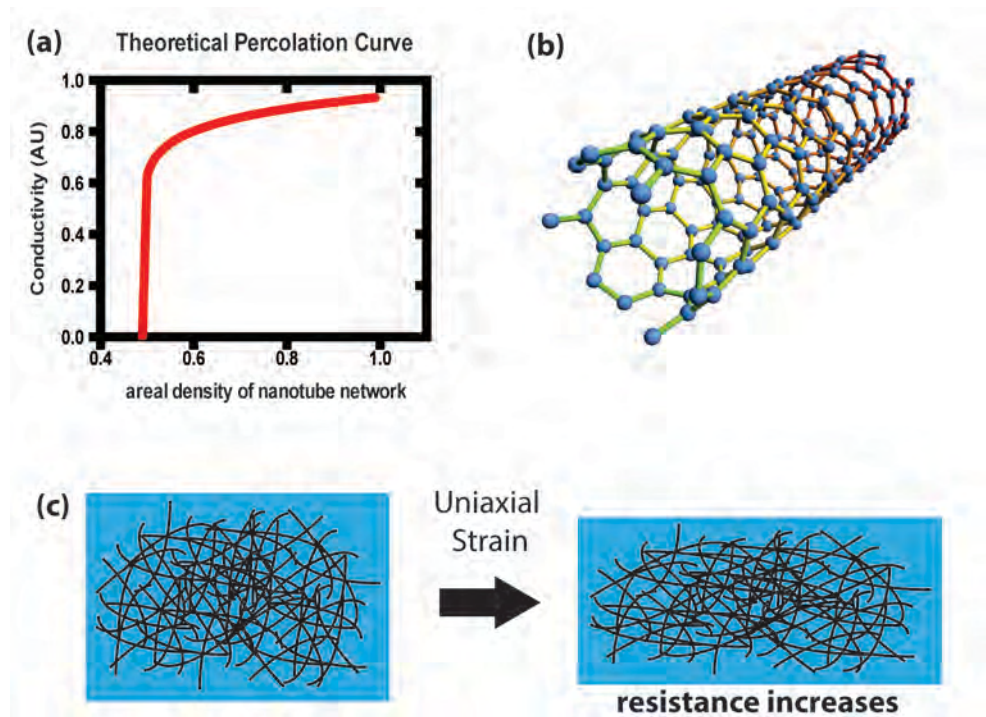
Figure 2: Nanotube percolation overview
(a) Simulated percolation network using the power-law fit and a percolation threshold of 50%. (b) Rendering of a single-walled nanotube to emphasize large aspect ratio (length/width) and the lattice structure (designed with Avogadro software). (c) Left shows a percolating network of nanotubes in a silicone matrix. It undergoes uniaxial strain that induces expansion in x and Poisson contraction in y resulting in a deformed nanotube network that still maintains conductivity while increasing the resistance.

Development of the layer-based percolation networks was driven largely by the transparent, stretchable electrode community as thin layers of nanotubes are relatively transparent and sustain stretching [11, 21, 29–34]. Here, such a layer of nanotubes is deposited on the surface of a sheet of elastomeric polymer and produces an electrode in much the same way that the deposited metal in a metallic strain gauge functions. Given this, much effort was directed at optimizing the percolation thresholds to reduce the number of nanotubes necessary for reliable conductivity while simultaneously improving transparency [11]. If transparency is not a requirement, the layering method becomes more straightforward as simpler deposition methods can be used to create the percolation network on the surface of the polymer. Typical techniques to produce nanotube layers comprise manual spreading of nanotubes, airbrushing a dispersion, silk-screening, polyelectrolyte layering, and vacuum filtration of a nanotube dispersion and subsequent transfer of the filtrate [1, 29, 32, 34–37]. This latter approach is both the fastest and most versatile (used both for transparent and general nanotube electrodes), and we chose to adopt and adapt it for the methods describes below.

2.3 Nanotube processing —selection, preparation, post-processing

For general stretchable sensors and many surface patterning applications, we have found that the layer-based method enabled by vacuum filtration and contact stamping is the simplest approach to produce electrodes or patterns of nanotubes on a planar, elastomeric surface. In brief, the method works as follows: acquire nanotubes and disperse them in water and surfactant (if necessary); vacuum filter the dispersion through a fine-pore filtration membrane; stamp-transfer the filtrate layer to a silicone substrate; encapsulate as necessary. The general process flow is presented in Figure 3, and the remainder of this section will address these steps in order.
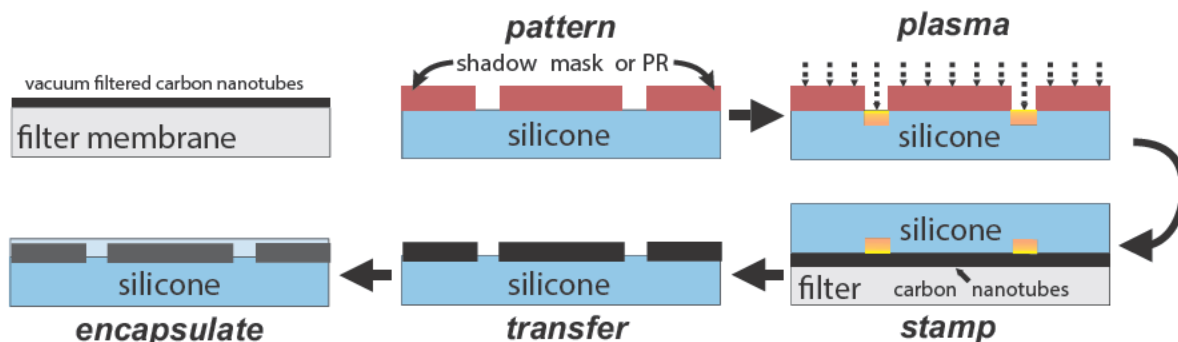
Figure 3: Process flow for patterning
(left to right) Nanotubes are first dispersed and vacuum filtered against a filtration membrane. During this process, the silicone substrate is cut and patterned with either photoresist or a sticker shadow mask. Once masked, the silicone is plasma treated to prevent nanotubes adhering to the treated regions. Post-plasma treatment, the mask is tripped and the silicone is stamped against the filtered nanotubes, in turn resulting in the specific transfer of nanotubes only to untreated regions. Post transfer, the nanotubes are encapsulated in a sprayed on silicone layer. *Adapted with permission from Cohen et al., Nano Letters (2012) American Chemical Society* [38]

2.3.1 Acquisition

Nanotubes have now reached the point of near ubiquity where reliable nanotubes can be purchased from online retailers such as Sigma and Cheaptubes.com. Moreover, for the work described herein, inexpensive, single-walled nanotubes from Cheaptubes were sufficient to achieve reliable performance. As application specific needs, such as number of walls, surface functionality, diameter vs. length, purity, etc. arise, the cost may increase, but basic nanotube research need not be expensive. By way of example, the nanotubes used in the case study below were ordered from Cheaptubes at $250/gram for 99% wt purity, 2 nm OD, 3-30 um long singlewalled carbon nanotubes. As the vacuum filtration protocol requires milligrams of nanotubes, a single purchase of stock will last for quite some time. The nanotubes we selected were chosen because we found that single-walled nanotubes transferred better than multiwalled nanotubes, and they had a high aspect ratio (length vs. diameter) of ~5000, which improves their

percolation performance. Figure 4 depicts a magnification sequence of images captured with scanning electron microscopy of these particular single-walled nanotubes.
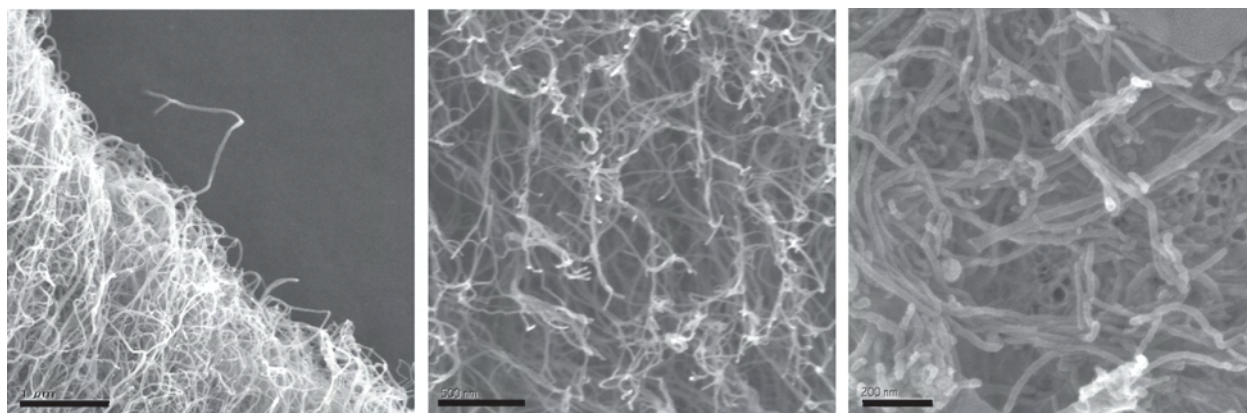
Figure 4: Scanning electron microscopy sequence of pre-fab nanotubes
(left) cluster of nanotubes, scale is 1 um; (center) zooming in, the interlocking network becomes clearer, scale is 500 nm; (right) zooming further we can see the individual tube structures (note the curvature), scale is 200 nm.

2.3.2   Pre-processing: dispersion

The vacuum filtration method relies on a relatively homogeneous distribution of nanotubes in the solvent (water). The single-walled carbon nanotubes in question are naturally hydrophobic and tend to aggregate and precipitate out of the solution without the aid of a surfactant or without first being surface functionalized. Typically, most vacuum filtration protocols begin by preparing a stock solution of no more than 5 mg/L of nanotubes in deionized, distilled water. To this solution, 1 g/mL of surfactant (SDS, Sigma) is added. The surfactant is essential for dispersion of the nanotubes, although it can later become a contaminant if care is not taken with the washing steps. *Proper ventilation should be used during the preparation of the solution to prevent inhalation of the nanotubes*. Once the solution is prepared, we treated it with bath sonication for 90-180 minutes and then allowed it settle overnight. Once treated, the dispersion should appear uniformly dark, although still partially transparent. The stability of the solution, and the need for surfactant and sonication, depends on the type of nanotube being used, with functionalized nanotubes offering greater stability in certain cases.

2.3.3   Vacuum filtration

The key step to this process is to prepare an apparatus capable of using a vacuum to draw the dispersion through a fine pore filtration membrane. Such systems can be purchased from companies such as Millipore, Sigma, and Whatman. We found that optimal performance came either from 220 nm mixed-cellulose-ester (MCE) filter membranes (MF Class, Millipore), or 20 nm anodic aluminum oxide filters (Anodisc, Whatman). As the latter are more expensive, fragile, and increase the filtration time significantly, the MCE filters should be tested first. The assembled filtration system is depicted in Figure 5a, where the solution reservoir sits upon the filter base, and this assembly in turn couples to two vacuum traps. Some form of vacuum trap is essential to

prevent the surfactant from excessively bubbling and going directly into the vacuum line. The volume of dispersed nanotube solution to use varies with the application and must be tuned in a case-specific manner. For the methods discussed here, we found 30 mL of solution to be optimal. During vacuum filtration, it is important to wash a significant amount of liquid through the filter to remove residual surfactant, and it is also essential not to let this added liquid agitate the freshly deposited nanotube layer. To handle this, we would filter the nanotubes until only a thin layer of liquid remained on the tubes and then very slowly and gently add 50 mL of fresh water down the side of the filtration reservoir to avoid damaging the nascent nanotube layer. Once the media has been exchanged, more water should be continually added until no surfactant bubbles are seen exiting the bottom of the filter (typically 500 mL of water). At this point, all liquid should be filtered out and the filter membrane should be removed and placed in a humidified Petri dish to await the transfer step. A representative filter disc post filtration is shown in Fig. 5b. In our experiments, we found that dry MCE filters tended to be less reliable during transfer than wet filters.

Figure 4: Filtration apparatus and representative samples
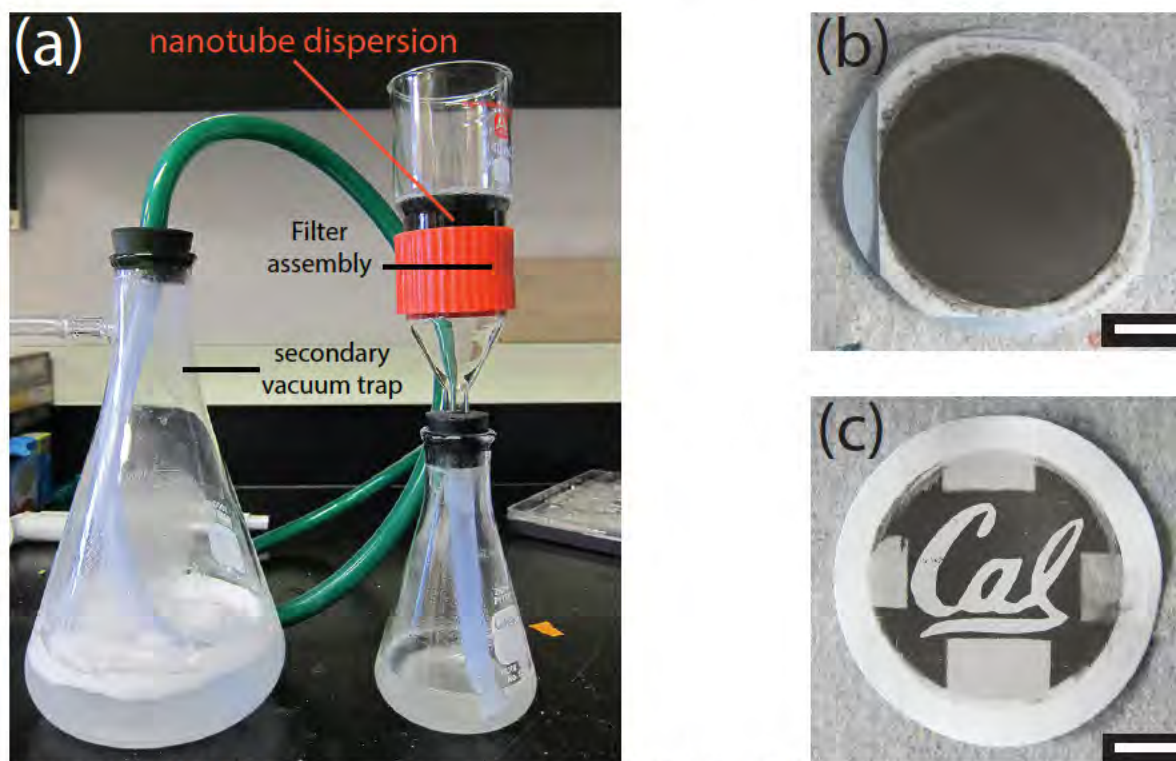(a) The vacuum filtration apparatus is shown using two vacuum traps, with the secondary trap useful for preventing surfactant bubbles from reaching the vacuum line. (b) What a filtration membrane looks like post-filtration with a gray layer of nanotubes atop it. (c) The negative pattern left after transferring the nanotubes to the target substrate. Scale bars are 0.75 cm.

2.3.4 Nanotube stamp transfer to silicone substrate

Once the nanotube filtrate layer has been produced, its role becomes similar to that of ink in traditional stamp transfer with the silicone substrate for the sensor playing the role of the paper. For simple applications where the geometry of the nanotube layer on the silicone is unimportant, the silicone can be directly stamped against the wet nanotube filtrate layer, and perfect transfer should occur, resulting in a semi-transparent, conductive layer of nanotubes on the surface of the silicone. While effective, this method affords no precision in the patterning process and is incompatible with techniques requiring any sort of specific geometry of patterning. To address this problem, previous studies have demonstrated that nanotubes can first be transferred to an intermediate, pre-molded polymer stamp that is then used to transfer the nanotubes to a fresh sheet of silicone [29, 39–42]. However, this method introduces an extra interface where transfer errors may occur, and so we have developed a simpler, faster method of direct transfer of high-resolution patterns.

Our method relies first on the fact that silicone can be converted between hydrophobic and hydrophilic surface properties through a brief exposure to atmospheric or oxygen plasma, and second on the native hydrophobicity of single-walled carbon nanotubes. In brief, we take a silicone substrate, mask the regions intended for nanotubes, expose the silicone to atmospheric plasma for 30 seconds in an inexpensive plasma cleaner (Harrick Plasma), strip the mask, and then stamp the plasma-treated silicone directly against the nanotube filtrate on the filter substrate. Using this protocol, we have observed nearly perfect transfer of nanotubes only to the untreated (hydrophobic) regions of the silicone substrates, as the examples in Figs. 5c and 6 demonstrate.

We begin by using pre-fabricated, ~250 um thick silicone sheeting (Bisco HT264, Stockwell Elastomers). While we have tested the method using traditional, hand-mixed silicone (Sylgard 184, Dow Corning), we have found that the Bisco silicone has more reliable and uniform mechanical properties for strain sensing than hand-mixed silicone. Moreover, pre-fabricated silicone sheets are much simpler to cut into customized dies using automated machines such as a laser cutter (VLS2.3, ULS, Inc.) or an inexpensive vinyl cutter (300 micron resolution Cameo Cutter, Silhouette, Inc.). These machines were used to produce the dogbone patterns presented in the case study. With respect to masking, there are two methods—one rapid and with coarse resolution, and the other lengthy but more precise.

> *Rapid, coarse patterning:* The simple, rapid method relies on using sticker paper to make a custom mask that is stuck to the silicone to maintain local hydrophobicity. Stickers were cut using either a laser or vinyl cutter. While resolutions can be obtained down to 300 microns, the ease of placing the sticker by hand depends on the complexity of the pattern. Features down to 1 mm rarely pose a problem, but smaller features require empirical testing to determine if it is possible to achieve the appropriate alignment by hand. Fig. 6a demonstrates a typical pattern from this method, while Fig. 5c shows the negative pattern left behind on the filter post-transfer. Overall, this method is the most versatile, as even hand-cut stickers can make effective masks.

> *Slow, fine patterning:* For features down to 100 um, we recommend photolithography. Specifically, we spin-coated S1818 positive photoresist (500

rpm/5 sec and 4000 rpm/30 sec) directly onto our silicone substrates, performed a 2.5 min soft-bake at 115 °C and then exposed the photoresist to 65 mJ/cm^2 I-line UV. Post-exposure was performed in CD-30 for 45 seconds. Once masked, the samples were then exposed to plasma and immediately washed with acetone post-plasma and prior to stamping against the nanotube substrate. Features down to 100 microns are achievable using this method, although it does require more specialized equipment and time. Figs. 6b/c present two complimentary patterns resulting from this method.

2.3.5   Stabilizing and encapsulating the nanotube layer

Stamp transfer methods require uniform pressure all across the stamp and the substrate, and we attempted to control this using two methods. Both methods begin by taking freshly plasma-treated silicone and gently reversibly adhering it to a glass slide. The slide was then placed silicone side down against the nanotube filtrate on the filter. Following this, we used a flat aluminum plate to help apply even pressure across the surface. For repeatability, we used a hydraulic press set at 0.25 MPa, although this is not strictly necessary. In the procedure described in the case study, we needed to coat both sides of a silicone sheet with different nanotube patterns, so we masked the silicone using sticker sheets on either side, plasma treated both sides simultaneously, and then performed the aforementioned stamping steps on both sides, serially, taking care not to damage the layers post-stamping. Contact with the glass stabilizer did not appear to modify the hydrophobicity, and both surfaces appeared to have transferred properly.

Sticker mask patterning   Photolithographic (positive)   Photolithographic (negative)
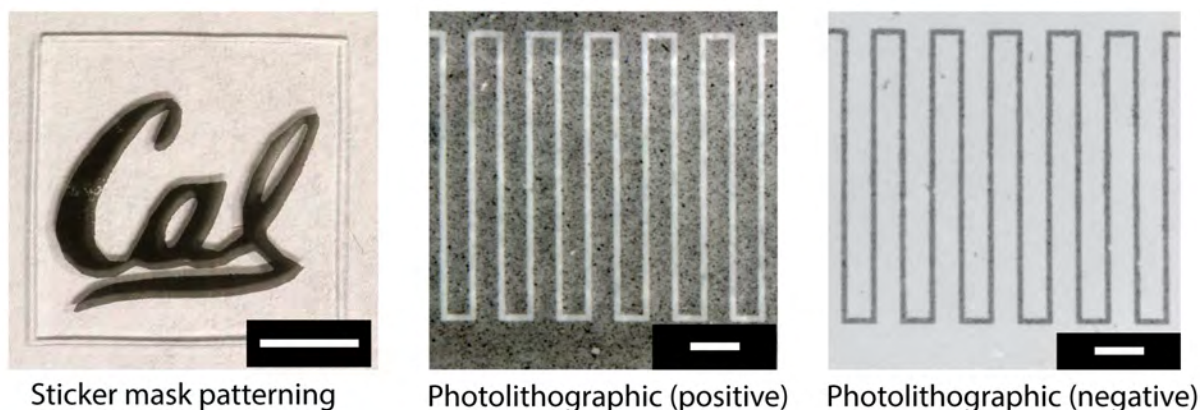
Figure 6: Results of patterning
(left to right) 'Cal' logo was produced using a sticker mask. Blurring is due to shadowing from the nanotube layer, and scale bar is 7.5 mm. The two rightmost images were made from the same filter—one is the negative of the other, and the scale bars are 750 um. *Adapted with permission from Cohen et al., Nano Letters (2012) American Chemical Society* [38]

Once the nanotubes are safely transferred to the silicone substrate, it may be desirable to encapsulate the layer to protect it. While many methods exist to do this, we opted to use a spray-based method where Sylgard 184 silicone is mixed in a 10:10:1 ratio of hexane, silicone, and curing agent, and subsequently loaded into an airbrush. The sample to be encapsulated can be safely taped against a new glass slide to protect both

the nanotube layer and any regions that need to make electrical contact post encapsulation. This slide is then heated on a hotplate at 110 °C. Once heated, the diluted silicone is sprayed against the exposed nanotube/silicone. Hexane is highly volatile is almost entirely gone by the time it reaches the surface, where the high heat serves to drive off any residual hexane while simultaneously curing the silicone. This method produces a relatively uniform layer that can be controlled to be < 100 um. Alternately, electrical contacts can be made ahead of time and then the whole sample can be immersed in silicone or another elastomer.

2.3.6 Electrical contacts

A major hurdle in any sensor with a silicone substrate is actually attaching external power/sense electrodes to the sensor since soldering is out of the question. A common method is to make conductive silicone by mixing in a percolating volume fraction of either carbon black, silver nanoparticles, or carbon nanotubes (as described earlier) to produce a percolating network that can be used like a conductive glue. While this can work, it can be difficult to get a sufficiently conductive glue. To simplify things, we opted for a clamping approach where all of our electrical contacts were made by building small plastic clamps fixed by screws that held wires (copper sheeting) in close contact with exposed regions of nanotubes after encapsulation as shown in Figure 7. We recommend this approach for situations where the sensor geometry permits it. In other cases, conductive glue may be more effective.

Figure 7: Device mounted and fully wired
A device has been fully mounted using two custom-made acrylic clamps. Each clamp respectively presses a copper electrode sheet against the appropriate nanotube surface to make a tight connection with low contact resistance. The whole assembly has been mounted on a syringe pump for cyclic mechanical testing.

2.4   Case Study: Poisson capacitor for highly elastic strain sensing

Using the simplest of the techniques described above, we will now walk through how to build a robust strain sensor capable of supporting strains of at least 100% over

thousands of cycles with minimal hysteresis. The basic design is presented in Figure 6 and discussed in the following section [38].
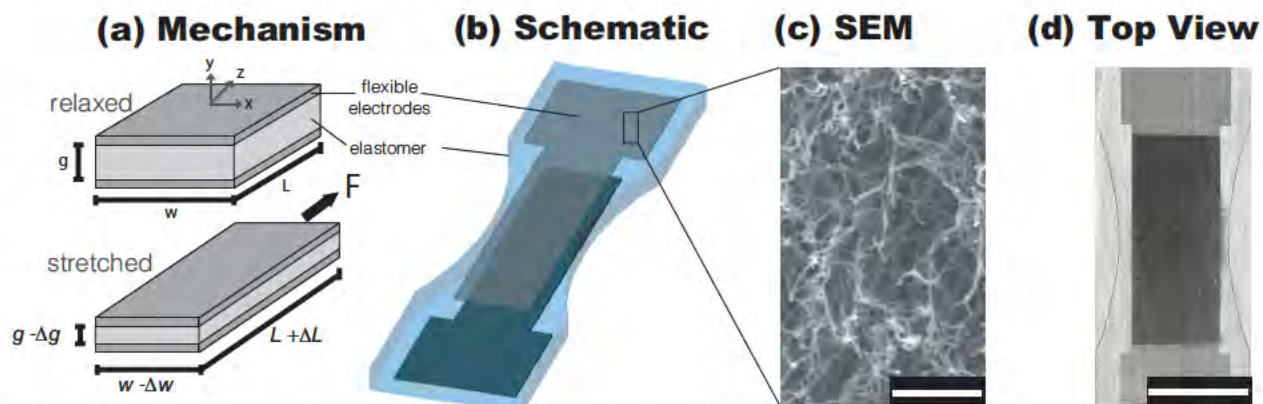
Figure 8: Mechanism, design, and fabrication of a Poisson Capacitor.
(a) Poisson contraction converts planar strain to a decrease in the gap distance between the percolating electrodes and an increase in capacitance. (b) Schematic of our device geometry; all sensing is carried out in the middle region of the sensor. (c) SEM data demonstrating percolation of the nanotubes within the electrode; scale bar is 500 nm. (d) Close-up image of the sensing region of the device. Darker region is due to overlap of electrodes, and striations are due to texture of the background; scale bar is 0.75 cm. *Adapted with permission from Cohen et al., Nano Letters (2012) American Chemical Society* [38].

2.4.1 Piezoresistance vs. Piezocapacitance

While piezoresistance-based nanotube sensors are certainly effective, they have a number of limitations that make them less attractive from a practical perspective. The primary drawback to a piezoresistive design is that the stability of the performance (the lack of hysteresis or drift) depends entirely on the stability of the percolation network. Should the statistical average of connection routes and contact resistances throughout the network shift from cycle to cycle, then the measured strain will also drift. This problem can partially be addressed by how the nanotubes are adhered to the silicone substrate. However, these methods require more complicated and expensive processing of the nanotubes. Moreover, even the best piezoresistive sensors for high strain sensing have exhibited non-linear performance and gauge factors [1]. While still quite usable, this does complicate the calibration process as well as reducing the device sensitivity and effective range. For these reasons, and because we sought to simplify the fabrication process, we opted for an entirely different mode of strain transduction based on capacitance.

Piezocapacitance occurs when a shift in the capacitance of a system is accompanied by a corresponding shift in strain in the system. To implement this using our platform, we needed to create two percolation electrodes sandwiching a dielectric (silicone) in order to produce a parallel plate capacitor. This sandwich design has traditionally been used to transduce strains normal to the surface (compression), but it has a mode of action that also allows it to transduce planar strains [8]. The general mode of action is presented in Figs. 8a/b, with an image of a completed device presented in Figs. 8c/d. The mechanism behind this kind of sensor relies expressly on Poisson contraction, whereby all elastic materials, when strained uniaxially, will experience strain of the

opposite sign in the normal axes—if you pull on something it becomes thinner. In our device, this thinning process brings the nanotube electrodes closer together, resulting in an increase in capacitance. A simple model of the mechanics is described by equations 3-6, while eqn. 7 provides a simplified model of how parallel plate capacitance can be coupled to Poisson contraction in this kind of sensor.

$$\frac{\Delta L}{L} = \varepsilon_z = \frac{\sigma_z}{E} \qquad (3) \qquad\qquad L_{stretch} = L + \Delta L = L + \varepsilon_z L \qquad (5)$$

$$\varepsilon_x = \varepsilon_y = \nu\varepsilon_z \qquad (4) \qquad\qquad w_{stretch} = w - \Delta w = w - \nu\varepsilon_z w \qquad (6)$$

Here, ν is Poisson's ratio (~0.5 for most silicone elastomers); σ is stress; ε is strain; E is the elastic modulus of silicones; and L, w, and g are the initial dimensions of the capacitor. Eqn. 3 is Hooke's law linking modulus to stress and strain. Despite the large target strains (100%), which normally require nonlinear elasticity models, an empirical fit from mechanical testing data (R^2 = 0.997) indicated that this standard linear model is sufficient to predict how the device would function. Accepting linear elasticity, we can then move to Eqns. 5 and 6 where we see how Poisson's ratio serves as the coupling parameter for strains in orthogonal axes. From these, we can then substitute these relations into the simple model of a parallel plate capacitor in Eqn 7, to arrive at an analytical expression of how capacitance should vary as a function of planar strain in the sensor.

$$\Delta C_{simple} = e_o e_{silicone} \left(\frac{w_{stretch} L_{stretch}}{g_{stretch}} \right) = e_o e_{silicone} \left(\frac{w(1 - \nu\varepsilon_z)L(1 + \varepsilon_z)}{g_{stretch}(1 - \nu\varepsilon_z)} \right) = e_o e_{silicone} (1 + \varepsilon_z) \frac{wL}{g} \quad (7)$$

Here, e_0 is the permittivity of free space, and $e_{silicone}$ is the relative permittivity of silicone. It is perhaps unintuitive to note that the final equation, despite resulting from Poisson contraction, does not depend on the value of Poisson's ratio as long as the material is assumed to be isotropic (a fair assumption for many silicones). Moreover, this equation also predicts that the capacitance will change linearly with strain so long as the electrode geometry scales elastically. What is particularly important about this point is that it means the performance of the device is now entirely independent of resistive properties of the electrodes so long as they maintain conductivity across the surface. In other words, even if there is resistive hysteresis and shifting in the structure of the percolation networks, so long as the networks can still conduct electricity and occupy roughly the same footprint and relative overlap across the sandwich, the sensor performance will depend only on Poisson contraction. It is this feature that enables such a simple fabrication method to produce a reliable sensor, so long as capacitance can be monitored accurately. That said, there is one final modification to the model that should be made, which is to take into account fringing fields. Eqn. 7, while simple, ultimately assumes an infinite parallel plate capacitor. Real capacitors will always experience electric fields at the borders that diverge from the simple model. However, these can be accounted for using the Palmer model, which acts as a scaling factor on all terms of the simple model and goes according to Eqn. 8 [43]. It was this model that was ultimately used for the simulation curves presented below (variables are consistent with those in Eqn. 7)

$$\Delta C_{Palmer} = e_0 e_{PDMS}(1+\varepsilon_z)\frac{wL}{g}\left(1+\frac{g}{\pi w}\left(1+\log\frac{2\pi w}{g}\right)\right)\left(1+\frac{g}{\pi L}\left(1+\log\frac{2\pi w}{L}\right)\right)$$

(8)

2.4.2 Testing apparatus and material characterization

The sensor depicted in Fig. 6d was affixed between two custom made clamps that held copper sheets tightly against the unexposed patches of nanotubes on the top and bottom of the capacitive sandwich, respectively. These clamps were then attached to a syringe pump (Harvard Apparatus) which was programmed to cycle continuously between a state of no tensile strain and 100% tensile strain (see Fig. 7). While slow (2 mm/s), syringe pumps make quite precise, inexpensive mechanical cycling machines. Implicit in our design is the assumption that our silicone behaves in a linear elastic manner up to 100% strain. To verify this, we mounted samples in a formal mechanical analyzer (Instron) and collected stress-strain curve data up to 100% strain at 2 mm/sec. Elasticity model assessments are typically characterized with respect to the *stretch parameter* (stretch = 1 + strain), and the linear elastic model is often contrasted with the Mooney-Rivlin non-linear elasticity model. After converting our stress-strain data to stress-stretch curves, we performed curve fitting using an optimization routine within Matlab (*fmincon*) with manual calculation of the residuals and the associated goodness-of-fit. From the data in Fig. 9 (left), there is little statistical difference between the two models. Mooney-Rivlin underestimates strains below ~30%, while linear elasticity overestimates strains below ~15%. However, on the higher end Mooney-Rivlin diverges much more than does the linear model. Given this, we opted to continue to use assumptions of linear-elasticity.

Having characterized the mechanical properties of the sensor, we needed to design a capacitance monitoring system and characterize the capacitive performance of the device. The most accurate approach for this is to use electrical impedance spectroscopy system ('EIS', Nova Systems). EIS relies on complex impedance, which requires an AC stimulation signal. In order to determine a fair sampling frequency, we measured capacitance as a function of stimulation frequency. The data is presented in Fig. 9 (right), and we used this to justify a stimulation signal at 10 kHz and a sampling frequency of 3 Hz. While a benchtop EIS system was used for characterization and parameter sweeps, the same measurements can be obtained using a capacitive Wheatstone bridge (analogous to the resistive bridge used for piezoresistors) or an off-the-shelf integrated circuit that performs EIS. Both approaches are relatively inexpensive and simple to build, and can also be scaled down in size to suit robotics and medical applications where a full EIS system is impractical and unnecessary.
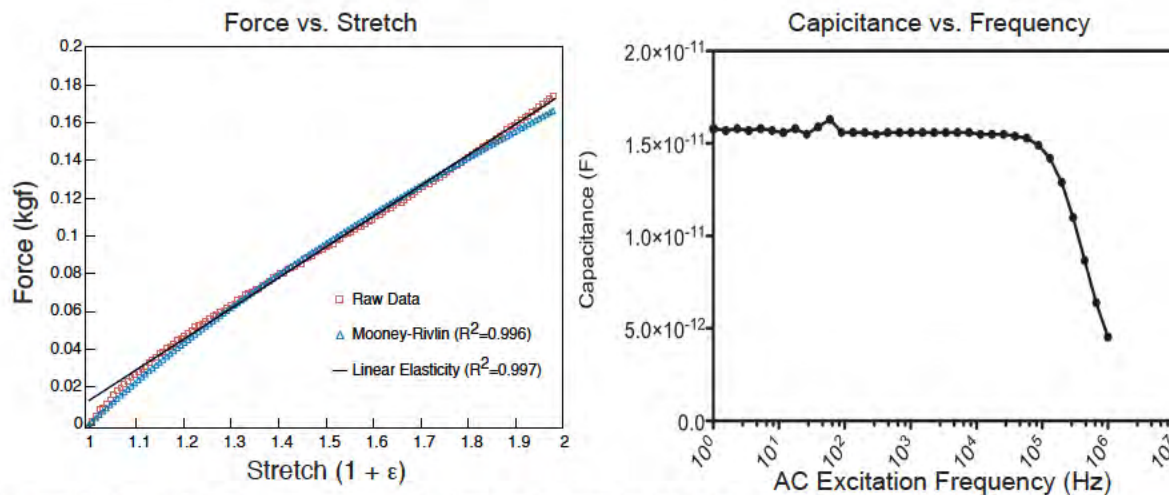
Figure 9: Mechanical properties and frequency response data
(left) Force vs. stretch curve for silicone devices. Red squares depict the raw data collected with an Instron at 2 mm/sec to 100% strain. Blue triangles represent the expected values if the material were a Mooney-Rivlin, non-linear elastic material. The black line represents the linear elasticity expected behavior. Goodness-of-fit metrics imply the two models are quite similar, although the linear model qualitatively fits the data better, especially at high strain.

2.4.3 Performance Metrics

As a general baseline, the first parameter we tested was the piezoresistive performance of one of the electrodes. To do so, we built another sensor consisting of an electrode strip that went entirely across the sensor, along with clamps that attached to either side of the same electrode to produce a resistor. Using the cycling parameters described above (100% strain, 2 mm/s), we confirmed the presence of hysteresis and nonlinearity. As show in Figure 10a, hysteresis resulted in a permanent increase in the baseline resistance of the system (measured by 2-point sensing). Further, the inset shows the presence of stress relaxation in the nanotube percolation network when the sensor was strained to 100% and held for 10 s while monitoring the impedance. The result of these phenomena was that the gauge factor itself also shifted from 0.5 to 0.25 after very few cycles.

However, when two of these electrodes were combined to make the capacitive sandwich described earlier, the performance and stability markedly improved. All devices tested (n=6) averaged a baseline capacitance of 16 pF, which implies that the fabrication method is reliable, even with variability in the percolation performance. To characterize the fundamental performance, model accuracy, and gauge factor, we looked at the dynamics of a representative stretching event to 100% strain and back at a constant strain rate, as shown in Fig. 10b. Here, the empirical data from the sensor (blue circles) is represented as the relative change in capacitance to the baseline and cleanly and linearly capture the strain dynamics of the system. Further, the ascending and descending curves ought to be symmetric given the constant strains and rates, and indeed they differ by < 2%. Given this, the gauge factor (the relative change in capacitance divided by applied strain) is linear and averages out to 0.99 over the entirety of the 100% strain range. As the theoretical optimum for a Poisson capacitor is

1, the device is performing well. The simulation curve generated by Eqn 8 is overlaid (red) on the data, and exhibits an R^2 of 0.998 relative to the measured data.
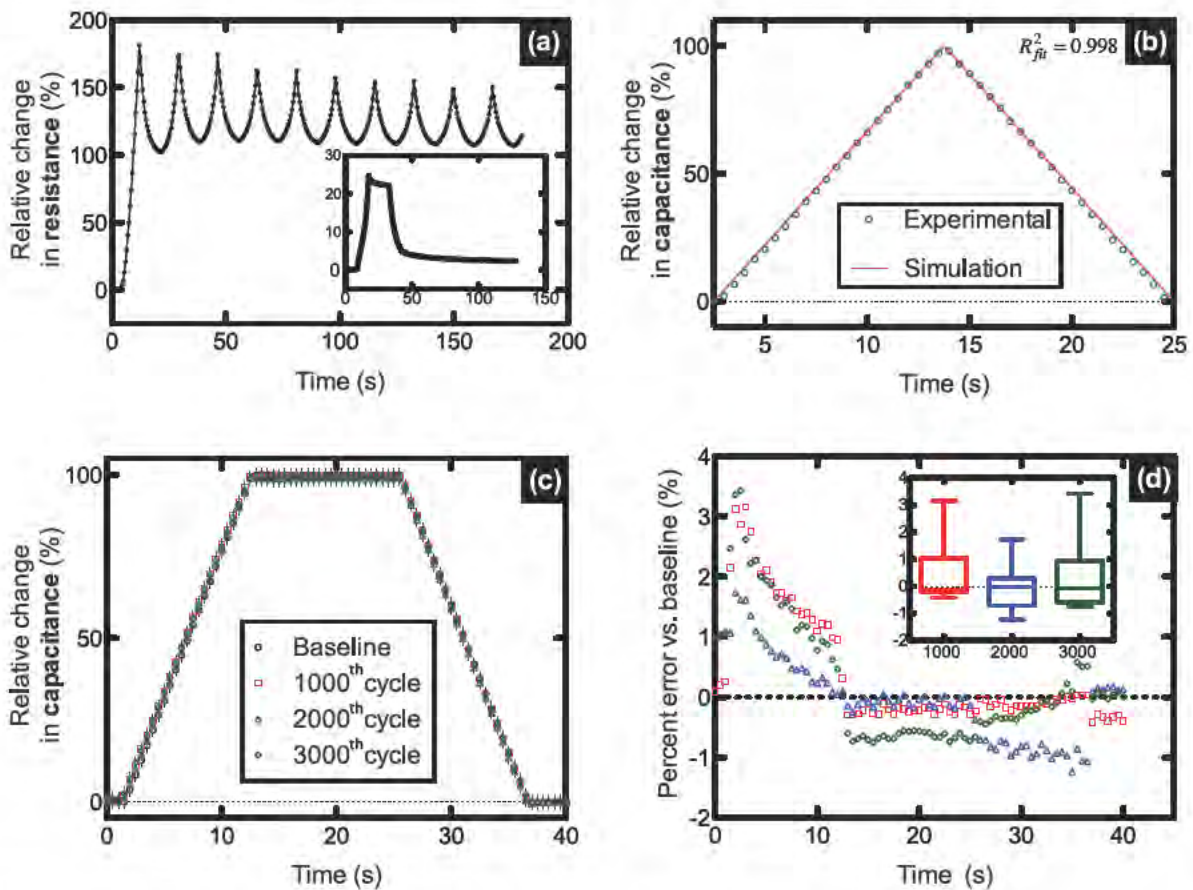
Figure 10: Performance characterization of Poisson capacitor strain gauge. (a) Resistive performance of a single percolation electrode when undergoing 100% cyclic strain. Main plot indicates significant hysteresis, while inset shows both relaxation during a 100% step strain and subsequent hysteresis during recovery. (b) Single, 100% strain cycle of the capacitive sensor (blue) overlaid (red) by the fit from parallel plate model with Palmer correction (red). (c) Demonstration of repeatability over 3000 cycles of 100% strain. After every 1000 cycles, the sample was subjected to a 100% step strain before being relaxed back to basal strain. (d) Stability plot showing how much sensor performance deviated from baseline performance over 3000 cycles. Legend is the same as for (c). *Adapted with permission from Cohen et al., Nano Letters (2012) American Chemical Society* [38]

If we compare Figs. 10a/b, we see that the prediction of the model that capacitance should be independent of hysteretic damage to the electrodes bears out. Despite the extreme fluctuations in electrode resistance, the capacitance data is quite steady. However, to properly test device stability we need to look at cyclic strain data, as is shown in Fig. 10c. Cyclic testing was conducted using the same speed as previously used, but with a 'step-and-hold' profile where the sensor was strained to 100% strain and held for 12.5 seconds before ramping down the strain. This type of profile tests both strain cycling and stress relaxation effects, and it was repeated for 3000 cycles. Fig. 10c depicts the baseline profile and then a representative profile from each batch of 1000 cycles throughout the trial. Taking these data, we can then calculate the deviation from

the baseline over 3000 cycles. This type of analysis is suited for identifying if there is any form of monotonic drift that would indicate underlying hysteresis. The resulting data, shown in Fig. 10d, indicate that, while there was up to 3% deviation from the baseline, it is not a monotonic error with respect to cycle count, and therefore it is likely due to random error rather than a systematic hysteresis. Moreover, if we normalize the error with respect to the data from the 1000th cycle rather than the first cycle, the error drops to ~1.5 % (not shown), and this in turn indicates that there is likely some slight settling in the geometry of the electrodes that occurs over the first 1000 cycles.

2.3.5   Application to bio-inspired robotics

As a demonstration of an alternative to traditional rigid transducers and encoders for robotics, we built a proof-of-concept for robotics applications where size, weight and power strongly constrain design options. Two such examples where these constraints are crucial are the MEDIC and DASH (platforms of centimeter-scale walking and running robots). Here, the exoskeleton of the robot consists entirely of origami-style composite laminates that have been cut and folded to produce from four to six 'legs' in the form of four-bar linkages. This process results in a strong and light robot (DASH is only 16 g), but also places a premium on sensing and actuation components. At present, the legs are controlled via open-loop, contractile shape memory alloy actuators and passive return springs. Using a Poisson capacitor instead of a return spring would additionally allow feedback control, in turn allowing much more consistent locomotion and more complex behaviors.

Using the same smart composite manufacturing process as used with MEDIC and DASH, we built a scaled up version off a leg linkage, and attached the Poisson capacitor in the place of the return spring. Fig. 11 presents stills of this motion sequence above a plot mapping 'limb angle' to relative change in capacitance. To do this, the system was cycled through 80% strain of the sensor (limited by the geometry of the linkage), during which time the 4-bar linkage rotates the 'limb' through a wide arc while the sensor stretches. In essence, this allows us to transduce changes in joint angles without relying on an angle encoder or any other traditional, rigid sensing component such as an linear variable differential transformer. While a simple demonstration, this type of sensing can clearly be scaled to a variety of different joints and linkages in a diverse array of robotics platforms.

2.5   Concluding Remarks

The most unexpected result from these data is the quality of the sensor performance and patterning resolution relative to the production cost, time, and ease. In terms of the raw materials consumed for a single sensor, the cost is < \$0.50/sensor. The assembly time for a single sensor from vacuum filtration to final encapsulation is ~ 30 minutes, and this can be parallelized. It is a clean demonstration of the utility of a simple principle of collective engineering (percolation), and the approach can be generalized to a variety of different applications beyond strain sensing. Ultimately, we hope that the frugality, generality, and simplicity of the approach will overcome the traditional barrier to entry of nanoscience and encourage researchers to explore incorporating carbon nanotubes into their sensors, robots and assays.
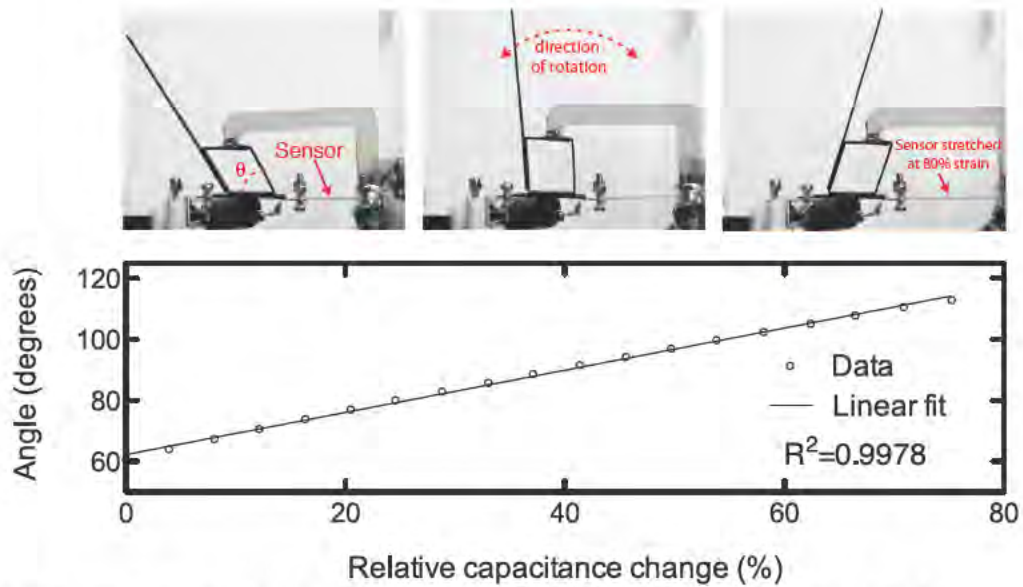
Figure 11: Demonstration of sensor as angle transducer for four-bar linkage. The image sequence is a time-lapse of the motion of a four-bar linkage 'limb'. The sensor, attached to the base of the linkage, stretches in proportion to the amount by which the limb rotates. The plot shows the mapping between sensor output and angle of the limb. The 'L' shaped structure physically pulls on the mobile part of the four-bar linkage.

Chapter 3
Spatiotemporally regulating gene activity in 2D bacterial colonies

"It must be admitted that the biological examples which it has been possible to give in the present paper are very limited. This can be ascribed quite simply to the fact that biological phenomena are usually very complicated."
-A. M. Turing,
"On the chemical basis of morphogenesis" (1952)

(Perhaps one of the greatest understatements in Science)

3.1 Chapter Overview

Nanotube percolation represents a collective behavior in an inanimate system that arises due to shape interactions amongst agents. By contrast, in this chapter we will consider an animate system consisting of living (and dying) agents. From a collective perspective, the theme here becomes one of building a tool to allow for exogenous control over a phenomenon that is normally self-regulating. While a hallmark of collective behaviors is that the emergence of order does not require any master controller, the idea we will begin to explore here examines what happens if we take a collective system and bias it with exogenous commands. This is a key idea in collective engineering where the goal is understanding how to blend top-down control with the bottom-up behaviors that typify collective behaviors. In the work discussed in this chapter, we have simplified the problem as much as possible by using a system with minimal biological complexity in order to focus on the development of a new kind of tool. As such, the work here hopefully presages things to come as our biological abilities improve and we can begin to apply this to more complex cellular systems.

More specifically, we will discuss a low-cost inkjet dosing system capable of continuous, two-dimensional spatiotemporal regulation of gene expression via delivery of diffusible regulators to a custom-mounted gel culture of *E. coli*. A consumer-grade, inkjet printer was adapted for chemical printing; *E. coli* cultures were grown on 750 μm thick agar embedded into micro-wells machined into commercial compact discs. Spatio-temporal regulation of the *lac* operon was demonstrated via the printing of patterns of lactose and glucose directly into the cultures; X-Gal blue patterns were used for visual feedback. We demonstrate how the bistable nature of the *lac* operon's feedback, when perturbed with patterns of lactose (inducer) and glucose (inhibitor), can lead to coordination of cell expression patterns across a field in ways that mimic motifs seen in developmental biology. Examples of this include sharp-boundaries and the generation of traveling waves of mRNA expression. To our knowledge, this is the first demonstration of reaction-diffusion effects in the well-studied *lac* operon. A finite element reaction-diffusion model of the *lac* operon is also presented which predicts pattern formation with good fidelity.

3.2 Overview to spatiotemporal genetics and morphogenesis

The origin of multicellularity, while shrouded in mystery, obviously involved a point where single-celled organisms became multicellular organisms. John T. Bonner, in his seminal work on the origins of multicellurity describes this transition as heralding a shift from outright competition to a sort of guarded collaboration. The argument goes that only through collaboration can multicellular structures emerge. Once these become part of the evolutionary landscape, they in turn begin to compete with other multicellular structures. While they are inherently still in competition in some sense internally, internal competition is now constrained by the same rules and selection pressures that brought the cells together in the first place so as to promote collaboration overall. In general such competition and collaboration extend both up and down from here. Organelles and genes compete and collaborate, as do the organisms themselves. These behaviors extend even up to the super-level of the colony, as is seen in social

insects where the colony itself becomes, as Bonner describes it, "a higher unit of selection".

For our purposes, the key point to consider here is that multicellularity inherently requires some sort of communication across the agents that make up the collective, or organism. The evolution of this communication is a topic for a great many other dissertations (as is a discussion of how it works), but the fact is that it arose throughout the course of evolution and has proven to be surprisingly potent. Such communication ultimately explains everything from why tigers have stripes (and why spotted cats have striped tails), to the regeneration of salamander limbs, to our own peculiar shape with its gangly limbs, and 10 well-proportioned fingers and toes. Ultimately, all form and function in multicellular organisms is a testament to agent-agent communication. Morphogenesis, first coined and quantified by Alan Turing, is the term normally applied to describing how a single cell can become many, and how the many can come to look like a platypus, porcupine, or panda. What Turing postulated (correctly in many cases) is that many of the patterns we see in organisms (stripes, proportions, symmetry, etc.) can be explained by relatively simple communication based on chemical diffusion gradients, activator-inhibitor combinations, and so forth. As a simple example, the combination of two such **morphogens** (bicoid and nanos) diffusing anti-parallel from opposite sides of a drosophila (fruit fly) embryo are sufficient to specify the anterior/posterior division plane in the embryo. This specification works because every cell (or proto-cell) in the embryo is running nearly identical genetic code and essentially sampling its immediate environment. The anti-parallel diffusion of bicoid and nanos produces two contrary concentration gradients that, when sampled as a ratio by cells, define a proportion specifying the anterior-posterior divide. This is an extraordinarily oversimplified view of the process, but the point is that we see how profound information can be extracted from relatively simple morphogenetic cues. This kind of self-organizing works in that every agent is 'running' identical code but acting upon local variations in the environment.

This, in turn, is where we introduce collective engineering again. In this simplified framework, we have a population of agents all behaving similarly and high susceptible for local environmental cues. Therefore, if we could exogenously manipulate those cues, we could, to some extent, predictably engineer the resulting behavior of the cellular collective. The beauty of this kind of engineering approach is that it allows the cells to handle all the downstream work of transducing the input signal into complex cellular behaviors. In this way, relatively simple engineering inputs can exert complex control over the behavior of the biological system. In practice, such morphogens can be anything from chemical signals to mechanical forces to thermal fluctuations to electric fields (as seen in Chapter 4). Given this, we designed a tool intended specifically delivering patterns of chemical morphogens to large bacterial colonies.

The development of methods that introduce spatiotemporal perturbations into developing, multi-cellular systems via soluble molecules has a long history [1-4] and a rich, recent body of literature. Specifically, advances in microfluidics [5-10] and biochemistry [11-14] are beginning to open the door to direct modulation of developmental pattern formation at the spatial and temporal scale of the cell's control circuitry. Such devices can provide spatially rich, real-time input-output (I/O) signals to bias developing cells into specific phenotypes. In the context of synthetic biology,

such interfaces would add a degree of control over the pattern formation dynamics in multi-cellular structures that are expressing genetic circuits intended to coordinate activity through soluble molecules [15]. Initial efforts in building synthetic multicellular constructs have already begun [15,16], and as these mature, a robust chemical interface will be invaluable in addressing and biasing the development of patterns. In the context of control theory, such devices would allow an exploration of equilibria, stability criteria, and the non-linear dynamics of regulatory circuits. In the context of regenerative medicine and tissue engineering, these devices could potentially provide active, spatiotemporal control of morphogenesis [8,17,18].

While it is clear that these applications call for systems capable of high-resolution dosing of multiple chemicals onto ensembles of cells, it is less clear how best to achieve this in a way that is low-cost, versatile, and open-source. Although a number of microfluidics-based attempts have been published [5,9,19,20], all have limitations in resolution, complexity of fabrication, or ease of use. As an alternative to microfluidics, we considered inkjet technology. To date, inkjets have been incorporated into a variety of biological techniques including: direct cell printing for patterning [21,22] and tissue engineering [23-27], assorted cell factor printing to regulate cell positioning and behavior [27-30] and DNA micro-array fabrication [31]. This list demonstrates the versatility of the platform. There are even commercialized research grade inkjet systems available (such as the Fujifilm Dimatix system), although these systems tend to be orders of magnitude more expensive than consumer grade systems. Regardless of the system, it is clear that inkjets are quite versatile, although they have yet to be used for active regulation of cellular behavior.

This chapter presents the adaptation of a commercial, low-cost, piezoelectric inkjet printer and commercial compact discs (CD's) for use as a chemical interface system designed to actively regulate cellular development (Figure 1). The printer is capable of addressing up to six different soluble chemicals, and subsequently delivering precise doses of these chemicals to cell cultures at 226 dots/mm. The platform can be integrated with inline microscopy to acquire data at specific time points post-dosing. Additionally, no custom software is required for our approach, making the whole system simple and user-friendly. While the CD platform is compatible with the rich toolset of polymer microfluidics [32,33] and could be adapted into a more sophisticated device in future work, its use here was solely as a convenient, readily modifiable substrate that was compatible with the printer. In this study we used the inkjet to control the spatiotemporal reaction-diffusion dynamics of gene expression in the *lac* regulatory system by printing specific patterns of lactose and glucose onto a field of *E. coli*.

The choice of *lac* was deliberate, in that it is commonly used in synthetic biology and has a number of interesting control features, including well-characterized feedback and multiple stable states [34-36]. We were surprised by the observation that the bistable nature of the *lac* operon's feedback system, when perturbed with patterns of lactose (inducer) and glucose (inhibitor), can lead to coordination of cell expression patterns across a field in ways that mimic motifs seen in developmental biology. This is especially interesting given that, while subsets of chemical feedback systems such as *lac* include Turing systems and other stable patterning systems, *lac* itself is merely a chemical system with positive and negative feedback [37]. Examples of this behavior include sharp gene expression boundaries and the generation of traveling waves of

mRNA expression from single 'trigger' patterns. In this context, lactose and glucose are analogous to morphogens in a developing system, with the *lac* operon acting as a general template for exploring how spatially-graded perturbations generate rich behavior in bistable circuits.
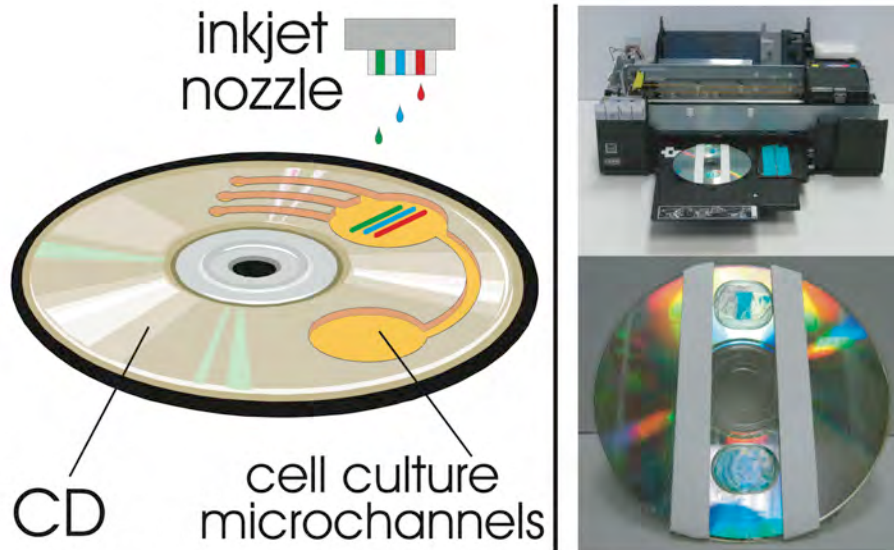
Figure 1: Overview of the printing system.
(left) the dosing method is based on the delivery of multiple chemical compounds from piezoelectric printer heads onto specially prepared compact disk (CD) templates modified so as to support thin layers of microbial agar cultures, (upper-right) the printer used was the Epson R280, here shown being loaded with a modified CD, (lower-right) close-up of a modified CD with stand-offs for the print rollers and two LB/X-Gal agar cultures of *E. coli* dosed with lactose patterns (which induce the characteristic X-Gal blue color, see text).

3.3   Theory and Model

The *lac* operon is one of the best-studied regulatory pathways in microbes [34-36,38]. In *E. coli*, kinetic data for the entire *lac* operon is available and robust models have been developed [34,35]. Moreover, the dynamics of the system are well understood, and are known to exhibit multiple stable points [34-36]. In the canonical *lac* system (Figure 2), extra-cellular lactose is taken up by lactose permease, where it is converted to allolactose by β-galactosidase. Allolactose upregulates the production of both β-galactosidase and lactose permease by inhibiting the repressor of the *lac* promoter. This lactose-based, positive feedback loop has been shown to be bistable [34]; below a certain lactose threshold, little lactose is converted, while above this threshold the system jumps to a much higher consumption rate. Glucose acts to inhibit the conversion of lactose by lowering the transcription rate of the *lac* operon via cAMP and the catabolite repressor protein (CRP). This acts as negative feedback for the conversion of lactose. The table in Fig. 2 is essentially the truth table for the operon, summarizing how it responds to various environmental combinations of lactose and glucose. This indicates how the operon can be controlled via selective dosing of lactose or glucose. Both lactose and glucose are soluble in the extra-cellular space. We chose to model (Figure 2) the *lac* system as a set of coupled differential equations, following models developed by [34,35]

(Figures S1 and S2, and Tables 1 and 2 in the Supporting Documentation). The well-known X-Gal assay [39] introduces the soluble X-Gal compound, which is cleaved by β-galactosidase into 5-bromo-4-chloro-3-hydroxyindole, in turn oxidizing to 5,5'-dibromo-4,4'-dichloro-indigo, finally resulting in an insoluble blue product. This allows for β-galactosidase activity to be assayed.
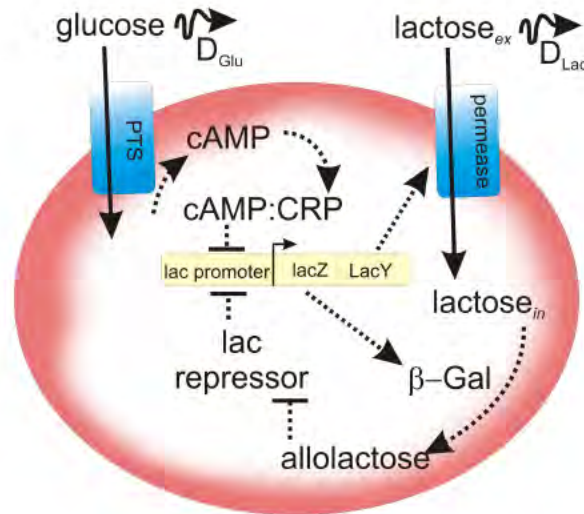
Lactose	Glucose	Operon State
No	No	OFF
No	Yes	OFF
Yes	Yes	**Very** low ON
Yes	No	**Full** ON

Figure 2: Graphical representation of the *lac* operon and operon logic table
This depicts the model used with the simulation. Glucose is the preferred fuel, with lactose being a secondary choice. The table summarizes the logic operations of the operon. See *Appendix A* for modeling and simulation details.

3.4   Experimental Methods

All experiments involved a series of four steps, detailed below. First, bacteria were cultured in advance of an inkjet print run. Once at the proper optical density (OD_{600}), they were spread over an agar substrate containing X-Gal and incubated until printing time. During the incubation period, the printer was sterilized and loaded with lactose and glucose. At the appropriate time, the bacteria were removed from the incubator, loaded onto the substrate CD, printed upon, and placed back in the incubator. Additional information is provided in the *Appendix A*.

3.4.1 Cell Culture
E. coli strain MG1655Z1 was used in this study [40]; the strain contained a low-copy number plasmid (pNS2-σVL) with three reporters, one which is GFP driven by the *lac* promoter. The initial culture, suspended in LB Agar (Sigma LB at 20 g/L, and Sigma Bacteriological Agar at 14 g/L), was prepared for freezing with the addition of 50% glycerol. Colony plates were created by taking a sterile loop and transferring a sample

from the freezer stock to 5mL of LB Broth (Sigma, 20 g/L) containing *Kanamycin* (50 μg/mL). This culture was incubated at 37 °C for 12 hours and then spread, via sterile probe, onto the surface of an LB Agar plate containing *Kanamycin* (50 μg/mL). The colony plate was incubated at 37 °C for a further 12 hours, before being transferred to a refrigerator maintained at 4 °C.

3.4.2 Print medium preparation
LB Agar was poured to a depth of 750 microns in Petri dishes and chilled overnight at 4 °C. Prior to plating the cells, the plates were removed from the refrigerator, and 200 μL of X-Gal solution (Sigma, 20mg/ml in DMSO) was bead-spread onto the surface of each plate. Ten minutes were allowed for the X-Gal to penetrate the agar, and for the DMSO to evaporate. Finally, 150 μL of an overnight *E. coli* suspension (diluted to OD_{600} 0.8) was bead-spread onto the surface and allowed to sit for 10 minutes, after which the plates were wrapped with Parafilm and placed in a 37 °C incubator for 3.5 hours at which point they had just entered exponential phase [41].

3.4.3 Inkjet modification and printing
As detailed descriptions of the modifications made to the Epson R280 are included in the Supplementary Text and video files, an abbreviated summary is presented here. The necessary modifications require commonly available tools and several hours to complete, and the procedure should be adaptable to a number of different printer types.

We used an Epson R280 inkjet for a number of reasons. Epson printers use piezoelectric print heads, as opposed to thermal jet heads. While both types of print head would probably suffice for our experiments, the mechanical nature of piezoelectric heads means that they can safely print a greater array of chemicals, and they do not impose temperature fluctuations on the printed fluid. Additionally, the R280 has the ability to print on rigid substrates (compact discs), which is not a common feature. Finally, the whole system is low cost (~$100) and widely available.

There are three fundamental challenges related to manipulating a printer: loading customized inks, uniquely specifying which inks are used during a print job, and interfacing with the biological substrate. Using an Epson R280 printer, we were able to load our lactose and glucose inks by interrupting the ink-charging process and manually injecting, by syringe pump, our solutions into specific color reservoirs (300 mM lactose, 500 mM glucose). This technique requires no manipulation of the ink cartridges themselves; we inject ink downstream of the cartridge, meaning that the printer functions completely normally but prints the injected solutions rather than ink. This is simpler, less prone to damage of the printer, and does not require the use of third-party hardware. Having primed the printer, the final step was to prepare it to accept a cell-bearing substrate.

We took advantage of the R280's ability to print directly onto the surface of compact discs and milled 800-micron deep wells directly into the surface of CD's. The size, geometry, and position of these wells were selected so as not to interfere with any of the printer's mechanisms (feed rollers or carriage drive system). By using a CD template in Adobe Photoshop, it was possible to create any planar pattern, uniquely specify the inks to be used, and print directly into the wells.

3.4.4 Printing of chemicals onto cultured E. coli

We used sterile shim-stock to cut out individual pieces of cell-bearing agar and transfer them to the appropriate wells on the surface of the CD. The CD was then loaded into the printer, and the print job sent. No run lasted longer than two minutes, and at no point did the cells come into contact with any components of the printer, which had previously been sterilized with 70% ethanol. Post printing, the agar slices were transferred to hydrated Petri dishes, placed in the incubator, and observed over a period of 15 hours.

3.4.5 Microscopy and Image Analysis

Static images were taken at 15 hours post-printing, and were captured using a fluorescent backlight and an 8 mega-pixel digital camera (Canon A590). Time-lapse data was collected using an Intel QX3 microscope positioned within the incubator. All images were subsequently grey-scaled, and intensity profiles were calculated using ImageJ. The resulting intensity profiles were normalized so that higher intensity values imply a greater transmittance of light. All simulation data was obtained according to the parameter set specified in Tables 1 and 2 in *Appendix A*.

3.5 Results & Discussion

There were three key goals for this work. First, we aimed to demonstrate the feasibility of using a commercial inkjet printer as a micro-dosing chemical interface for cellular systems. Second, we wished to determine whether inclusion of diffusion terms into a partial differential equation (PDE) model of the lac operon would predict the gene expression patterns generated by the printer. Lastly, we hoped to explore the types of morphogenetic-like behaviors that could be induced solely through direct, chemical manipulation of the *lac* operon.

3.5.1 The bistability of the lac operon generates sharp gene expression boundaries

We first characterized the resolution and pattern-formation capability of the printer system. As we were printing into hydrated agar (which would allow for diffusion of any dosed molecule), we could not rely on the resolution specifications of the print head. Concentrated lactose (300 mM) was printed in parallel bars of varying widths onto samples and the resulting X-Gal pattern was recorded (Figure 3). By fitting this data (in addition to the transient data presented below) to our finite element reaction-diffusion model, the effective diffusion rates were calculated. The fact that competition between diffusion and reaction rates biases the bistable response of the *lac* operon is evident in Figure 3. Below a certain width of printed inducer, diffusion reduces the peak concentration, and the lac operon never switches to its ON state (note how the fourth bar shows a marked, non-linear decrease in induction). For 300 mM lactose and our agar formulation, features smaller than 700 μm tended not to visibly induce. Thus, by varying the diffusion constant of the medium and the concentration of dosed inducer, the exact minimum width of an induced feature can be precisely controlled. A demonstration of this involves using half-toning to produce size-graded, two-dimensional features across a field of cells (Figure 4). Here, we see blurring between closely spaced, large features, but more well defined smaller features. The implication is that, by taking the transport characteristics of a system into account, we can modulate how features interact with each other.
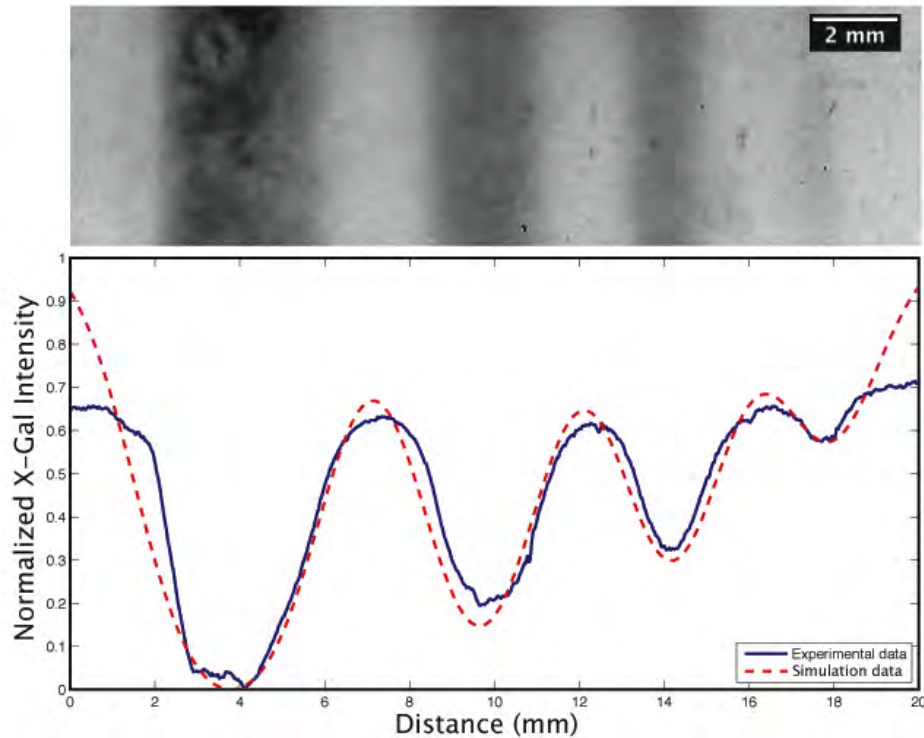
Figure 3: Resolution test varying only the width of the printed region.
Four bars of lactose were printed with the following widths (left to right): 3.5 mm, 2.0 mm, 1.5 mm, and 0.75 mm. Note the abrupt transition to a low level of induction at the 0.75 mm bar. Further note the close agreement between the empirical data and the simulation. The discrepancies at the boundaries are a result of the optical properties of the agar at the boundaries of the sample that were not taken into account in the simulation.
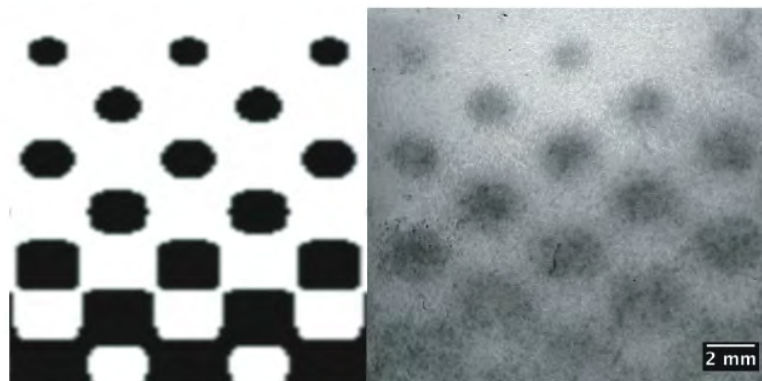
Figure 4: Half-toning demonstration of minimum feature spacing.
Half-toning was used to produce a 2-D, graded template (left) with the feature density decreasing towards the top of the pattern. As expected, large, closely situated features tended to blur (right), while distinct features emerged when the feature density decreased. This behavior can be used to modulate feature interaction as a function of geometry and the transport properties of the medium.

Bearing this in mind, Figure 5 shows a crosshatched pattern used to test the uniformity of response (and resolution) across a large field of cells. This also demonstrates how the

inkjet, in conjunction with a bistable circuit, can be readily used to produce sharp boundaries enclosing non-induced material even in the presence of an inter-diffusion zone. By taking advantage of bistability in the presence of weak gradients, we can achieve fairly sharp boundaries (see below), a motif observed in embryonic developmental programs [42]. Given a well-tuned simulation tool, it is possible to design and print almost any induction pattern within the resolution constraint given above.
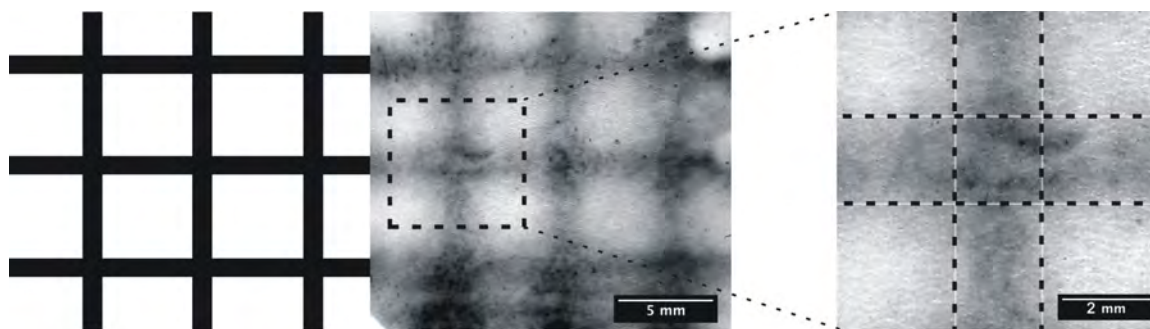
Figure 5: Crosshatched lactose resolution testing.
The printer template and corresponding induction profile are shown (left), alongside a close-up of a junction, which demonstrates the sharp drop-off in induction that occurs, despite diffusion.

3.5.2 Inline microscopy captures time-lapse pattern formation data

Figure 6 shows the development of X-Gal pattern over time subsequent to lactose induction. Time-lapse microscopy was performed within an incubator, with images being taken every 20 minutes for a period of 3 hours (see Methods). This data was used to fit the finite element model diffusion rates. Typically, induction becomes visible by eye after 45 minutes, and will then plateau at around 1.5 hours.
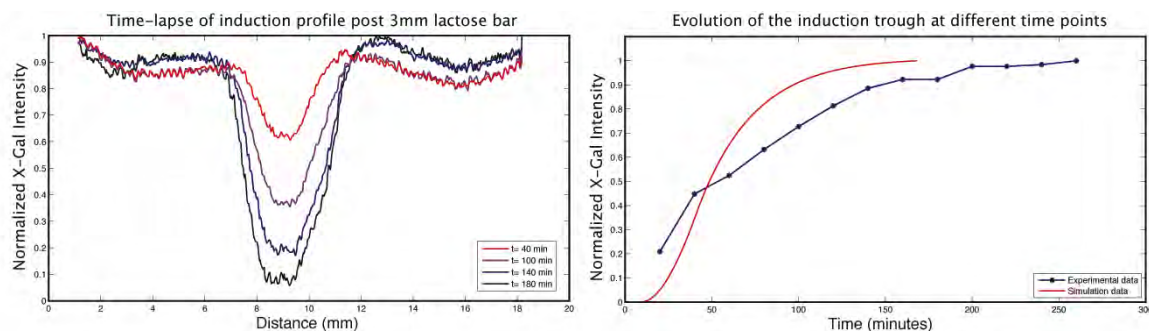
Figure 6: Transient lactose induction profiles
A single bar of lactose was printed and observed for 3 hrs. Induction profiles taken at various time points are presented (left) alongside the corresponding rate curves. Each data point in the empirical rate curve comes from averaging the intensity across the trough of the corresponding induction profile.

3.5.3 Inkjet printing allows for the printing of 2-D spatial chemical gradients

Figure 7 shows results for a piece-wise continuous lactose gradient across a field of cells. Working from a grayscale image generated on a commercial drawing program

(CorelDraw 11.0), the first bar contains 0.24 M lactose, and each subsequent bar is 20% less concentrated than the previous bar. Such a pattern is not easily attainable without a patterning device, such as the inkjet, and demonstrates the ability to produce customized, finely controlled patterns, in turn allowing fine control of cellular behavior.
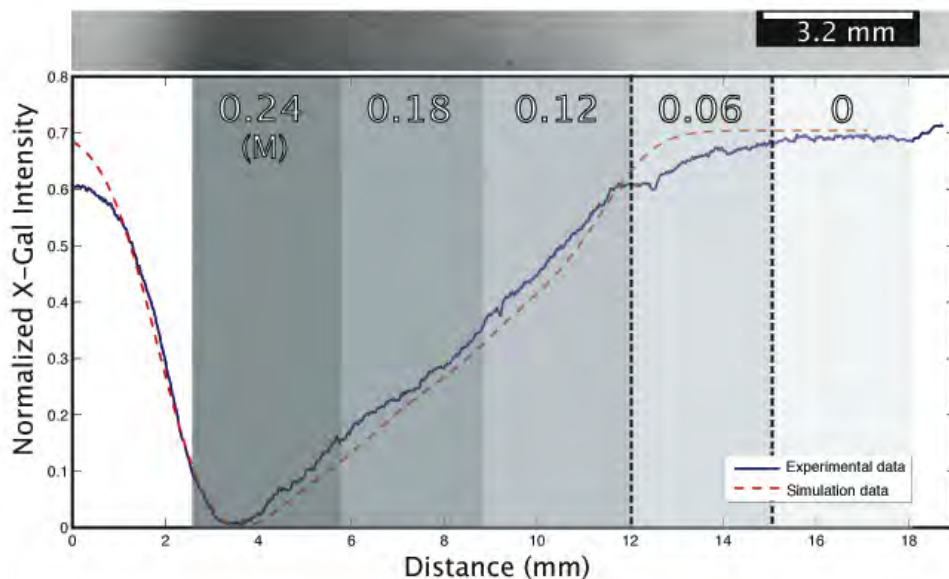
Figure 7: Piecewise continuous lactose gradient profile
Here, a 5-bar (3.2mm/bar), piecewise continuous lactose gradient was printed, where the numbers across the bars represent the concentration of lactose printed in that bar. Again, we see very close agreement between the empirical data and the simulation. Additionally, despite lactose being printed across most of the region, we detect induction only up to the 0.06 M region (between the dashed lines), which represents the theoretical bi-stable threshold concentration for the *lac* operon.

3.5.4 Patterns of multiple chemicals can be printed

We took advantage of the R280's ability to print multiple types of ink by creating patterns composed of both lactose and glucose. Specifically, we first printed a large, uniform field of lactose (300 mM) over an entire sample, immediately followed by a narrow bar of glucose (550 mM) printed on top of the lactose. Glucose is an exceptionally strong transcriptional inhibitor for the *lac* promoter, and this effect is demonstrated both by the complete lack of induction underneath the glucose bar, and the graded level of induction propagating out from that region (Figure 8).
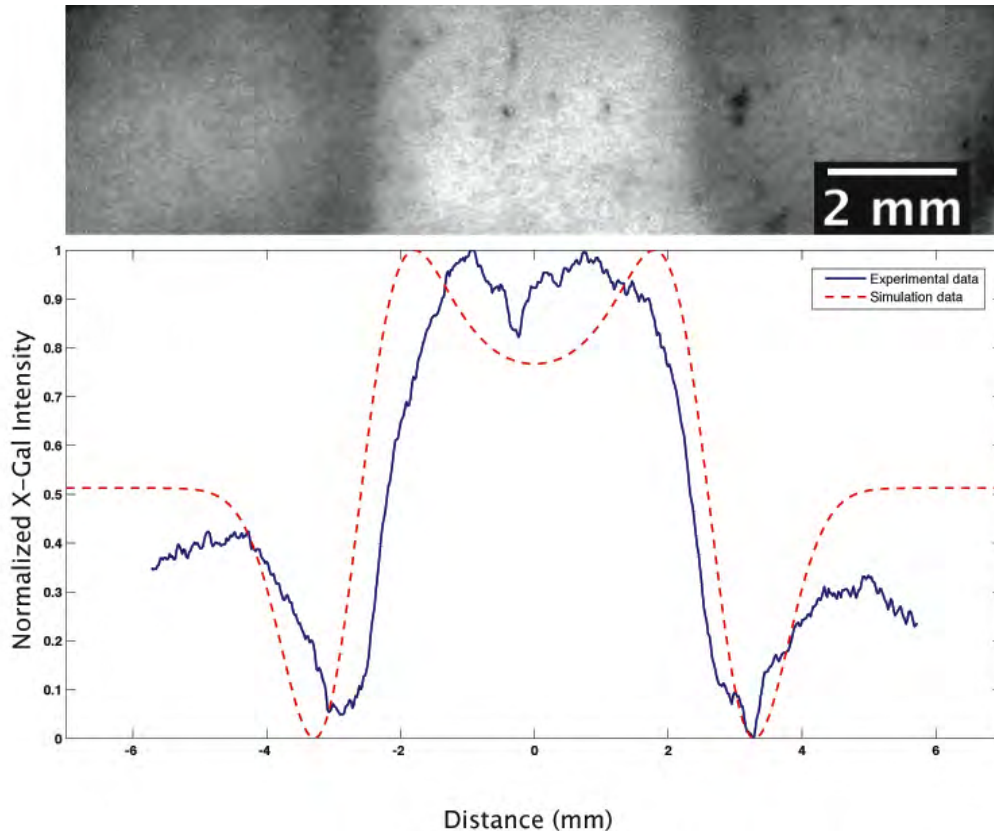
Figure 8: Activator-inhibitor printing with lactose and glucose
Lactose was first printed over an entire field of cells. Following this, a glucose bar, measuring 2.2 mm wide, was printed down the center of the field, on top of the lactose. Glucose is an inhibitor, while lactose is an activator. The result, with which the simulation agrees, is a region of repressed *lac* operon activity framed by dark boundaries. The increased induction arises because the lactose under the glucose is not consumed and therefore diffuses laterally, increasing the amount of lactose available for consumption along the boundaries.

3.5.5 Subtle reaction-diffusion dynamics arise from patterned activator-inhibitor dosing to a bistable system

In addition to predicting general features of X-Gal production patterns, our model predicts two pattern formation phenomena that arise as a result of spatial heterogeneity in the initial conditions (Figure 9).

Size invariance in a printed field (Figure 9a).
The multi-stable nature of the lac operon [34-36] allows for counter-gradients of glucose and lactose to generate an ON/OFF boundary (as in Figure 8) at the same location relative to the size of the field (Figure 9a). This is a classical motif in developmental biology known as the French Flag problem [43]; it is interesting to observe that even in a regulatory system not intended for pattern formation, such behavior arises simply as a consequence of coupling bistable gene regulation with weak (linear) gradients.

Traveling pulses of gene expression emerge from a single initial printed pattern (Figure 9b).
The coupling of the *lac* operon's reactions and the diffusion of lactose and glucose lead to interesting dynamical behavior at boundaries between glucose and lactose patterns (Figure 9b). Regions dosed with lactose above the threshold for induction will immediately begin to uptake (and metabolize lactose); conversely, areas dosed with high amounts of glucose will not uptake lactose until all of the glucose is taken up. This creates a reservoir of unused lactose in the glucose-dosed regions that begins to diffuse into the lactose-dosed regions where it is taken up. This phenomenon leads to the darker regions seen at the boundaries (and predicted by simulation) in Figure 8. More interestingly, as both reaction and diffusion of glucose near the boundary deplete glucose, inhibition for lactose uptake progressively weakens and a traveling pulse of *lac* mRNA transcription arises, originating from the lactose region and extending into the glucose-rich areas.

(a)   (b)
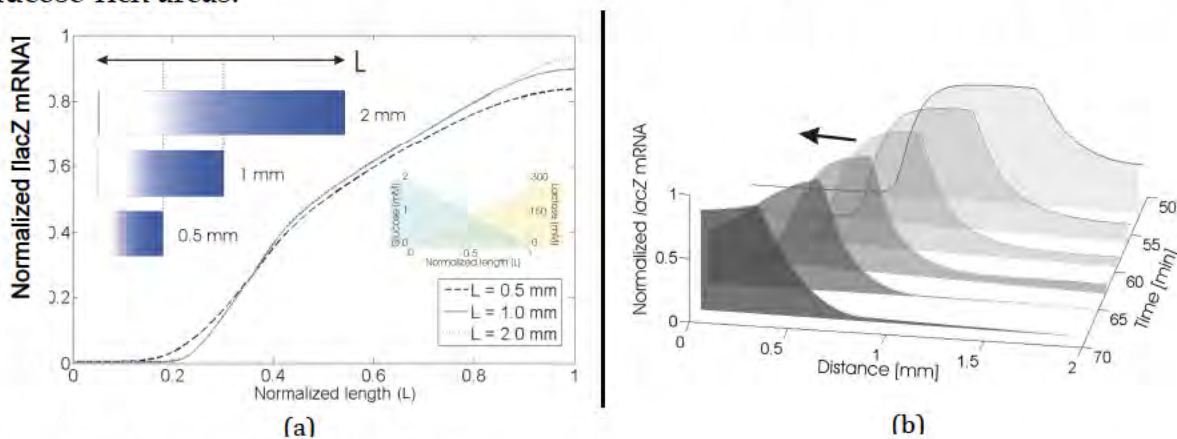
Figure 9: Reaction-Diffusion Dynamics
(a) Counter-gradients of activator (lactose) and inhibitor (glucose) result in scale invariant features that preserve proportions. This was demonstrated in simulation with three different trials where the lengths were varied. The simulated data shows the normalized lacZ mRNA concentration as a function of the distance for three different length cases, and this clearly demonstrates the phenomenon of scale invariance. (b) Plot of normalized lacZ mRNA concentration for several time steps. Here, a 2 mm long strip is simulated as having been printed with 270 mM lactose, on top of which 2 mM is printed for $x < 0.75$ mm. Initially, lacZ mRNA is heavily up-regulated in the lactose only region ($x > 0.75$ mm); as both glucose is consumed for $x < 0.75$ mm and lactose is consumed for $x > 0.75$ mm, an mRNA peak emerges which travels to the left over time (arrow indicates direction).

3.6 Conclusions

This work proposed and developed a low-cost, simple interface for regulating spatiotemporal gene expression through the use of a consumer-level inkjet printer. The system was successfully demonstrated using lactose and glucose to manipulate the *lac* operon in *E. coli*. By printing a particular chemical dosing pattern in both space and time, the printer is able to regulate the micro-chemical environments within a field of cells, therefore serving as a 'collective engineering' master controller. These data imply that, were this tool to be applied to a more sophisticated biological system (as our biotechnology improves), we would be able to spatiotemporally manipulate complex signaling pathways just as easily.

We note two fundamental biological observations from our work. First, even genetic regulatory systems not used for cell signaling (*lac*, in this case), can be adapted to mimic developmental, morphogenetic regulatory systems. As long as spatiotemporal control of chemical dosing can be achieved, many such systems might be manipulated to perform in a manner that mimics more traditional developmental pathways. Second, the ability to disturb chemical boundary conditions in space and time (especially, if used in conjunction with inline imaging) may reveal new and rich dynamics even in classical gene circuits (like the canonical *lac* operon). Moreover, apart from the ability to print simple line and dot-based patterns, the printer allows for graded dosing profiles to be created. Owing to the non-linearity of reaction-diffusion systems, there are important dynamics that likely cannot be seen without graded initial conditions. Ultimately, as the system improves, the loop can be closed with real-time monitoring of genetic activity coupled to a controller that can actively correct or redirect activity by regulating the temporal aspect of the dose profiles. This system can be informed by using computational simulations as a design tool to obtain specific patterns (in much the way that Computer Aided Design systems work). Our system and techniques are simple, rapid, and inexpensive, making it an attractive option for others interested in exploring the effects of spatiotemporal dosing.

Chapter 4
Collective engineering of cell migration via bioelectric cues

"None but those who have experienced them can conceive of the enticements of science. In other studies you go as far as others have gone before, and there is nothing more to know; but in a scientific pursuit there is a continual food for discovery and wonder."
-Victor von Frankenstein in *Frankenstein*
Mary Shelley, 1818

4.1 Chapter Overview

Thus far, we have explored collective engineering methods that emphasize steady state behaviors and systems that, at the level of interest, are non-motile. Here, we will shift the focus to **collective motion**—the collective process of myriad agents moving as a group[1]. When we think about collective behaviors and swarms, collective motion is typically what comes to mind—flocking birds, schooling fish, migrating wildebeests, etc. These are only a few of the examples we can see at the macro scale, and a plethora of collectively moving agents exists at the micro scale. For instance, were we to zoom in on the bacteria that comprise the colonies presented in Ch. 3, we would see that, as the colonies becomes confluent via bacterial division, individuals begin to abut against their neighbors. The result is that, as a function of their rod-like shapes, the bacteria begin to push on their neighbors and force local alignment patterns within the colony. However, a much more dynamic, micro-scale example is what happens when large numbers of mammalian cells migrate together. These migrations happen continuously *in vivo*, although most markedly during embryogenesis, morphogenesis, and wound healing where large numbers of cells need to arrange themselves in a coordinated fashion. Such behavior offers us a great deal of engineering potential for tissue engineering (the manipulation and growth of biological tissues for medical or engineering purposes). For example, the work in this chapter was originally inspired by the goal of improving wound healing through engineering the collective motion of cells within and near a wound in order to accelerate and improve healing.

From the perspective of collective engineering, this is the most complex of the examples presented thus far. First, we must identify a control approach to manipulate the migration of collectives of junctioned cells (adhered to their neighbors). The concept is not dissimilar from that of a sheepdog/shepherd precisely controlling the behavior of herds of sheep. In our case, finding it difficult to scale sheepdogs down to the length-scale of mammalian cells, we opted for a little known bioelectric approach whose origins date back to the 19th c. As for the analysis itself, the same quantitative analyses (imported from statistical mechanics) that describe herded sheep, flocking birds, and the like also describe migrating cells. Finally, monitoring the 'herding' process requires a read-out based on the local migration dynamics of the cellular collective. This read-out is derived from computational methods from aerospace engineering that were originally intended to assess aerodynamics. Given this mélange of concepts and methods, this chapter includes not just a description of the research, but detailed historical, scientific, and methodological asides to illuminate the full scope of the research involved.

4.2 Epithelia as migrating collectives; scope of research

Collective behaviors, which emerge at the population scale from individual interactions, permeate many systems from animals (penguins, starlings, fish, ants), to road traffic flow, to cell migration[1–12]. The breadth of this phenomenon emphasizes the ubiquity of large-scale order in the absence of a master controller. Progress in understanding these behaviors is most advanced for collective cell migration, being driven by new

technologies including monolayer stress microscopy[8,9,13], cellular Particle-Image-Velocimetry (PIV)[7,14], and biophysical statistical mechanics[7,8,15]. By probing material properties and cellular mechanisms, these technologies have identified collective cell behaviors in embryonic development and metastatic cancer[16–20]. Collective analyses extract fundamental properties of individuals from observations of the population. These approaches have demonstrated that cellular collectives are analogous to complex materials with distinct phase transitions[7,21], collective cell migration is modulated by principle stress axes and free surfaces[8,9], collective behaviors vary markedly across different cancer cell lines[18,22], and geometric boundaries affect migration dynamics[11,12]. What emerges from these studies is that tissues are an active material in which physical coupling between cells and inter/intracellular feedback loops create a collective decision network that produces emergent behaviors. **This suggests a new class of question: can we use this framework to control collective cell behavior in a predictable fashion, such as how a sheepdog guides sheep? Following this, we sought to develop analogous interactive tools to spatiotemporally direct the collective migration of epithelial cells.**

The canonical model for studying collective cell migration is a monolayer of **MDCK-II epithelial cells** in which cell-cell junctions physically link cells to each other. While the two most common perturbations - the scratch assay and the barrier assay - have been useful for characterizing fundamental cell behavior in monolayers, neither affords interactive, spatiotemporal control of cell movements. The scratch assay requires 'wounding' a monolayer and observing the 'healing' migration of cells into the 'wound' area[23]. The barrier assay involves the formation of a cell monolayer either around a removable barrier[10,12,13] or within a confining environment[11].

We demonstrate here the ability to precisely pattern cell monolayers, and then spatiotemporally manipulate cell migration behaviors without disrupting the structural integrity of the monolayer. Our approach adapts the well-established (yet often overlooked) phenomenon of *galvanotaxis* (migration of cells in a weak, DC electric field) to induce directed collective motion. Prior to this work, galvanotaxis had not been employed as a tool for controlling cells. Rather, previous work had overwhelmingly focused on the migration of single cells in unidirectional electric fields (single axis migration) with little emphasis on temporal dynamics. By contrast, our perspective specifically considered how junctioned collectives of cells would be behave **as a migratory unit** when exposed to DC fields, and how much exogenous control could be exerted over their behavior. To explore this, we identified several control and characterization goals:

1. **Characterization of the temporal response and 'bandwidth':** How quickly can cells respond to a change in the field polarity?

2. **Characterization of local spatial control:** Can a 2D electric field be superimposed on cellular collectives, and if so, how will a population respond that is receiving different (or even contradictory) migration instructions in different regions?

3. **Biological design parameters:** How important are the collective geometry and the properties of the cells at the borders?

Given these guidelines, we used shaped electric fields with precisely patterned epithelial monolayers to demonstrate an array of novel cell behaviors. Most notable were monolayer migration reversal via local 'U-turns', and multiaxial control of migration trajectories within a single monolayer. We then explored the interplay between population geometry and our ability to control cell migration. Taken together, we find that the migration patterns of cells in epithelial monolayers are highly plastic and controllable via galvanotactic cues. In addition to enabling new perturbation experiments to study collective cell migration, such data imply that it may be possible to improve the wound healing process if we can design a biocompatible, DC-stimulation system that can shape the endogenous wound field present in epidermal wounds[24–27].

4.3 Galvanotaxis as a tool for collective control

The discovery that galvanotaxing cells orient and migrate in a specific direction relative to a direct-current (DC) electric field dates to the late 19th century[28], and a recent meta-study has suggested that electrically sensitive cell lines are the rule, not the exception[29,30]. Galvanotaxis has been implicated in cell movements in embryogenesis, morphogenesis, regeneration, and epidermal 'wounds'[27]. While the precise mechanisms driving galvanotaxis is under study (*Appendix* B), four mechanistic details are important.

1. Galvanotactic cues *do not* exert a bulk, electrophoretic force on cells.

2. Galvanotactic cues seem to act on the same downstream motility pathways as chemotaxis and general cell migration[29–31].

3. Epithelial galvanotaxis requires mechanical coupling amongst cells via E-cadherin[32].

4. While 'electric field' is the accepted nomenclature, it is **current density**, which is rarely reported, that drives cell motility (see *Appendix* ???*).

The remainder of this section will discuss the historical background of bioelectricity research and the implications for clinical wound healing.

4.3.1 Historical context[24,27,33–36]
Given the bizarre and tangled history of bioelectricity research, a brief discussion of the origins of the field along with the associated philosophical, scientific, and pop-cultural implications is included here. Not only does this strange story begin with some of the earliest work on *flowing* electricity, but also the dramatis personae comprise some of the greatest luminaries in Western science and medicine. What is most surprising given this is that so little of this work is remembered or taught today—a fact which we will briefly consider later. Prior to the 1780s, nearly all electrical research was concerned with the generation and properties of static electricity. What set Luigi Galvani's work apart was that he had, inadvertently, begun to study the flowing of electricity in an electrolyte. Galvani performed two key experiments that kicked off the next century of research

into bioelectricity. His first experiment was to demonstrate that static electricity transferred through a metal probe and into the sciatic nerve of a frog leg resulted in the twitching of the muscle. His second discovery was perhaps even luckier. His frogs sat upon iron grills, and he manipulated them with bronze probes. Using this configuration and probing a frog spine, Galvani observed muscular twitching with no apparent external electrical source (he was unaware of the electrochemical cell he had created). This second experiment in particular propelled him into the center of a raging debate in the scientific and philosophical communities—the debate between **vitalism** and **mechanism**. Vitalism, briefly put, maintained that there is something unique and special that set animate things apart from inanimate things. At the time, **vitalism** was also linked to the concept of "**spontaneous generation**"—the idea that life could come about spontaneously from material such as refuse (of which Erasmus Darwin was a strong proponent). After his second experiment, Galvani incorrectly came to believe that this 'vital spark' might be electricity, and he coined the phrase "**animal electricity**". It was this claim that particularly raised the ire of Alessandro Volta, the other electrical luminary of the time. Volta belonged to the camp of the mechanists who maintained that life was simply the result of myriad physical processes and could be described as such. In this capacity, Volta was able to demonstrate that the results of Galvani's second experiment were due to the use of dissimilar metals, rather than any intrinsic life force present in a frog limb.

However, this did little to counter the growing conflation of mysticism and electricity in the eyes of the public. For instance, the early 1800s saw Galvani's nephew, Giovanni Aldini, taking center stage in the public eye with his demonstrations of what had come to be known as *galvanism*. Of particular relevance is the manner in which Aldini went about demonstrating the potency of electricity. In his most famous demonstration (1803), Aldini was granted permission to *galvanize* the corpse of an executed criminal (one George Forster of London). During this demonstration, he is purported to have to induced winking and the motion of limbs by connecting the corpse to a voltaic cell. While he was unable to instill life in the corpse, the demonstration was an enormous public perception coup. Science, meanwhile, would take some time to catch up due to technical limitations in sensing and sourcing electricity. Historians of bioelectricity have subdivided the early development of electrical knowledge and technology into five regimes beginning in the 1660s and ending in the late 1800s. The first two regimes concern electrostatic discharge and storage (Leyden jars), before giving way to Volta's DC pile batteries in the 1800s. However, from here, it would take over a generation before knowledge and technology became advanced enough to enable formal monitoring and quantification of bioelectric phenomenon. During this time, Faraday developed the induction coil and Ørsted developed the theoretical links between electricity and magnetism. These matured in the 1830s, but during that time important things had happened in the world of bioelectricity pop culture. In 1818, Mary Shelley published the first edition of Frankenstein and this had, and continues to have, an enormous effect on the public perception of bioelectricity. While Shelley carefully never once mentions bioelectricity in the primary text, she writes in a preface to the third edition that *"Perhaps a corpse would be re-animated; **galvanism** had given token of such things, perhaps the…parts….might be…brought together and endued with vital warmth."*[34] To be fair, she deliberately avoided any specific claim, and a full reading of her preface reveals a fair amount of skepticism. However, the fact remains that there was an almost

tacit assumption, shared by both scholars and the public, that if any phenomenon had the power to imbue something with life, it would probably be electricity.

By the 1830s, the mechanists were finally able to take on the vitalists in a more quantitative fashion, as new, more sensitive galvanometers were now available. Using these tools, Carlo Mateucci made the first recordings of electrical impulses within muscles. Mateucci also made the first observations of the **injury potential**—an electrical signal that appeared during resections of muscles and nerves. Beyond these, he is also created one of the first organic-inorganic hybrid machines known as a Galvanoscopic Frog[37]. Here, he used an electrochemical junction coupled to two, amputated frog leg 'probes' to produce a galvanometer where the legs would twitch upon being simultaneously touched to something conductive. Approximately a decade after Mateucci first probed muscles, the man largely credited with starting the formal field of Electrophysiology entered the scene. Émile du Bois-Reymond was a physiologist who made the first quantitative measurements of the electrical properties of nerves (paving the way for the discovery of the action potential). In addition to this, he greatly expanded on Mateucci's work and demonstrated (using a cut in his own thumb) that all epidermal wounds have a characteristic electrical field. Known now as the **wound field**, this 1845 discovery is the scientific core, combined with the first galvanotaxis demonstrations of the late 19th c., motivated my original interest in using bioelectricity to control tissue and improve wound healing.

With the advent of these powerful new techniques and discoveries, mechanism quickly made headway against vitalism in the scientific community. A staunch mechanist, du Bois-Reymond once remarked that vitalism was "*a tissue woven of the most arbitrary claims, ... a murky empire of speculation.*"[38] However, as historian Alan Lightman explains: *"As biology advanced through the centuries, the vitalists rarely surrendered but instead retreated to smaller castles and less specific decrees."*[35] Moreover, electricity itself was a puzzle for the public as it combines 'action at a distance' and fantastical effects. In this climate, pseudoscience flourished, and it was simple for charlatan physicians to begin providing electrical medicines. The damage this has done is as subtle as it is staggering when we look back. Even today, discussions of the underlying bioelectric phenomena discussed in the remainder of this chapter are often greeted with surprise at scientific conferences, and modern scientific papers take great pains to establish a reputable scientific pedigree in their introductions. Brief histories similar to what we have just discussed are often presented alongside statements like the excerpt that follows, taken from a paper co-authored by two well known bioelectricity researchers: *"[I]n the past, bogus electrical therapies to 'cure' ailments ranging from impotence to baldness were common. 'Electric air baths', for example, were a popular Victorian spa treatment and, when Mary Shelley was writing Frankenstein, public demonstrations using electrical shocks to raise corpses were popular for their theatrical impact. **Much of the bad reputation associated with bioelectricity is rooted in this quackery.**"*[24]

This last statement is crucial—even today, bioelectricity research still bears a stigma from the events of the 19th c. (not to mention modern products such as 'abdominal muscle shockers' and the like). Moreover, as Martinsen and Grimnes explain of bioelectricity research in the 20th c., *"[t]he achievements are more specialized and of narrow impact, not so well known to the 'public at large'."*[33] Indeed, while most people today have a rough understanding of the electrical activity of nerves, action potentials, tissue

impedance, etc., very few (scientists included) are familiar with the foundational work that led to these discoveries, such as the discovery of the wound field. This is a shame, but it also means there is a great deal of dusting and discovering to do in the historical archives.

At this point, apologies may be due to the reader. Frankly, this historical interlude is not necessary to understand the research described in this chapter. Perhaps a few sentences on du Bois Reymond's discovery of the wound field would have sufficed. However, given that there is still stigma associated with bioelectricity and confusion as to its origins, it seems to be the obligation of any author discussing the subject to address this up front.

4.3.2 Galvanotaxis and the 'wound field'

The discovery that galvanotaxing cells orient and migrate in a specific direction relative to a direct-current (DC) electric field dates to late 19th century work on single celled organisms.[28] A recent meta-study has suggested that electrically sensitive cell lines are the rule, not the exception[29,30]. Galvanotaxis has been implicated in cell movements in embryogenesis, morphogenesis, regeneration, and epidermal 'wounds'[27]. This latter point describes a possible effect of the 'wound field' discovered by du Bois-Reymond and discussed above. Restated—epidermal injuries give rise to a transient, DC electric field at the site of the wound, with the cathode (negative) centered in the wound itself and the field extending laterally around the wound into healthy tissue. The presence of these fields has been confirmed many times with precise, modern equipment. In mammals, they are on the order of 10 mV/mm and can last for 3-6 hours after injury. A great deal of *in vivo* and *in vitro* work has demonstrated that they have a strong effect on the healing process. The most striking example is seen in salamanders regenerating an amputated limb. If an external electrical source delivers a DC potential that amplifies the native field direction extending from the limb stump, the regenerating limb will grow too quickly, and too large. In contrast, if the external field countermands the native field and the direction of the field is changed, regeneration will not take place.

A question that commonly arises in galvanotactic literature is why cells might evolve to support navigating via an electric field in the first place. There are two primary explanations. The first is that the presence of these fields is, in itself, almost an emergent phenomenon. Consider the wound field—it arises when we damage the epidermis and allow access to the underlying tissue. Most body plans in nature consist of collections of tubes, and we are no exception. Break that tube and an electrochemical imbalance is created that gives rise to an ionic current and the associated electric field. We can extend this argument to development as a whole. Development encompasses all manner of processes where cells must navigate in response to internal and environmental cues. Perhaps it was advantageous for cells to possess this ability. Both of these explanations touch on the 'just-so' problem that arises in evolutionary explanations, and they do not necessarily describe the behavior of the single celled organisms that galvanotax. It may simply be that the composition of the lipid bilayer in eukaryotic cells and the charge on surface proteins renders cells susceptible to ionic currents. The specifics of this question are difficult to answer, especially as the precise mechanism, regardless of the cell line,

remains unclear. *Appendix* B provides more detail as to possible mechanisms in eukaryotes.

4.4   Experimental methods

The experimental methods can be grouped into three categories: galvanotaxis chamber and electrical stimulation, cell culture, and microscopy. Following a discussion of these, the next section will address analysis techniques.

4.3.1   Galvanotaxis chamber design

Galvanotaxis chambers have scarcely changed since they were introduced 35 years ago[39–41]. Their primary goal is to deliver a DC current to a biological sample. Typically, agar salt bridges couple current into a shallow channel containing cells (see *Appendix B*). Two methods for assembling such chambers have been used. The most common one comprises a tunnel formed from glass coverslips and silicone grease. While effective, this method is slow, produces only unidirectional fields, and is difficult to standardize due to assembly variability[32,42,43]. The second method uses a microfluidic chamber (commercial, soft lithography, or tape-based) for better field shaping, but this does not allow population patterning[44–46]. Nearly all prior data were derived from isolated cells rather than monolayers.

We constructed a galvanotaxis chamber around pre-patterned cell monolayers, which allowed independent control of both the electric field and monolayer characteristics (Fig. 1, Methods). First, we simulated the desired electric field profile (Fig. 1, 'Design') and used an inexpensive, computer-controlled cutter to cut a 150 μm thick, double-sided, silicone adhesive *foundation* (comprising the chamber walls), and a 250 μm thick silicone *cell stencil* into arbitrary patterns. The foundation layer was adhered to a tissue culture compatible surface (Fig. 1, 'Design'), after which the stencil was placed into the stimulation area and seeded with cells (Fig. 1, 'Add Cells'). Once the cells had adhered and formed intercellular junctions, the stencil was removed, an acrylic frame was affixed to the foundation tape, and media was added to the reservoirs (Fig. 1, 'Make Channel'). The acrylic frames were produced using a laser cutter, allowing for arbitrary planar geometries. Lastly, agar salt bridges were run into the two chamber reservoirs and connected via saline reservoirs to a power supply under computer control. During experiments, media exchange was facilitated using an evaporative pump to draw fresh media gently into the stimulation chamber. Galvanotactic behavior was not affected by the direction of media flow, and the flow rate was kept low (at most 100 uL/hr). Please see *Appendix* B for design principles based on current density manipulation.

3 MAKE CHANNEL
remove stencil
affix cover to tape
add media
add salt bridges

2 ADD CELLS
cut/place stencil
add cells to wells
let cells adhere

*design/cut truly arbitrary geometries
of field chamber and cell patterns*

1 DESIGN
simulate
cut tape layer
affix to Petri dish

Ag/AgCl anode · current supply · Ag/AgCl cathode
salt bridge · Electric field in channel · cover · salt bridge
saline tape · tape saline
phase contrast objective

Figure 1. Stimulation chamber design

Overview of the design and assembly process (order is bottom to top). *'Design'*: the chamber is simulated and the foundation tape is cut and placed. *'Add Cells'*: the stencil is cut, placed, and loaded with cells. The MDCK-II dinosaur monolayer (right) demonstrates the versatility of the patterning method (scale is 1.5 mm). *'Make Channel'*: once the cells adhered, the frame is attached and the reservoirs are loaded. The schematic (right) is a cross-section of the stimulation chamber and shows the assembly of the electrochemical cell.

4.3.2 Electrochemical methods

The most common electrochemical method for delivering continuous DC current to cells is the silver:silver chloride (Ag/AgCl) electrode. As shown in Fig. 1 (upper right), power is routed from a supply (current controlled) through the electrode (the anode) into a saline reservoir, through an agar salt bridge, through the tissue sample, through another salt bridge and saline reservoir, back out a second electrode (the cathode) and into the ground of the supply. Ag/AgCl is used due to its ability to reduce pH changes in the sample itself by minimizing the production of dangerous ions such as $H+$ and $Cl(-)$ (which will form chlorine gas). The Ag/AgCl surface also serves to minimize losses to the electrical double layer that forms during stimulation, thereby improving the efficiency of the potential drop across the sample. These benefits come at the cost of corroding the electrodes out, limiting their practical lifespan. Steps can be taken to improve electrode lifespan by increasing the surface area by using coiled wire and pre-treating the wire to an acid etch. We used ~2.5" of 1 mm diameter silver wire per electrode, and pre-treated the wires in nitric acid (1:3 with water) for 30 sec to roughen the surface. Subsequently, wires were immersed in bleach for at least 24 hrs. While a variety of chloridation methods exist (including push-pull power supplies), bleach immersion is the most common and facile method. Properly treated wires will take on a purple-grey hue. Care must be taken to leave an untreated region at one end to allow

coupling to the power supply. The AgCl surface is reputed to be photosensitive, and we stored all wires opaque containers. A well-treated wire could easily last over several 6 hour experiments, although care must be taken to monitor the potential being drawn by the current-controlled power supply. Spikes in the voltage mean that the electrical double layer at the electrode surface in the saline solution is growing and that the electrode is likely to fail soon.

The electrodes connect the power supply to the sample via a saline reservoir and agar salt bridge. The saline reservoir, typically 50 mL per reservoir, serves as a buffer against electrochemical byproducts that might damage cells and serve to couple the current into the agar salt bridges without damaging the bridges (by plunging the wire into the agar directly, for example). While Steinberg's saline solution is the most common, phosphate-buffered-saline can be substituted along with a variety of other saline solutions.

The agar bridges provide the primary defense as they act as a diffusion barrier against harmful byproducts diffusing into the cell chamber. Agar bridges were prepared by adding 1.5% agar dissolved in phosphate buffered saline (PBS) containing calcium and magnesium to flexible tubing (1 cm outer diameter, and 0.75 cm internal diameter). Each bridge was then placed into a separate reservoir in the stimulation chamber (Fig. 1). An extra acrylic plate was cut to hold these bridges in place (optional). The exposed ends of the bridges were then placed in two separate beakers filled with Steinberg's solution. Agar bridges were made fresh before each trial.

Once the bridges, reservoirs and wires were prepared, the wires were connected to the positive and negative terminals, respectively, of a current-controlled power supply (Keithley 2400). This power supply was under computer control via a GPIB interface to MATLAB (Mathworks, Inc.). Custom scripts were written to activate, set and monitor the output voltage of the supply. Meanwhile, real-time monitoring of the voltage drop across the stimulation region of the chamber was accomplished using Ag-AgCl sense electrodes positioned on either side of the stimulation chamber and monitored by the computer via a myDAQ card (National Instruments).

4.3.3 Cell culture

All experiments used MDCK-II (G-type) cells from the Nelson Lab at Stanford University. MDCK-I cells were a kind gift from Prof. Karl Matlin (Univ. of Chicago). All cells were adapted for culture in customized media (low glucose DMEM, 1 g/L sodium bicarbonate, and penicillin-streptomycin). Cells were maintained at 37.5°C and 5% CO_2 in air. Imaging was carried out with media supplemented with 20 mM HEPES. Despite the ubiquity of MDCK cells, there is little agreement over the appropriate media, and most labs formulate their own media. The cells are quite hardy and can be adapted for a variety of media, although their galvanotactic performance can be affected by media selection. Further, long time-lapse experiments require some form of pH control in the media to balance metabolic acidification. MDCK in particular will rapidly acidify their media, especially in a small chamber such as was used here. In the absence of a CO2 control system built into a microscope incubator, it is common practice to use some

form of buffer solution. HEPES is the most common, although it is troublesome to work with. We found that HEPES supplementation performed best when prepared fresh before each experiment, rather than from a pre-made stock. A well-prepared HEPES imaging medium (and salt bridges) prevented significant pH change over at least 6 hrs. Gentle media perfusion in the sample chamber can also aid in pH stabilization.

4.3.4 Microscopy and image processing

The stimulation system was assembled in a tissue culture hood and then transported to a Nikon Ti-S microscope equipped with a XY motorized stage. The system was secured to the stage using hot glue, and the wiring was conducted as described above. Hot glue makes an excellent, low-cost fixation method. Considering that commercially available plate holders and stage inserts can run upwards of $600/insert, this is a good alternative. When using hot glue, care should be taken to ensure that the glue does not get under the dish being stabilized to avoid leveling issues. The whole microscope was enclosed within a customized temperature-controlled chamber set to 37.5 °C and referenced to the media temperature within the stimulation chamber. All experiments were conducted using either 5X or 10X phase contrast objectives, and image acquisition was controlled by the open-source MicroManager package. The time between frames was either 3 or 5 min., as stated in the text. Post-processing of all images was performed using either FIJI or MATLAB. First, images were stitched together to create composite images of each individual population. Following this, entropy filtering was used to fully remove the background prior to PIV analysis (4.4).

4.4 Collective analysis: image-based analysis and quantification

Over the last decade, a great deal of the work in collective motion (especially cell migration) has involved the use of Particle-Image-Velocimetry (PIV)[477,8,10,14]. This section will discuss the conceptual background of the PIV method as well as introducing a visualization method that has never before been used with cellular data. Following this, we will briefly discuss how certain statistical mechanics concepts can be leveraged to quantify the resulting data.

4.4.1 Particle Image Velocimetry (PIV)

Originally developed for use in aerodynamics research, PIV is an image correlation method that can be used to reveal flow dynamics. As migrating epithelia have been shown to exhibit a variety of flow behaviors, the algorithm is conceptually well suited for use, although it needs some adaptation. **Details aside, the overall goal of cellular PIV is to create velocity vector fields that describe the patterns of motion within a cellular collective.** Given this, one of the primary attractions of PIV for cellular work is that it can be used to describe cellular collective motion at cm^2 scale *without requiring tracking of the individual cells*. It should be stated that PIV is specifically *not* a tracking algorithm, meaning that if individual cellular trajectories are required the raw PIV data must either be carefully post-processed or manually tracked. Finally, cellular PIV is significantly simpler than traditional PIV as it requires only phase contrast (or high

contrast) microscopy as opposed to the laser sheets and high-speed cameras used in traditional PIV.

In its simplest form, cellular PIV begins with two sequential microscopy image frames of migrating cells that will be converted into a vector field. A PIV vector field describes how Image 1 must be shifted to become Image 2, and is represented as a field of velocity vectors describing motion within the sample. In order to calculate the field velocities, Image 1 and Image 2 must be correlated in some way. Generally, the algorithm then uses correlation peaks to determine which regions of Image 2 correspond to which regions of Image 1. From these data, the algorithm can calculate the shifts required to map Image 1 to Image 2 and generate the matrix of velocity vectors. Figure 2 depicts a sample of the process applied to a small region at the edge of a patch of cells.

Cell data from consecutive frames   PIV Vector Overlay   LIC Overlay
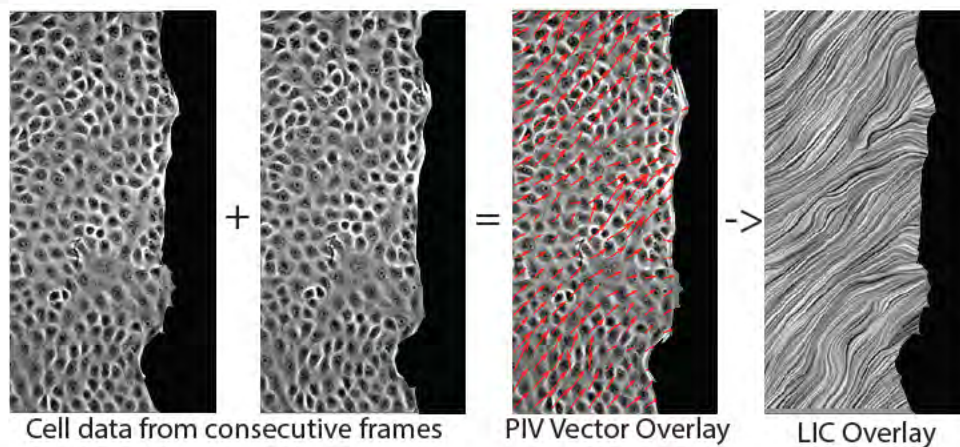
Figure 2: Sample process flow for PIV image analysis
Here, two consecutive images are correlated for PIV to produce the vector field shown in the third image. Note that the two consecutive images *are* slightly different. The final image presents the LIC visualization method discussed in 4.4.2.

When adapting PIV to cellular data, there are two primary concerns. The first is that the PIV algorithm was originally intended for use on extremely high contrast images of tiny illuminated oil or smoke particles spread out across a dark field (aerodynamics testing). Traditional brightfield microscopy cannot offer such contrast (resulting in confounding noise), while fluorescent microscopy during extended time-lapse experiments can cause phototoxicity and bleaching. Fortunately, simple phase contrast microscopy can generate sufficient contrast and texture for accurate correlation. A second concern is that PIV correlations break down if there is too much of a change between Image 1 and Image 2. Given this, the microscopy sampling rate must be empirically tuned for a given experiment and type of cell. If the sampling is too slow (15-30 minutes between frames for MDCK), correlation accuracy can be reduced. Alternately, if it is too fast (~30-60 seconds), membrane fluctuations and CCD noise are detected during correlation and the data becomes noisy. For most epithelial cells, 5 min/frame represents a good starting point.

PIV analysis is often performed using existing software packages. For this work, we chose to use PIVlab (William Thielicke, University of Applied Sciences, Bremen), which is a free package for MATLAB and performs a full suite of PIV analyses as well as many post-processing operations. The core operating parameters to consider when using PIV are discussed below.

- The PIV Window: For a given frame of migrating cells, a PIV comparison window must be selected. The size of this window depends on the resolution required in the analysis, but often encompasses several cells. The algorithm will raster this window across Image 1 and search for correlates in Image 2 via cross-correlation. The region in Image 2 exhibiting the highest correlation peak is assumed to be the match. We opted to use a window size of 32x32 pixels or 64x64 pixels. We tried to keep the number of cells within a window to between 5-10 cells.

- Window Overlap: In order for the algorithm to raster the PIV window across the image, it must know how much to translate the window. While the window could be moved one full window width, this tends to reduce accuracy at the interface between windows. Instead, an overlap percentage varying between 25% and 50% is often chosen (we used 50%).

- Frame sampling order: Given Frames A/B/C/D, there are two primary ways to pair the images for PIV processing. The first is called AB/CD pairing, where frames A and B are analyzed as a pair, and frames C and D are analyzed as a pair. While fast, this is less accurate then the alternative AB/BC pairing, which is what we used. Here, A is paired to B, and B is then paired to C for the next frame. AB/BC pairing results in N-1 PIV vector fields for a stack of N images.

- Correlation algorithm: There are two primary methods of performing PIV. The first is direct cross-correlation (DCC) which is based on performing a template search within an image using matrix cross-correlation. As traditional cross-correlation can be implemented using Fast-Fourier Transforms, many software packages offer both matrix algebra and FFT correlation methods. Other methods, such as 'minimum quadratic difference' (MQD), based on similar underlying equations are also popular, and it is ultimately up to the user to find the most effective method for a given application. For instance, while MQD is analytically more accurate than DCC, it is vulnerable to artifacts such as CCD pixel noise when applied to real-world data[48]. For our data, we compared FFT and DCC correlation methods and ultimately chose DCC as it ran faster than multi-pass FFT and with similar accuracy.

4.4.2 The Line Integral Convolution

Vector fields are powerful quantitative tools, but are often difficult to study by eye for large fields as the vector density in the rendering tends to mask flow patterns. Imagine a 50x50 array of the vector panel in Fig. 2 and the problem becomes apparent for large fields of view. In such cases, there are simply too many vectors in the image at one time, and down-sampling the field similarly masks patterns. This problem has been

addressed in computational fluid dynamics through a method known as 'texture convolution'. Texture convolutions convolve a vector field with a texture map (lines, checkerboards, noise, etc.), and the resulting image represents how the texture pattern would be affected in the flow field. In essence, texture convolutions are similar to tracking fluid streamlines, but they are easier to visualize. The most common convolution for PIV data is to convolve the vector field with an equally sized field of 'noise'. The feature size of the noise and the type (white, brown, pink) affect the resulting image, but the overall output appears as correlated streaks reminiscent of the brushstroke textures in a painting (see the final panel in Fig. 2). The particular convolution method favored for PIV is called a Line Integral Convolution (LIC) and was first proposed by Cabral and Leedom in 1993[49]. The major drawback of the LIC is that it loses directionality information. The streak pattern does not describe in which direction along the pattern a particle would travel. This can be addressed by merging the LIC with a velocity heat map (color) that indicates the direction of motion. This colorized LIC is incredibly well suited to visualizing cellular collective migrations, but has not, to our knowledge, been previously employed for this purpose. All of our LIC operations were performed in MATLAB using the FastLIC algorithm implemented in the Vector Visualization Toolbox (Nima Bigdely Shamlo, UC San Diego) to generate the LIC and custom scripts to produce the colorized form.

4.5 Data from collective engineering of epithelial migration

Five core experiments comprise the data and demonstration of how galvanotaxis can be used to engineer collective cell migration. First, we demonstrate how on-demand U-turns can be implemented at a population level. Second, we investigate how a multi-directional, 2D electric field can invoke local responses in a tissue. Third, we explore how population geometry and size affect the controllability of a cellular collective. Next, we take a closer look at how the border zones of a population drive geometric effects. Finally, we highlight how the galvanotactic migration cue overrides certain other cues, such as contact inhibition and can inexorably drive cells against an obstacle.

4.5.1 Epithelial monolayers perform complete, collective reversals via local 'U-turns'

Single keratocytes presented with a galvanotactic cue migrate in one direction, and a subsequent cue in the opposite direction causes cells to make a 'U-turn' rather than repolarizing and reversing direction[29]. This response is straightforward for single cells, in which neither speed nor turning are compromised by the presence of neighboring cells. In contrast, U-turns would seem more difficult in a cell monolayer, since each cell in a monolayer is physically coupled to neighboring cells and the mean speed in a monolayer is significantly slower than that of a single cell. Rather, such intercellular coupling would more likely induce jamming (lack of reorientation), or gradual repolarization of the cell and subsequent reorientation.

To examine if and how junctioned epithelial cell monolayers change direction, we patterned a 3 x 3 mm monolayer into the center of a 13 x 5 mm galvanotaxis channel (see Fig. 1, Simulation). This geometry prevents sidewall contact from biasing cell

behavior. After 12 hours, cells in the monolayer had formed cell-cell junctions and were stimulated at 0.3 mA/mm^2 (~ 5 V/cm) to induce leftward migration (these MDCK-II cells migrate cathodically). Once ordered, we reversed the field polarity to induce rightward migration. Images were captured at 1 frame/3 min. Post acquisition, images were stitched together and analyzed using PIV (Methods) to capture flow dynamics by generating a velocity field for each frame pair (Fig. 3, right). The degree of order in a population was assessed by the order parameter, ϕ, either parallel or perpendicular to the field; $\phi_\parallel$, ranging from [-1,1], is the ensemble average of the cosine of the angle of every vector, with respect to the direction of the field (Eqn. 1):

$$\phi_\parallel = \frac{1}{n}\sum_i \cos(\theta_i) \quad ; \quad \phi_\perp = \frac{1}{n}\sum_i \left|\sin(\theta_i)\right| \quad ; \quad \Delta\phi_\perp = \frac{\phi_\perp}{\langle\phi_\perp\rangle_t} - 1 \tag{1-3}$$

$\phi_\parallel$ captures the amount of order parallel to the direction of the field during stimulation (red curve, Fig. 3a). A clear reversal of migration from left (-1) to right (+1) was observed in response to a change in polarity of the field, although *how* the reversal occurred could not be inferred from these data alone. To detect such transitions, we defined $\phi_\perp$, the order in the direction perpendicular to the field axis, by modifying (1) to take the magnitude of the cosine, as in (2). This changed the range to [0,1], which was useful because any persistent upward or downward migration implied a U-turn, and taking the magnitude avoided cases in which local up and down migrations cancelled each other in the average. For visualization, we present $\Delta\phi_\perp$ (Eqn. 3), the percent deviation from the mean of $\phi_\perp$ (blue curve in Fig. 3a). The spike arising during the transition signifies that U-turns took place. The local dynamics shown in Fig. 3b-e explain how U-turns occurred. Rather than being a systematic process in which the cell population turned up or down, this turning process was distributed spatiotemporally, with small patches turning down (Fig. 3c) followed by neighboring patches turning up (Fig. 3d). Eventually, these distributed U-turns were completed and the population as a whole began to migrate in the opposite direction (Fig. 2e). A surprising amount of symmetry existed in these maneuvers, as shown by plotting the motion as a kymograph (Fig. 3f, kymographs plot temporal change across a single row of pixels).

The speed and kinematics of how cell populations performed a U-turn were particularly striking. We patterned a new, 3x3 monolayer and focused on a single region to avoid stage drift. To capture the temporal dynamics, we used a sinusoidally oscillating field with periods ranging from 2.5 - 30 minutes (video sampling rates satisfied the Nyquist criterion for each frequency). The cycling data (Fig. 3g) show an ensemble response even at the 2.5 min scale. While faster responses likely occurred, limitations in PIV (Methods) prevented us from exploring this here. Regardless, these data belie the view that epithelial monolayers are cumbersome, but instead indicate that they have an extraordinarily fast, collective response to changes in galvanotactic cues.

4.5.2 Simultaneous, multidirectional control of migration within a single monolayer

The data above demonstrate that cell motions within an epithelial monolayer induced by a galvanotactic cue can have regions of localized order, even as the ensemble acts to follow the cue. While flocking animals (sheep, birds, fish) may move independently of

one another and can scatter or split, cells in an epithelial monolayer cannot as they are physically coupled to each other. Given this constraint, what level of spatial control can be achieved? We tested whether a shaped field could induce two contiguous regions within a single monolayer to diverge or converge from their shared border, or whether they would simply respond to the average field and remain stationary.

We patterned a 2x20 mm monolayer of cells within a chamber designed to produce an electric field profile capable of inducing either divergence or convergence in the monolayer depending on the field polarity. Figs. 4a-c show the monolayer and chamber geometry (note that the monolayer does not contact the side-walls), and a simulation of the field strength and streamlines. The chamber, shaped like a squat 'T', produced a tripartite field. The left and right zones were equivalent in magnitude but anti-parallel, while the central zone exhibited smoothly curving streamlines running from the lower terminal towards the distal terminals. The '+' and '-' in Fig. 4b indicate electrical polarity, with the unbracketed case inducing convergence (towards the midline) and the bracketed case inducing divergence (away from the midline). The monolayer underwent a one-hour control period (no stimulation), followed by one hour of convergent stimulation, and then a subsequent hour of divergent stimulation (~5 V/cm). Data were collected and analyzed as described above. To more effectively display the monolayer behavior, we performed Line-Integral-Convolutions (LIC) on the PIV data to generate a texture map that captures flow patterns (streamlines), which we overlaid with heat-maps of the velocity field to show directionality (Figs. 4d-f). Together, this method allowed visualization of dynamic flow patterns within a static image.

Without galvanotactic cues, monolayers (Fig. 4d) exhibited a low-magnitude, heterogeneous distribution of right-left velocities, with the LIC texture indicating dominant upward and downward cell migration. This behavior matches the expected behavior of a thin, epithelial stripe of cells[10,13]. A divergent field cue applied to the same monolayer induced rapid ordering and divergence along field lines (Fig. 4e); cells even followed the vertical field lines in the central zone. Moreover, the LIC texture clearly depicted the curving nature of the cellular flow pattern. Correspondingly, convergent cues produced convergent motion along the field lines (Fig. 4f). Taken together, the data show a monolayer exhibiting three distinct zones of motion that were precisely controlled by a single electric field and obeyed multiaxial field lines. Moreover, the entire flow pattern of the monolayer was reversible from divergence to convergence, enabling the application of complex, dynamic field geometries to achieve multi-directional control over migration.
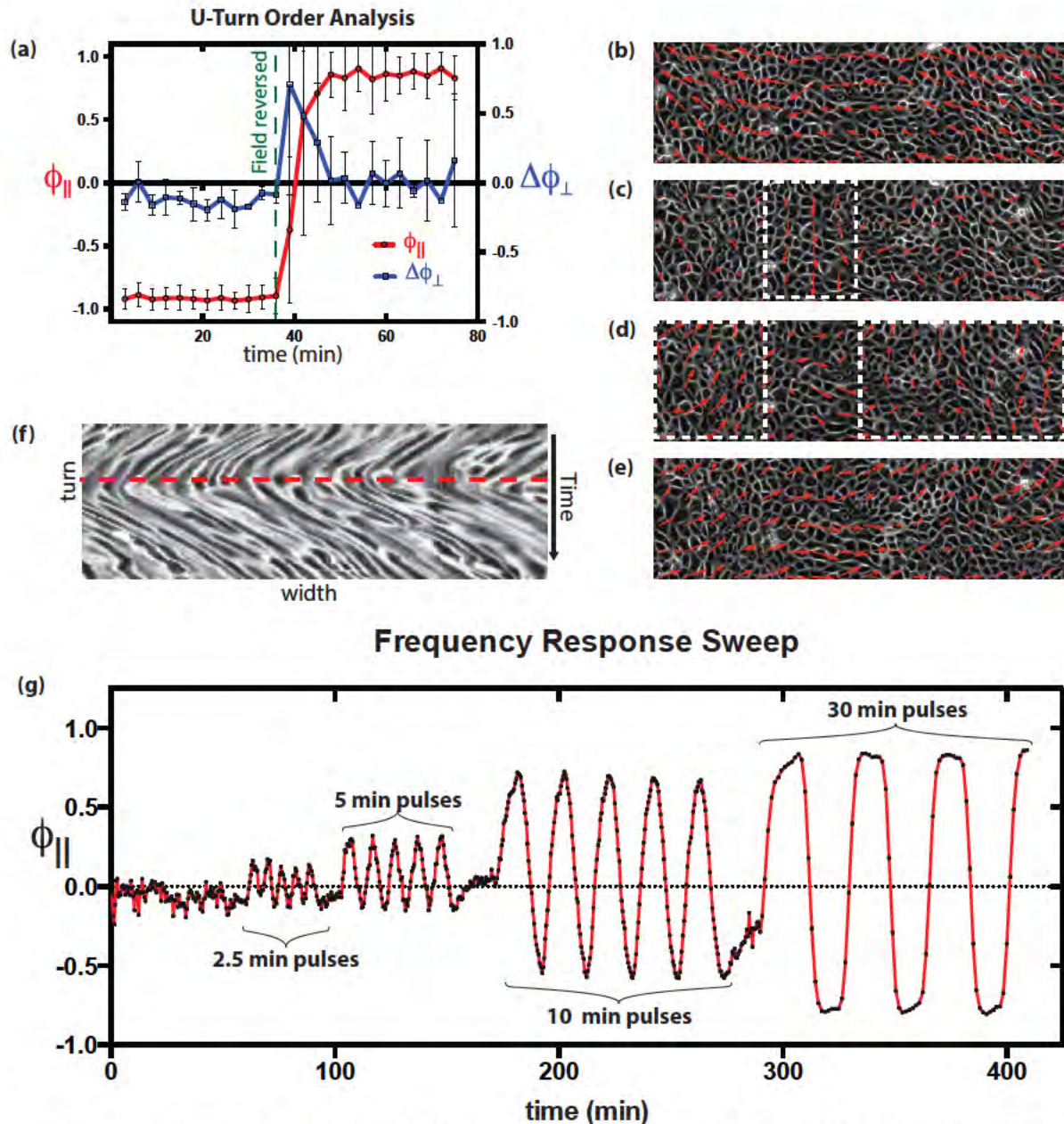
Figure 3: Galvanotaxing epithelial monolayers perform collective U-turns and respond rapidly. (a) Order analysis of a population-wide U-turn event. Error bars represent standard deviations for each time point. (b-e) Time course of local U-turn events (6 min between panels, panel width ~600 μm). (b) Leftward migrating population prior to field activation. (c) Downward U-turn initiation in the region bordered by the dashed white line. (d) Upwards U-turn initiation in the boxed regions. (e) Overall realignment towards the right. (f) Kymograph of a U-turn zone from a different experiment. Vertical dimension is time (5 min/row), and horizontal dimension spans ~750 μm. Red dashes indicate approximate turning region. (g) Temporal response data with cycling frequency annotated for each interval. Note that sampling rates for each pulse frequency were adapted to be > 3x the Nyquist frequency.

55
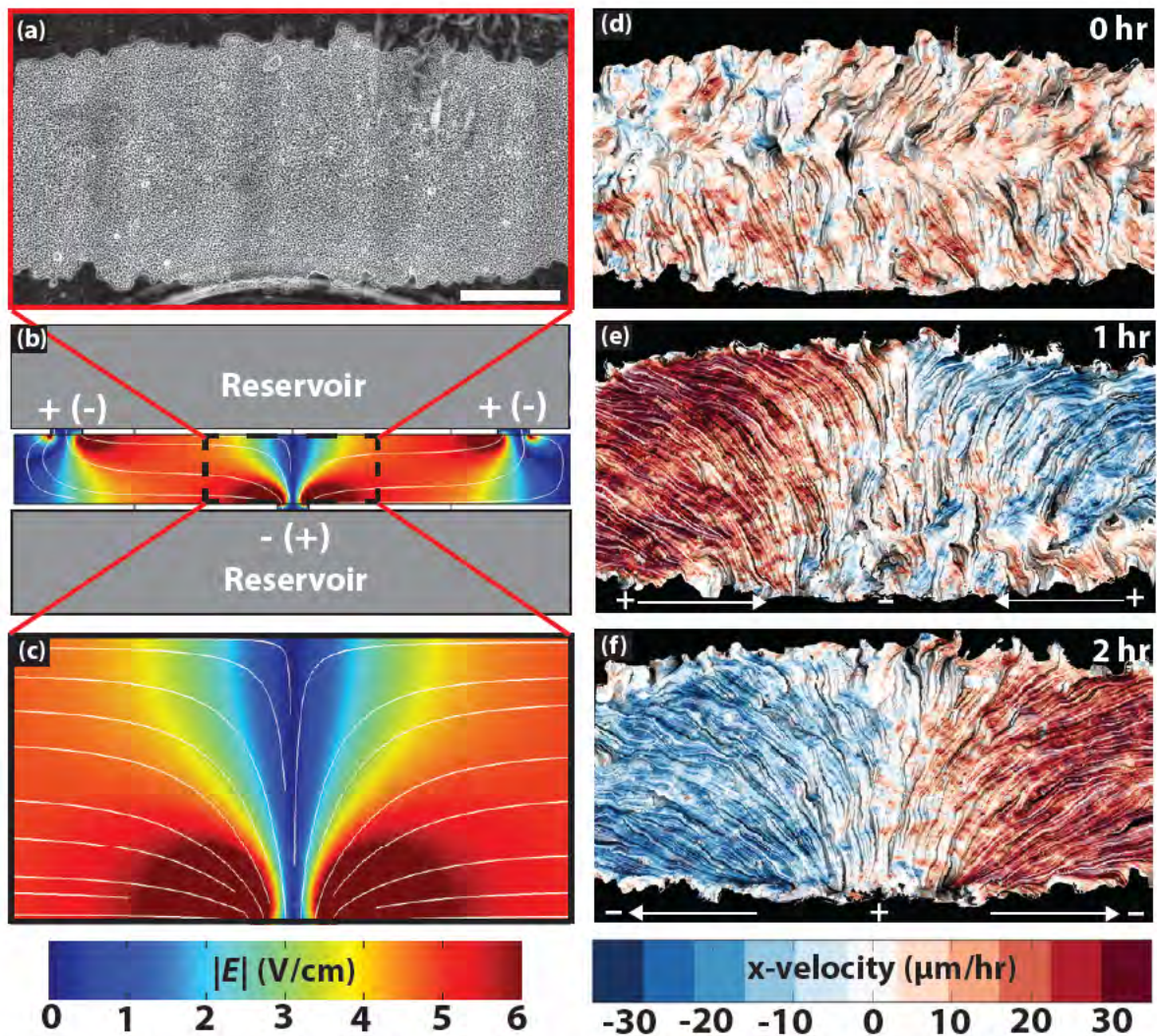
Figure 4: Epithelial monolayer migration follows field lines in 2D electric fields.
(**a**) 5x phase contrast image of the central zone of the monolayer (scale bar, ~800 μm). (**b**) Top-down view of simulated chamber. Media reservoirs depicted in grey, and stimulation zone colorized. The heatmap indicates the magnitude of the electric field, |*E*| (V/cm). All chambers can produce two field polarities, depending on location of the anode and cathode; the unbracketed + and - connote the electrical terminal polarity to induce divergent monolayer migration from the midline, and the bracketed (+) and (-) represent the reversed polarity case that would induce convergence towards the midline. (**c**) Magnified view of the region of interest (same zone occupied by the monolayer shown in **a**). (**d**) Monolayer behavior *prior* to field stimulation (time = 0 hr). Texture produced by LIC, color indicates *horizontal* velocity (μm/hr; red to the right, blue to the left). The monolayers in **a** and **d** are the same. (**e**) Monolayer behavior ~ 1 hr into divergent field stimulation. The white arrows, and + and - indicate the direction of the field (diverging here). (**f**) Monolayer behavior ~ 1 hr after field polarity reversal. Note the change in migration direction (see white arrows for field direction).

4.5.3   Population geometry influences the galvanotactic response

A hallmark of collective motion is that the borders exhibit behaviors that are different from bulk behaviors, and thereby the borders can affect bulk behavior[15,50]. We sought to understand how population size and shape would affect galvanotactic control of

collective migration. We patterned two square monolayers of different sizes (~5 mm^2 and ~25 mm^2) with different perimeter-to-area ratios (2 vs. 0.8, respectively). We hypothesized that the smaller population, with its more prevalent borders, would more strongly resist migration control than the larger population. Three replicates of each size were patterned into a single 10 x 26 mm chamber. All populations were seeded from the same stock of cells, and seeding volumes were scaled accordingly. We performed a time-lapse experiment (1 frame/5 min, 4X phase contrast) with 1.5 hrs of control data after which the field was activated at 0.3 mA/mm^2 (~5 V/cm). In controls, the LIC patterns show that the peripheries of both population sizes migrated normal to the perimeter, while the bulk zones had much less order (Fig. 5a). During galvanotactic stimulation, there was a dramatic shift in both the LIC and velocity magnitudes, with both cell populations becoming highly aligned and migrating markedly faster (Fig. 5b). However, despite alignment to the field in the bulk population, the LIC indicated that border migration was still normal to the perimeter.

To quantify these effects, we studied shifts in the order parameters. Fig. 5c presents $\phi_\parallel$ (left-right order, [-1,1]) averaged at each time point over all available data for the respective population sizes. We found that the smaller population converged on a significantly less ordered state than the larger population (0.6 vs. 0.8, respectively). This trend remained, albeit with higher net order ($\phi_{\parallel\,Large}$= 0.95, $\phi_{\parallel\,Small}$= 0.7), if we analyzed only the bulk of each population. While these data show how cell migration of the borders biased the bulk population, we could observe the converse case by considering the vertical order magnitude parameter, $\phi_\perp$ ([0,1], Eqn. 2). Plotting the overall order in the vertical axis throughout the experiment (Fig. 5d), we found that the population orders were stable through the control period, but began to decrease once the field was engaged. Such a decrease implies a switch from vertical to horizontal migration. Importantly, larger populations underwent a more dramatic decrease (~45%) in net vertical order than smaller populations (~20%). This implies that larger populations were better able to override the effects of the border regions owing to a more favorable perimeter-to-area ratio.

Finally, we quantified the field-induced increase in speed in the two population types. While the speed of both populations increased during stimulation, this shift was far more pronounced in the larger population (Fig. 5e). Furthermore, the same shift did not occur in the vertical velocity, so the effect was related directly to induced migration in the direction of the field. While it may seem that a larger population would be more cumbersome with its many more cells and intercellular junctions, we believe that the size-dependent effect is based on at least two phenomena. First, the LIC and order data showed that the large population was more ordered overall, resulting in a greater mean-free path. Second, the lateral edges of a population also affected cell migration (see Fig. 6), and a larger population was less susceptible to these affects in the bulk, again increasing the likelihood of greater velocity during directed migration than would occur in a small population.
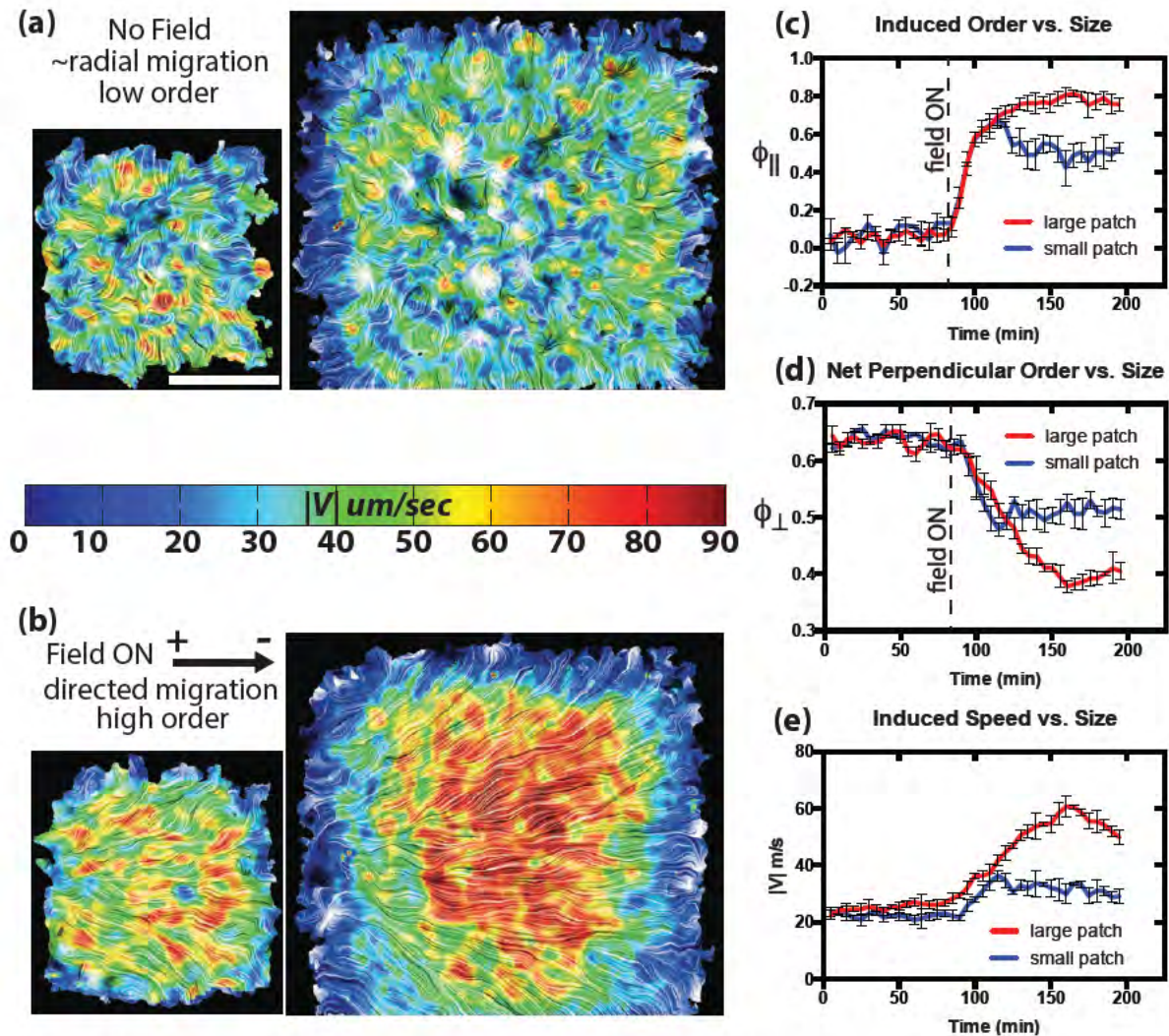
Figure 5: Monolayer size and shape affect galvanotactic controllability.
(a) LIC analysis of a monolayer prior to stimulation (scale bar, ~1 mm). The heat map is the velocity *magnitude*, |V| (µm/hr). (b) Representative LIC analysis after field stimulation (t ~ 150 min). Field direction is to the right (arrow). (c) Horizontal order analysis over time comparing small (blue) and large (red) monolayers (error bars from S.E.M., n=3). Dashed vertical line indicates the activation of the field. (d) Vertical order analysis over time comparing the small (blue) and large (red) populations (error bars from S.E.M., n=3). Vertical order was calculated as in Eqn. (2). (e) Velocity magnitude analysis comparing small (blue) and large (red) monolayers (error bars from S.E.M., n=3).

4.5.4 Leader cell dynamics are insensitive to induced collective behavior

The border effects examined above suggest a different type of border than other collectives that lack physical junctions between neighbors (e.g., birds, fish, sheep, etc.). Where the envelope of a flock of birds will translate through space (i.e. the whole flock moves in the same direction), galvanotaxing cell monolayers do not as the borders are less susceptible to galvanotactic guidance. We attribute this difference to leader cell dynamics, as leader cells are unique to the border zones and are known to play a role in

collective migration[9,13,51]. While the specifics of the roles of leader cells are constantly being refined as new traction force data are obtained[9,13], we assume that leader cells exert some level of local directional control of cell migration at borders of galvanotaxing monolayers. Furthermore, epithelial leader cells are known to be phenotypically distinct from the interior cells[10], and perhaps this difference prevents them from responding to galvanotactic cues. Fig. 6a highlights this effect with a slice of PIV vector data taken from the side of a square monolayer, where a leader cell, distinguished by its semilunar profile and lamellipod, protrudes perpendicular to the electric field. The vector field shows a smooth transition from highly ordered bulk cells (left) to the 90-degree shift taken by the leader cell (right).

Interestingly, leader cells migrated parallel and anti-parallel to the electric field. Fig. 6b demonstrates how the borders of a narrow monolayer within a rightward field still migrate normal to the perimeter. While this is expected for symmetric monolayers (Trepat), the colorized LIC (heat-map for horizontal velocity) depicts how the majority of the population galvanotaxed rightward, while leader cells on the left front kept migrating leftwards, with the result that the population as a whole became stretched (see 'post field', Fig. 6b). The kymograph in Fig. 6b shows how the population began moving uniformly rightward before the leader cells on the left began to reverse direction (arrow in the kymograph).

To test whether leader cells were responsible for this behavior, we inhibited leader cells by confining the monolayer within the stencil until immediately before the experiment. The stencil walls inhibited lateral growth and prevented leader cells from polarizing, and it took up to 3 hrs for leader cells to reform following removal of the stencil. We expected that the monolayer would expand overall if leader cells were present, even during galvanotactic stimulation, whereas the monolayer would contract during stimulation if leader cells were absent. Once stimulated, the leader cell-free monolayer migrated in the field direction. Significantly, the trailing edge underwent a dramatic contraction (~325 μm) towards the midline as there were no leader cell forces to balance the monolayer stress. Furthermore, the leading edge of the monolayer remained stationary without the guidance of leader cells. Lastly, the slopes in the kymograph (Fig. 6c) show that the trailing half of the monolayer moved more quickly than the leading half, perhaps because the rapidly moving trailing half was pulling against the now slow moving leading half. Overall, the data demonstrate a key difference between traditional flocking systems and a junctioned monolayer, and show how the presence and placement of leader cells can affect the control of population level migration.
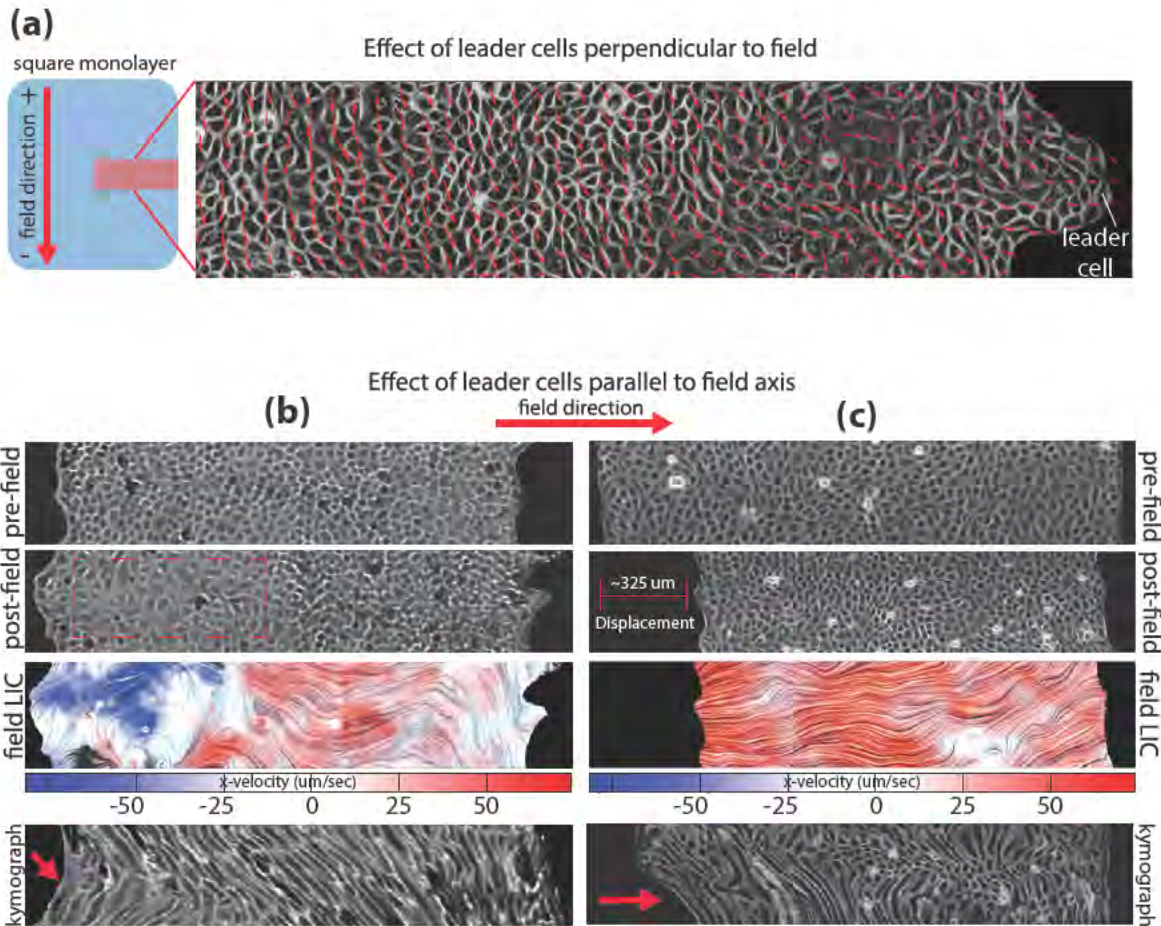
Figure 6: Leader cells are insensitive to galvanotaxis.
(a) Behavior of leader cells perpendicular to the field axis; left, stylized monolayer emphasizing field orientation relative to the region of interest (red box); right, PIV vector field from the region of interest, leader cell identified with an arrow. **(b, c)** Effects of leader cells parallel to the field axis (left to right, red arrow). Column **b** shows data from a monolayer with intact leader cells, while Column **c** data was from a monolayer without leader cells (panel width ~2.1 mm). As each column has the same layout, they will be described in parallel here. The 'pre-field' and 'post-field' panels present the change in the monolayer after field stimulation. Note the cell packing density change in the Column **b** 'post-field' panel, and the 360 μm trailing edge contraction in the Column **c** 'post-field' panel. The 'field LIC' panels show the LIC taken from the 'post-field' data. The Column **b** LIC data demonstrates bidirectional migration, while the Column **c** LIC indicates nearly unidirectional migration. Kymographs were computed over the entire experiment for each case. The red arrow in Column **b** kymograph identifies when the trailing edge leader cells began to migrate antiparallel to the field. The red arrow in Column **c** kymograph focuses on the dynamics of the trailing edge contraction.

4.5.5   Galvanotactic cues are obeyed despite monolayer obstacles

Since these data show that galvanotactic cues dominate in the absence of border effects, we explored whether we could force galvanotaxing monolayers to migrate against an obstacle. Traditional obstacles are made from micro-patterning cell adhesion blocking areas with chemicals[11], and micro-fabricated walls. However, both of these obstacles produce borders in the population that would bias the resulting behavior. Moreover, the strongest galvanotactic effects occur in the monolayer center, and not at the edge that would contact these obstacles. Taking advantage of this fact while avoiding border

effects, we leveraged Abercrombie's 1950s experiments on monolayer contact inhibition to produce a cell-based obstacle within the monolayer itself[52]. Fundamentally, epithelia (such as MDCK monolayers) are contact inhibited in migration, meaning that they rarely violate planar culture conditions by overlapping each other out of the plane[52], even when two monolayers fuse at the mid-line. This is especially true in cases where contacting monolayers share cell-cell junction proteins, as is the case of homophilic E-cadherin adhesion by MDCK-I/II cells. Using this principle, we patterned contiguous 25 mm^2 monolayers of MDCK-I and –II cells and over 16 hours allowed the monolayers to fuse at the interface, which became the midline of the resulting hybrid monolayer. The obstacle itself came from two design details. First, by patterning a saturating density of MDCK-I cells, we reduced their mean migration velocity, thereby making one half of the hybrid monolayer less motile. Second, MDCK-I cells galvanotax anti-parallel to the MDCK-II cells used in this study. When combined with the high density cell seeding, the MDCK-I half of the monolayer effectively served as a wall against which the MDCK-II cells were driven via a unidirectional electric field (0.3 mA/mm^2).

The collective response was surprising (Figs. 7a-c). For ~5 hrs, MDCK-II cells continued to migrate (with elevated velocity) directly against the MDCK-I boundary wall despite the immobility of the boundary and relatively stationary MDCK-I cells. Figs. 7a, b show both an x-velocity heat-map and corresponding spatial mean profile of this behavior, while Fig. 7c shows the kymograph of the entire experiment including the control period. Two cell behaviors are striking. First, the sharp drop-off in the velocity profile indicates a surprisingly rapid deceleration at the interface. Despite this, no propagating effects distal to the border were observed. Second, this behavior induced cells to 'pile up' at the interface, resulting in increased local cell density that far exceeded that of confluent control MDCK-II cells in which contact inhibition regulates local density and cell proliferation[7,53]. These data are consistent with cells locally acting on galvanotactic cues, and imply that galvanotaxing monolayers obey Abercrombie's rule of contact inhibition[52].

4.6 Collective engineering as a design approach

Our results strengthen the concept of tissues as active materials, which possess emergent behaviors that can be manipulated by appropriate stimuli. This framework allows us to provide a 'task' ("migrate left", "reverse migration direction") to the tissue without specifying a solution trajectory. This allows the tissue to respond locally while still producing a predictable, global outcome. This is clearly seen in the U-turn data when the population reverses direction via distributed U-turns of small groups of cells (Fig. 3). Even the rapid response time may stem from this local interpretation of commands, which may also explain why we were able to induce complex spatial behaviors in these cell monolayers (Fig. 4). These nuances are surprising, especially given the overriding nature of the response, as shown in Fig. 7 in which an MDCK-II monolayer relentlessly collided with a stationary wall of MDCK-I cells. Indeed, the dominant nature of this phenomenon enhances the 'compass' explanation of galvanotaxis[29]. However, while this example is powerful, it is fundamentally limited by population geometry and size (Figs. 5-6). For instance, altering the perimeter-to-area ratio dramatically affects the controllability of induced cell behavior. While the monolayer response is still predictable, the borders must be taken into account,

especially given the insensitivity of leader cells to galvanotactic cues. These points clearly illustrate some of the key differences between junctioned monolayers and traditional swarming organisms that lack physical coupling.

Galvanotaxis may be clinically useful for wound healing applications, but the approach is not limited to electrical stimulation or application to epithelia. Ultimately, we may be able to develop a suite of 'sheepdog' analogs that allow similar control of a variety of different tissue types and tissue engineering applications. Our goal in this work was to demonstrate that such control is possible and to provide a unique platform and set of assays for exploring this further.
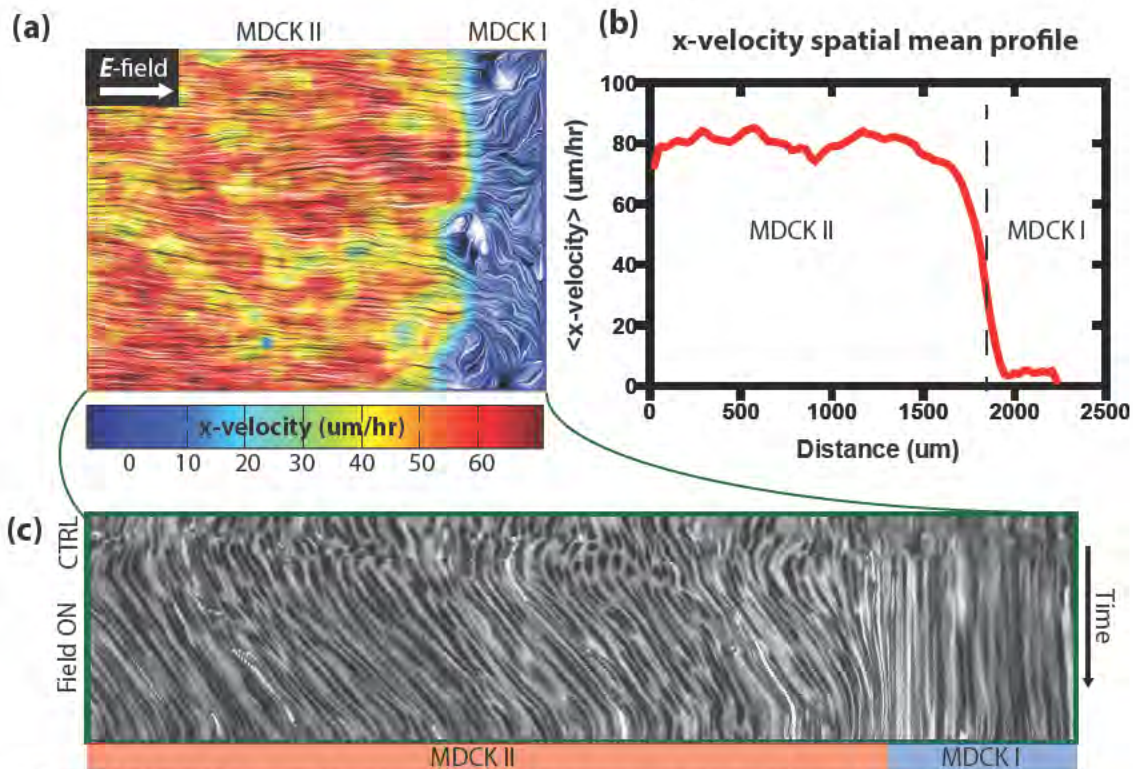
Figure 7: MDCK-II monolayers galvanotax against co-cultured obstacles.
(a) LIC of MDCK-II monolayer (left) colliding with MDCK-I monolayer (right). Heatmap is horizontal velocity, and the field points to the right (panel width ~2.1 mm). (b) The velocity spatial mean profile was calculated by averaging the velocity over each row of **a**. Note the rapid drop-off in velocity at the collision interface. (c) The kymograph was analyzed over entire duration of the experiment. Note the stability of the velocity (slope) throughout the MDCK-II monolayer, despite the stationary cell wall formed by the MDCK-I monolayer.

Chapter 5
Closing Remarks

Forþon nu min hyge hweorfeð
ofer hreþerlocan,
min modsefa
mid mereflode,
ofer hwæles eþel
hweorfeð wide,
eorþan sceatas
cymeð eft to me
gifre ond grædig;
gielleð anfloga,
hweteð on hwælweg
hreþer unwearnum
ofer holma gelagu.
-The Seafarer, c. 900 BCE

Looking back, I hope you have come away with a better sense of how some of the myriad myriads in the world accomplish what they do; be it flocking, schooling, swarming, herding, or otherwise interacting according to a collective verb. To reiterate, the purpose of this dissertation was not to provide an exhaustive overview of collective behaviors or collective engineering methods, nor was it to even formally define collectivity and emergence. Rather, it was to sweep through three vastly disparate fields and show how the same perspective and paradigm can be applied to each field to get a better sense of how things work and to inspire new engineering and design methods. Obviously, this sounds somewhat idyllic and grandiose. Collective engineering is not going to be a panacea to our problem-solving woes. Many problems we face are best solved using traditional engineering methods. However, more tools in the toolbox should only help us. The bigger problem is likely determining when to apply collective engineering and, as always, learning how to ask the right questions.

References

Chapter 1 References

1.   Johnson. *Emergence*. (Scribner, 2002).
2.   Strogatz. *Sync*. (Hyperion, 2004).
3.   Gordon. The rewards of restraint in the collective regulation of foraging by harvester ant colonies. *Nature* 3–6 (2013). doi:10.1038/nature12137
4.   Aristotle. *Metaphysics*. Book H, 1045a 8–10
5.   Gallagher & Appenzeller. Beyond Reductionism. *Sci.* **284 ,** 79 (1999).
6.   Goldstein. Emergence as a Construct: History and Issues. *Emergence* **1,** 49–72 (1999).
7.   Corning & Alto. THE RE-EMERGENCE OF " EMERGENCE ": *Complexity* **7,** 1–21 (2002).
8.   Tambe, Hardin, Angelini, Rajendran, Park, Serra-Picamal, Zhou, Zaman, Butler, Weitz, Fredberg & Trepat. Collective cell guidance by cooperative intercellular forces. *Nat. Mater.* **10,** 469–75 (2011).
9.   Ballerini, Cabibbo, Candelier, Cavagna, Cisbani, Giardina, Lecomte, Orlandi, Parisi, Procaccini, Viale & Zdravkovic. Interaction ruling animal collective behavior depends on topological rather than metric distance: evidence from a field study. *Proc. Natl. Acad. Sci. U. S. A.* **105,** 1232–7 (2008).
10.   Cavagna, Cimarelli, Giardina & Parisi. Scale-free correlations in bird flocks.
11.   Anon, Serra-Picamal, Hersen, Gauthier, Sheetz, Trepat & Ladoux. Cell crawling mediates collective cell migration to close undamaged epithelial gaps. *Proc. Natl. Acad. Sci.* (2012). doi:10.1073/pnas.1117814109
12.   Angelini, Hannezo, Trepat, Marquez, Fredberg & Weitz. Glass-like dynamics of collective cell migration. *PNAS* **108,** 4714–4719 (2011).
13.   Borghi, Lowndes, Maruthamuthu, Gardel & Nelson. Regulation of cell motile behavior by crosstalk between cadherin- and integrin-mediated adhesions. *Proc. Natl. Acad. Sci. U. S. A.* **107,** 13324–9 (2010).
14.   Vicsek & Zafeiris. Collective motion. *Phys. Rep.* **517,** 71–140 (2012).
15.   Cavagna & Giardina. The seventh starling. *Significance* 62–66 (2008).

Chapter 2 References

1. Yamada T, Hayamizu Y, Yamamoto Y, et al. (2011) A stretchable carbon nanotube strain sensor for human-motion detection. Nature Nanotechnology 1–11. doi: 10.1038/nnano.2011.36
2. Ajovalasit a, Zuccarello B (2005) Local Reinforcement Effect of a Strain Gauge Installation on Low Modulus Materials. The Journal of Strain Analysis for Engineering Design 40:643–653. doi: 10.1243/030932405X30894
3. Rogers J a, Someya T, Huang Y (2010) Materials and mechanics for stretchable electronics. Science (New York, NY) 327:1603–7. doi: 10.1126/science.1182383

4. Carta R, Jourand P, Hermans B, et al. (2009) Design and implementation of advanced systems in a flexible-stretchable technology for biomedical applications. Sensors and Actuators A: Physical 156:79–87. doi: 10.1016/j.sna.2009.03.012

5. Cutkosky MR, Kim S (2009) Design and fabrication of multi-material structures for bioinspired robots. Philosophical transactions Series A, Mathematical, physical, and engineering sciences 367:1799–813. doi: 10.1098/rsta.2009.0013

6. Lacour SP, Benmerah S, Tarte E, et al. (2010) Flexible and stretchable micro-electrodes for in vitro and in vivo neural interfaces. Medical & biological engineering & computing 945–954. doi: 10.1007/s11517-010-0644-8

7. Sekitani T, Nakajima H, Maeda H, et al. (2009) Stretchable active-matrix organic light-emitting diode display using printable elastic conductors. Nature materials 8:494–9. doi: 10.1038/nmat2459

8. Takei K, Takahashi T, Ho JC, et al. (2010) Nanowire active-matrix circuitry for low-voltage macroscale artificial skin. Nature Materials 9:1–6. doi: 10.1038/nmat2835

9. Lee K, Lee SS, Lee J a, et al. (2010) Carbon nanotube film piezoresistors embedded in polymer membranes. Applied Physics Letters 96:013511. doi: 10.1063/1.3272686

10. Kyrylyuk A V., Hermant MC, Schilling T, et al. (2011) Controlling electrical percolation in multicomponent carbon nanotube dispersions. Nature Nanotechnology. doi: 10.1038/nnano.2011.40

11. Hu L, Hecht DS, Gruner G (2004) Percolation in Transparent and Conducting Carbon Nanotube Networks. Nano Letters 4:2513–2517.

12. Adrega T, Lacour SP (2010) Stretchable gold conductors embedded in PDMS and patterned by photolithography: fabrication and electromechanical characterization. Journal of Micromechanics and Microengineering 20:055025. doi: 10.1088/0960-1317/20/5/055025

13. Spitalsky Z, Tasis D, Papagelis K, Galiotis C (2010) Carbon nanotube–polymer composites: Chemistry, processing, mechanical and electrical properties. Progress in Polymer Science 35:357–401. doi: 10.1016/j.progpolymsci.2009.09.003

14. Tiwari MK, Yarin AL, Megaridis CM (2008) Electrospun fibrous nanocomposites as permeable, flexible strain sensors. Journal of Applied Physics 103:044305. doi: 10.1063/1.2885112

15. Graz IM, Cotton DPJ, Lacour SP (2009) Extended cyclic uniaxial loading of stretchable gold thin-films on elastomeric substrates. Applied Physics Letters 94:071902. doi: 10.1063/1.3076103

16. Jha V, Thomas AG, Bennett M, Busfield JJC (2010) Reversible Electrical Behavior with Strain for a Carbon Black-Filled Rubber. Polymer 116:541–546. doi: 10.1002/app

17. Cheng C, Xiao L, Cheung Y, et al. (2007) A strain gauge that uses carbon black and carbon nanotube doped silicone oil encapsulated in a PDMS microchannel. 2007 7th IEEE Conference on Nanotechnology (IEEE NANO) 1199–1202. doi: 10.1109/NANO.2007.4601398

18. Lewandowski M, Koncar V (2010) A Flexible Strain Sensor Based on a Conductive Polymer. Sensors (Peterborough, NH) 8291–8303. doi: 10.3390/s100908291

19. Byrne MT, Gun'ko YK (2010) Recent advances in research on carbon nanotube-polymer composites. Advanced materials (Deerfield Beach, Fla) 22:1672–88. doi: 10.1002/adma.200901545

20. Hu L, Hecht DS, Grüner G (2009) A method of fabricating highly transparent and conductive interpenetrated carbon nanotube-parylene networks. Nanotechnology 20:465304. doi: 10.1088/0957-4484/20/46/465304
21. Zhang M, Fang S, Zakhidov A a, et al. (2005) Strong, transparent, multifunctional, carbon nanotube sheets. Science (New York, NY) 309:1215–9. doi: 10.1126/science.1115311
22. Shin MK, Oh J, Lima M, et al. (2010) Elastomeric Conductive Composites Based on Carbon Nanotube Forests. Advanced materials 22:2663–2667. doi: 10.1002/adma.200904270
23. Sekitani T, Nakajima H, Maeda H, et al. (2009) Stretchable active-matrix organic light-emitting diode display using printable elastic conductors. Nature materials 8:494–9. doi: 10.1038/nmat2459
24. Liu C, Choi J (2010) Strain-Dependent Resistance of PDMS and Carbon. IEEE Transactions on Microwave Theory and Techniques 9:590–595.
25. Lü Q, Cao H, Song X, et al. (2010) Improved electrical resistance-pressure strain sensitivity of carbon nanotube network/polydimethylsiloxane composite using filtration and transfer process. Chinese Science Bulletin 55:326–330. doi: 10.1007/s11434-009-0562-z
26. Huang YY, Terentjev EM (2010) Tailoring the Electrical Properties of Carbon Nanotube-Polymer Composites. Advanced Functional Materials 20:4062–4068. doi: 10.1002/adfm.201000861
27. Bokobza L (2007) Multiwall carbon nanotube elastomeric composites: A review. Polymer 48:4907–4920. doi: 10.1016/j.polymer.2007.06.046
28. Jung YJ, Kar S, Talapatra S, et al. (2006) Aligned carbon nanotube-polymer hybrid architectures for diverse flexible electronic applications. Nano letters 6:413–8. doi: 10.1021/nl052238x
29. Zhou Y, Hu L, Grüner G (2006) A method of printing carbon nanotube thin films. Applied Physics Letters 22–24. doi: 10.1063/1.2187945
30. Hu L, Yuan W, Brochu P, et al. (2009) Highly stretchable, conductive, and transparent nanotube thin films. Applied Physics Letters 94:161108. doi: 10.1063/1.3114463
31. Zhang D, Ryu K, Liu X, et al. (2006) Transparent, conductive, and flexible carbon nanotube films and their application in organic light-emitting diodes. Nano letters 6:1880–6. doi: 10.1021/nl0608543
32. Loh KJ, Kim J, Lynch JP, et al. (2007) Multifunctional layer-by-layer carbon nanotube–polyelectrolyte thin films for strain and corrosion sensing. Smart Materials and Structures 16:429–438. doi: 10.1088/0964-1726/16/2/022
33. Bennett RD, Hart AJ, Miller AC, et al. (2006) Creating Patterned Carbon Nanotube Catalysts through the Microcontact Printing of Block Copolymer Micellar Thin Films. Society 8273–8276.
34. Lipomi DJ, Vosgueritchian M, Tee BC-K, et al. (2011) Skin-like pressure and strain sensors based on transparent elastic films of carbon nanotubes. Nature nanotechnology 1–6. doi: 10.1038/nnano.2011.184
35. Sangwan VK, Southard A, Moore TL, et al. Transfer Printing Approach to All-Carbon Nanoelectronics. 1–17.
36. Wu Z, Chen Z, Du X, et al. (2011) Transparent , Conductive Carbon Nanotube Films. doi: 10.1126/science.1101243

37. Loh KJ, Lynch JP, Shim BS, Kotov N a. (2007) Tailoring Piezoresistive Sensitivity of Multilayer Carbon Nanotube Composite Strain Sensors. Journal of Intelligent Material Systems and Structures 19:747–764. doi: 10.1177/1045389X07079872

38. Cohen DJ, Mitra D, Peterson K, Maharbiz MM (2012) A highly elastic, capacitive strain gauge based on percolating nanotube networks. Nano letters 12:1821–5. doi: 10.1021/nl204052z

39. Pint CL, Xu KY, Moghazy S, et al. (2010) Dry Contact Transfer Printing of Aligned Carbon Nanotube Patterns and. 4:1131–1145.

40. Kim B-S, Lee SW, Yoon H, et al. (2010) Pattern Transfer Printing of Multiwalled Carbon Nanotube Multilayers and Application in Biosensors. Chemistry of Materials 22:4791–4797. doi: 10.1021/cm101401t

41. Saran N, Parikh K, Suh D-S, et al. (2004) Fabrication and characterization of thin films of single-walled carbon nanotube bundles on flexible plastic substrates. Journal of the American Chemical Society 126:4462–3. doi: 10.1021/ja037273p

42. Li S, Yan Y, Liu N, et al. (2007) Transfer printing of submicrometer patterns of aligned carbon nanotubes onto functionalized electrodes. Small (Weinheim an der Bergstrasse, Germany) 3:616–21. doi: 10.1002/smll.200600525

43. Palmer HB (1937) No Title. Transactions of the American Institute of Electrical Engineers 56:363–366.

Chapter 3 References

1. Bonner JT (2000) First Signals: The Evolution of Multicellular Development. Princeton: Princeton University Press.

2. Zicha D, Dunne GA, Brown AF (1991) A new direct-viewing chemotaxis chamber. Journal of Cell Biology 99: 769-775.

3. Engelmann TW (1881) Neue Methode zur Untersuchung der Sauerstoffausscheidung pfanzlicher and tierischer Organismen. Pfluegers Arch Gesamte Physiol Menschen Tiere 25: 285-292.

4. Boyden S (1962) The chemotactic effect of mixtures of antibody and antigen on polymorphonuclear leucocytes. Journal of Experimental Medicine: 453-466.

5. Park JH, Bansal T, Pinelis M, Maharbiz MM (2006) Electrolytic patterning of dissolved oxygen microgradients during cell culture," Lab on a Chip 6: 611-622.

6. Jeon LN, Baskaran H, Dertinger S, Whitesides G, Water LVd, et al. (2002) Neutrophil chemotaxis in linear and complex gradients of interleukin-8 formed in a microfabricated device. Nature: Biotechnology 20: 826-830.

7. Ismagilov RF, Maharbiz MM (2007) Can we build synthetic, multicellular systems by controlling developmental signaling in space and time? Current Opinions in Chemical Biology 11: 604-611

8. Keenan TM, Folch A (2008) Biomolecular gradients in cell culture systems. Lab on a Chip 8: 34-57.

9. Chena D, Dua W, Liua Y, Liua W, Kuznetsovb A, et al. (2008) The chemistrode: A droplet-based microfluidic device for stimulation and recording with high temporal, spatial, and chemical resolutio. PNAS 105: 16843-16848

10. Bansal T, Lenhart J, Kim T, Duan C, Maharbiz MM (2009) Patterned delivery and expression of gene constructs into developing zebrafish embryos using microfabricated interfaces. IEEE Biomedical Microdevices 11.

11. Mayer G, Heckel A (2006) Biologically active molecules with a "light switch". Angew Chem, Int Ed 45: 4900-4921.
12. Shestopalov I, Chen J (2008) Chemial technologies for probing embryonic development. Chemical Society Review 37: 1294-1307.
13. Chambers JJ, Banghart MR, Trauner D, Kramer RH (2006) Light-Induced Depolarization of Neurons Using a Modified Shaker K+ Channel and a Molecular Photoswitch. J Neurophysiol 96: 2792-2796.
14. Ellis-Davies GC (2007) Caged compounds: photorelease technology for control of cellular chemistry and physiology. Nature: Methods 4: 619-628.
15. Basu S, Gerchman Y, Collins C, Arnold F, Weiss R (2005) A synthetic multicellular system for programmed pattern formation. Nature 434: 1130-1134.
16. Brown T, Chang C, Heinze B, Hollinger P, Kittleson J, et al. (2007) Development of an inducible three colour bacterial water colour system. IET: Synthetic Biology 1: 21-24
17. Gurtner G, Werner S, Barrandon Y, Longaker M (2008) Wound repair and regeneration. Nature 453: 314-321.
18. Lutolf M, Hubbell J (2005) Synthetic biomaterials as instructive extracellular microenvironments for morphogenesis in tissue engineering. Nature: Biotechnology 23: 47-55.
19. Gu W, Zhu X, Futai N, Cho BS, Takayama S (2004) Computerized microfluidic cell culture using elastomeric channels and Braille displays. PNAS 101: 15861-15866.
20. Peterman MC, Noolandi J, Blumenkranz MS, Fishman HA (2004) Localized chemical release from an artificial synapse chip. PNAS 101: 9951-9954.
21. Merrin J, Leibler S, Chuang J (2007) Printing Multistrain Bacterial Patterns with a Piezoelectric Inkjet Printer. PLoS One 2.
22. Boland T, Xu T, Damon B, Manley B, Kesari P, et al. (2007) Drop-on-demand printing of cells and materials for designer tissue constructs. Materials Science & Engineering 27: 372-376.
23. Saunders RE, Gough JE, Derby B (2008) Delivery of human fibroblast cells by piezoelectric drop-on-demand inkjet printing. Biomaterials 29: 193-203.
24. Roth EA, Xu T, Das M, Gregory C, Hickman JJ, et al. (2004) Inkjet printing for high-throughput cell patterning. Biomaterials 25: 3707-3715.
25. Boland T, Xu T, Damon B, Cui X (2006) Appication of inkjet prining to tissue engineering. Biotechnolog Journal 1: 910-917.
26. Cohen DL, Malone E, Lipson H, Bonassar LJ (2006) Direct freeform fabrication of seeded hydrogels in arbitrary geometries. Tissue Engineering.
27. Rosoff WJ, McAllister R, Esrick MA (2005) Generating controlled molecular gradients in 3D gels. Biotechnol Bioeng.
28. Ilkhanizadeh S, Teixeira AI, Hermanson O (2007) Inkjet printing of macromolecules on hydrogels to steer neural stem cell differentiation. Biomaterials 28: 3936-3943.
29. Campbell PG, Miller ED, Fisher GW, Walker LM, Weiss LE (2005) Engineered spatial patterns of FGF-2 immobilized on fibrin direct cell organization. Biomaterials 26: 6762-6770.
30. Saadi W, Rhee SW, Lin F, Vahidi B (2007) Generation of stable concentration gradients in 2D and 3D environments using a microfluidic ladder chamber. Biomedical Microdevices.
31. Lausted C, Dahl T, Warren C, King K, Smith K, et al. (2004) POSaM: a fast, flexible, open-source, inkjet oligonucleotide synthesizer and microarrayer. Genome Biology 5: R58-R58.

32. Madou M, Madou M, Zoval J, Zoval J, Jia G, et al. LAB ON A CD. Annu Rev Biomed Eng
    8: 601-628
33. Ducree J, Haeberle S, Lutz S, Pausch S, Stetten Fv, et al. The centrifugal microfluidic Bio-Disk platform.
34. Yildirim N, Mackey MC (2003) Feedback Regulation in the Lactose Operon: A Mathematical Modeling Study and Comparison with Experimental Data. Biophysical Journal 84: 2841-2851.
35. Ozbudak EM, Thattai M, Lim HN, Shraiman BI, van Oudenaarden A (2004) Multistability in the lactose utilization network of Escherichia coli. Nature 427: 737-740.
36. Ahmadzadeh A, Halasz A, Kumar V, Prajna S, Jadbabaie A. Analysis of the Lactose metabolism in E. coli using sum-of-squares decomposition; 2005. pp. 879-884.
37. Murray JD (1993) Mathematical Biology: II: Spatial Models and Biomedical Applications. Berlin-Heidelberg: Springer-Verlag
38. Wong P, Gladney S Mathematical Model of the lac Operon: Inducer Exclusion, Catabolite Repression, and Diauxic Growth on Glucose and Lactose. 132-114 p.
39. Lehninger AL, Nelson DL, Cox MM (2004) Principles of Biochemistry.
40. Dunlop MJ, Cox RS, Levine JH, Murray RM, Elowitz MB (2008) Regulatory activity revealed by dynamic correlations in gene expression noise. Nature: Genetics 40.
41. Fujikawa H, Morozumi S (2005) Modeling Surface Growth of Escherichia coli on Agar Plates. Applied Environmental Microbiology 17: 7920-7926.
42. Amonlirdviman K, Khare NA, Tree DRP, Chen W-S, Axelrod JD, et al. (2005) Mathematical Modeling of Planar Cell Polarity to Understand Domineering Nonautonomy. Science 307: 423-426.
43. Wolpert L (1969) Positional information and the spatial pattern of cellular differentiation. Journal of Theoretical Biology 25: 1-47.

Chapter 4 References

1. Vicsek & Zafeiris. Collective motion. *Phys. Rep.* **517,** 71–140 (2012).
2. Zitterbart, Wienecke, Butler & Fabry. Coordinated movements prevent jamming in an Emperor penguin huddle. *PLoS One* **6,** e20260 (2011).
3. Cavagna, Cimarelli, Giardina, Parisi, Santagati, Stefanini & Viale. Scale-free correlations in starling flocks. *Proceedings* **107,** 11865–70 (2010).
4. Gordon. The rewards of restraint in the collective regulation of foraging by harvester ant colonies. *Nature* 3–6 (2013). doi:10.1038/nature12137
5. Zheng, Ahn, Chen & Laval. Freeway Traffic Oscillations: Microscopic Analysis of Formations and Propagations using Wavelet Transform. *Procedia - Soc. Behav. Sci.* **17,** 702–716 (2011).
6. Trepat, Wasserman, Angelini, Millet, Weitz, Butler & Fredberg. Physical forces during collective cell migration. *Nat. Phys.* **5,** 426–430 (2009).
7. Angelini, Hannezo, Trepat, Marquez, Fredberg & Weitz. Glass-like dynamics of collective cell migration. *PNAS* **108,** 4714–4719 (2011).

8. Tambe, Hardin, Angelini, Rajendran, Park, Serra-Picamal, Zhou, Zaman, Butler, Weitz, Fredberg & Trepat. Collective cell guidance by cooperative intercellular forces. *Nat. Mater.* **10,** 469–75 (2011).

9. Kim, Serra-Picamal, Tambe, Zhou, Park, Sadati, Park, Krishnan, Gweon, Millet, Butler, Trepat & Fredberg. Propulsion and navigation within the advancing monolayer sheet. *Nat. Mater.* **12,** 1–8 (2013).

10. Poujade, Hertzog, Jouanneau, Chavrier, Ladoux & Buguin. Collective migration of an epithelial monolayer. *October* (2007).

11. Ram, Vedula, Chun, Lei, Hersen & Kabla. Emerging modes of collective cell migration induced by geometrical constraints. (2012). doi:10.1073/pnas.1119313109

12. Anon, Serra-Picamal, Hersen, Gauthier, Sheetz, Trepat & Ladoux. Cell crawling mediates collective cell migration to close undamaged epithelial gaps. *Proc. Natl. Acad. Sci.* (2012). doi:10.1073/pnas.1117814109

13. Serra-Picamal, Conte, Vincent, Anon, Tambe, Bazellieres, Butler, Fredberg & Trepat. Mechanical waves during tissue expansion. *Nat. Phys.* **8,** 628–634 (2012).

14. Petitjean, Reffay, Grasland-Mongrain, Poujade, Ladoux, Buguin & Silberzan. Velocity fields in a collectively migrating epithelium. *Biophys. J.* **98,** 1790–800 (2010).

15. Bialek, Cavagna, Giardina, Mora, Silvestri, Viale & Walczak. Statistical mechanics for natural flocks of birds. *Proc. Natl. Acad. Sci. U. S. A.* **109,** 4786–91 (2012).

16. Sun, Huang, Yang, Liu, Xie, Yuan, Zhang & Jiang. Self-organizing circuit assembly through spatiotemporally coordinated neuronal migration within geometric constraints. *PLoS One* **6,** e28156 (2011).

17. Friedl, Hegerfeldt & Tusch. Collective cell migration in morphogenesis and cancer. *Int. J. Dev. Biol.* **48,** 441–9 (2004).

18. Friedl & Gilmour. Collective cell migration in morphogenesis, regeneration and cancer. *Nat. Rev. Mol. Cell Biol.* **10,** 445–57 (2009).

19. Vasilyev, Liu, Mudumana, Mangos, Lam, Majumdar, Zhao, Poon, Kondrychyn, Korzh & Drummond. Collective cell migration drives morphogenesis of the kidney nephron. *PLoS Biol.* **7,** e9 (2009).

20. Bianco, Poukkula, Cliffe, Mathieu, Luque, Fulga & Rørth. Two distinct modes of guidance signalling during collective migration of border cells. *Nature* **448,** 362–5 (2007).

21. Selmeczi. Phase transition in the collective migration of tissue cells: Experiment and model. 1–5 (2006). doi:10.1103/PhysRevE.74.061908

22. Mccann, Kriebel, Parent & Losert. Cell speed , persistence and information transmission during signal relay and collective migration. 1724–1731 (2010). doi:10.1242/jcs.060137

23. Vitorino & Meyer. Modular control of endothelial sheet migration. **1,** 3268–3281 (2008).

24. McCaig, Song & Rajnicek. Electrical dimensions in cell science. *J. Cell Sci.* **122,** 4267–76 (2009).

25. Forrester, Lois, Zhao & McCaig. The spark of life: the role of electric fields in regulating cell behaviour using the eye as a model system. *Ophthalmic Res.* **39,** 4–16 (2007).

26. Zhao. Electrical fields in wound healing-An overriding signal that directs cell migration. *Semin. Cell Dev. Biol.* **20,** 674–82 (2009).

27. Caig, Rajnicek, Song & Zhao. Controlling Cell Behavior Electrically : Current Views and Future Potential. *Physiol. Rev.* 943–978 (2005). doi:10.1152/physrev.00020.2004.

28. Nagel. Uber Galvanotaxis. *Pflügers Arch. Bd* **59,** (1895).

29. Allen, Mogilner & Theriot. Electrophoresis of Cellular Membrane Components Creates the Directional Cue Guiding Keratocyte Galvanotaxis. *Curr. Biol.* 1–9 (2013). doi:10.1016/j.cub.2013.02.047

30. Sun, Do, Gao, Zhao, Zhao & Mogilner. Keratocyte Fragments and Cells Utilize Competing Pathways to Move in Opposite Directions in an Electric Field. *Curr. Biol.* 1–6 (2013). doi:10.1016/j.cub.2013.02.026

31. Zhao, Song, Pu, Wada, Reid, Tai, Wang, Guo, Walczysko, Gu, Sasaki, Suzuki, Forrester, Bourne, Devreotes, McCaig & Penninger. Electrical signals control wound healing through phosphatidylinositol-3-OH kinase-gamma and PTEN. *Nature* **442,** 457–60 (2006).

32. Li, Hartley, Reiss, Sun, Pu, Wu, Lin, Hoang, Yamada, Jiang & Zhao. E-cadherin plays an essential role in collective directional migration of large epithelial sheets. *Cell. Mol. Life Sci.* (2012). doi:10.1007/s00018-012-0951-3

33. Martinsen & Grimnes. *Bioimpedance and Bioelectricity Basics*. (Academic Press, 2011).

34. Shelley. *Frankenstein; or, The Modern Prometheus*. (Lackington, Hughes, Harding, Mavor & Jones, 1831).

35. Lightman. *The Discoveries*. (Random House LLC, 2010).

36. Elliott. "More Subtle than the Electric Aura": Georgian Medical Electricity, the Spirit of Animation and the Development of Erasmus Darwin's Psychophysiology. *Med. Hist.* **52,** 195–220 (2012).

37. Matteucci. The Physical Phenomenon of Living Bodies. *Lancet* **1254,** (1847).

38. Dierig. *Wissenschaft in der Maschinenstadt*. (Wallstein, 2006).

39. Cooper & Keller. Perpendicular orientation and directional migration of amphibian neural crest cells in dc electrical fields. *Proc. Natl. Acad. Sci. U. S. A.* **81,** 160–4 (1984).

40. Robinson. The responses of cells to electrical fields: a review. *J. Cell Biol.* **101,** 2023–7 (1985).

41. Erickson & Nuccitelli. Can Be Influenced by Physiological Electric Fields Embryonic Fibroblast Motility and Orientation. **98,** (1984).

42. Nishimura, Isseroff & Nuccitelli. Human keratinocytes migrate to the negative pole in direct current electric fields comparable to those measured in mammalian wounds. *J. Cell Sci.* **109 (Pt 1,** 199–207 (1996).

43. Song, Gu, Pu, Reid, Zhao & Zhao. Application of direct current electric fields to cells and tissues in vitro and modulation of wound electric field in vivo. *Nat. Protoc.* **2,** 1479–89 (2007).

44. Huang, Cheng, Yen & Young. Electrotaxis of lung cancer cells in a multiple-electric-field chip. *Biosens. Bioelectron.* **24,** 3510–6 (2009).

45. Tsai, Peng, Wu, Chang & Cheng. Electrotaxis of oral squamous cell carcinoma cells in a multiple-electric-field chip with uniform flow field. *Biomicrofluidics* **6,** 034116 (2012).

46. Song, Han, Ko, Kim & Shin. Collaborative effects of electric field and fluid shear stress on fibroblast migration. *Lab Chip* (2013). doi:10.1039/c3lc41240g

47. Deforet, Parrini, Petitjean, Biondini, Buguin, Camonis & Silberzan. Automated velocity mapping of migrating cell populations (AVeMap). *Nat. Methods* **9,** 1081–3 (2012).

48. Pust. PIV: Direct Cross-Correlation compared with FFT-based Cross-Correlation. *Proc. 10th Int. Symp. Appl. Laser Tech. to Fluid Mech.* **27,** (2000).

49. Cabral & Leedom. Imaging vector fields using line integral convolution. in *Proc. 20th Annu. Conf. Comput. Graph. Interact. Tech.* (ACM, 1993).

50. Cavagna, Cimarelli, Giardina & Parisi. Scale-free correlations in bird flocks.

51. Khalil & Friedl. Determinants of leader cells in collective cell migration. *Integr. Biol. (Camb).* **2,** 568–74 (2010).

52. Abercrombie. Contact inhibition in tissue culture. *In Vitro* **6,** 128–42 (1970).

53. Puliafito, Hufnagel, Neveu, Streichan, Sigal, Fygenson & Shraiman. Collective and single cell behavior in epithelial contact inhibition. *Proc. Natl. Acad. Sci. U. S. A.* **109,** 739–44 (2012).

Appendix A: Supplemental material for operon modeling and inkjet preparation

Simulation parameters

	Net production		Degradation		Diffusion
$\dfrac{dM}{dt}$	$\eta \cdot \alpha_M f_1(A) + \Gamma_0$	+	$-\tilde{\gamma}_M\, M$	+	--
$\dfrac{dA}{dt}$	$B \cdot \left[\alpha_A g_1(L) - \beta_A f_2(A)\right]$	+	$-\tilde{\gamma}_A\, A$	+	--
$\dfrac{dL_{\text{int}}}{dt}$	$P \cdot \left[\alpha_L \cdot h(L_{ext}) - \beta_L \cdot g_2(L_{\text{int}})\right] - \alpha_A \cdot B \cdot g_1(L_{\text{int}})$	+	$-\tilde{\gamma}_L\, L_{\text{int}}$	+	--
$\dfrac{dL_{ext}}{dt}$	$-P \cdot \left[\alpha_L \cdot h(L_{ext}) + \beta_L \cdot g_2(L_{\text{int}})\right]$	+	--	+	$D_{L_{ext}} \nabla^2 L_{ext}$
$\dfrac{dG_{ext}}{dt}$	$-k_{t\_Glu} \cdot \dfrac{G_{ext}}{G_{ext} + K_{t\_Glu}}$	+	--	+	$D_{G_{ext}} \nabla^2 G_{ext}$
$\dfrac{dcAMP}{dt}$	$k_{cAMP} \cdot \left(\dfrac{K_{c,cAMP}}{G_{ext} + K_{c,cAMP}}\right)$	+	γ_{cAMP}	+	--
$\dfrac{dXgalB}{dt}$	$\dfrac{B}{1 + e^{-(2\cdot10^7 \cdot M)}} \cdot \alpha_A$	+	--	+	--

$$f_1(A) = \frac{1 + K_1 A^2}{K + K_1 A^2}$$

$$f_2(A) = \frac{A}{K_A + K}$$

$$\tilde{\gamma}_M = (\gamma_M + \mu)$$

$$\tilde{\gamma}_A = (\gamma_A + \mu)$$

$$\tilde{\gamma}_L = (\gamma_L + \mu)$$

$$g_1(L) = \frac{L}{L + K_L}$$

$$g_2(L) = \frac{L}{K_{L1} + L}$$

$$\eta = \eta_0 \cdot \frac{cAMP}{K_{fit} + cAMP}$$

$$h(L_{ext}) = \frac{L_{ext}}{L_{ext} + K_{L_{ext}}}$$

$$\gamma_{cAMP} = -(scAMP + \mu) \cdot cAMP$$

$$P = k_P M$$

$$B = k_B M$$

Table S1: Equations used in the simulation

Type	Symbol	Description	Value	Unit
Variables				
	M	mRNA concentration	-	M
	A	allolactose concentration	-	M
	L_{int}	intracellular lactose concentration	-	M
	L_{ext}	extracellular lactose concentration	-	M
	G_{ext}	extracellular glucose concentration	-	M
	cAMP	intracellular cAMP concentration	-	M
	XgalB	X-gal Blue product concentration	-	M
	B	β - galactosidase concentration	-	M
	P	lactose permease concentration	-	M
Constants				
Diffusion	$D_{L_{ext}}$	External lactose	1×10^{-10}	$m^2 s^{-1}$
	$D_{G_{ext}}$	External glucose	2×10^{-10}	$m^2 s^{-1}$
	D_{XgalB}	X-Gal	0.85×10^{-10}	$m^2 s^{-1}$
Loss	γ_M	mRNA degradation	0.411/60	s^{-1}
	μ	Loss due to dilution	0.0226/60	s^{-1}
	γ_A	Allolactose degradation	0.52/60	s^{-1}
	γ_L	Lactose degradation	0	s^{-1}
	γ_P	Permease degradation	0.65/60	s^{-1}
	γ_B	β – galactosidase degradation	8.33e-4/60	s^{-1}
Equilibirum	K_1	Repressor-allolactose reaction	2.52×10^{-2}	$(\mu \cdot M)^{-2}$
	K	Loss rate of allolactose via conversion to glucose and galactose	7.2×10^3	--
	K_A	Allolactose to glucose and galactose	1.95	mol/m^3
Saturation	K_{L1}	Internal lactose (L_{int}) loss due to permease reversability	1.81	mol/m^3
	K_{Lext}	Lactose permease import constant	0.26	mM
	K_L	Conversion of lactose to allolactose	0.97×10^{-3}	$10^3 \cdot mol/m^3$
	K_{t_Glu}	Saturation of glucose transport	15×10^{-6}	$10^3 \cdot mol/m^3$
	K_{fit}	Fitted saturation constant for η parameter	5×10^{-8}	$10^3 \cdot mol/m^3$
Time				
	τ_B	β – gal. production via mRNA translation	2*60[s]	s
	τ_M	mRNA transcription from DNA	€0.1*60[s]	s

	τ_P	Permease production via mRNA translation	0.83*60[s]	s
Rate				
	k_B	Relates β – gal. production to mRNA concentration.	0.677	--
	k_P	Relates permease production to mRNA concentration	13.94	--
	α_L	Inversely proportional to L_{ext}	(2.88 x10^3)/60	s^{-1}
	α_M	Production rate of mRNA from DNA transcription	9.97 x 10^{-7}	$\dfrac{10^3 \cdot mol}{m^3 \cdot 60 \cdot s}$
	α_A	Production rate of Allolactose from lactose mediated by β – galactosidase	$\dfrac{1.76 \cdot 10^4}{60}$	s^{-1}
	α_B	Production rate of β – galactosidase through mRNA transcription	(1.66 x10^{-2})/60	s^{-1}
	α_P	Production rate of Permease	10/60	s^{-1}
	β_A	Loss rate of Allolactose via conversion to glucose and galactose	(2.15 x10^4)/60	s^{-1}
	β_L	Intracellular lactose loss to the extracellular fluid because of reversible nature of the permease-mediated transport	44.166	s^{-1}
	Γ_0	Spontaneous rate of mRNA production due to a repressor not bound	7.25 x10^{-10}	$\dfrac{10^3 \cdot mol}{m^3 \cdot 60 \cdot s}$
	k_{t_glu}	Glucose transport constant	3000	$\dfrac{10^3 \cdot mol}{m^3 \cdot 60 \cdot s}$
	k_{cAMP}	cAMP sythesis rate constant	1 x10^{-3}	$\dfrac{10^3 \cdot mol}{m^3 \cdot 60 \cdot s}$
	K_{cAMP}	Inhibition constant for cAMP production	4 x10^{-5}	$\dfrac{10^3 \cdot mol}{m^3 \cdot 60 \cdot s}$
	scAMP	Composite cAMP excretion and degradation rate.	2.1/60	s^{-1}
Efficiency				
	η	Efficiency parameter for mRNA production regulated by cAMP	--	--
	η_0	Maximum value for efficiency parameter η	1	--

$$k_B \cdot M = \frac{\alpha_B \cdot e^{-\mu \tau_B}}{\tilde{\gamma}_B} \cdot M = B \qquad\qquad k_P \cdot M = \frac{\alpha_P \cdot e^{-\mu(\tau_B + \tau_P)}}{\tilde{\gamma}_P} \cdot M = P$$

Table S2: Simulation parameters

Development of the model and simulation

The model for the lactose feedback (Table S1, Eqns. 1 – 4) on the *lac* operon is based on [27] with order reduction shown in [30] and with the introduction of separate variables for internal (L_{int}) lactose which does not diffuse from cell to cell and external lactose (L_{ext}) which is allowed to diffuse. The effect of glucose (Table S1, Eqns. 5 -7) is modeled after [28]. Glucose acts by altering the concentrations of cAMP and, in turn, the concentration of the cAMP:CRP complex (see [28] Eqn 5 and *Appendix* 1) whose presence enhances transcription initiation when it is bound near the *lac* promoter. This is modeled as an efficiency factor, η, which can have a value from 0 to 1. In order to determine the fraction of total binding sites occupied by the cAMP-CRP complex, a mass balance is required ([28]):

(1) [CRP] = [CRP$_f$] + [CRP:E] + [CRP:cAMP] + [CRP:D] + [CRP:cAMP:E] + [CRP:cAMP:D]
(2) [cAMP] = [cAMP$_f$] + [CRP:cAMP] + [CRP:cAMP:E] + [CRP:cAMP:D]
(3) [E] = [E$_f$] + [CRP:E] + [CRP:cAMP:E]
    where
        [CRP:cAMP] = K_{ns}[CRP$_f$][cAMP$_f$]
        [CRP:E] = K_{np}[CRP$_f$][E$_f$]
        [CRP:D] = K_{nd}[CRP$_f$][D]
        [CRP:cAMP:E] = K_{nsp}[CRP:cAMP][E$_f$]
        [CRP:cAMP:D] = K_{nsd}[CRP:cAMP][D$_f$]
    here
        the subscript *f* denotes the concentration of free compound
        [D] is the concentration of nonspecific DNA binding sites (0.0118 M)
        [E] is the CRP:cAMP DNA binding site concentration (8.47×10^{-12} mol/ g
            DCW)
        [CRP] is the cAMP receptor protein concentration (2×10^{-6} M)
        K_{np} 10^6 1/M
        K_{nd} 10^6 1/M
        K_{ns} 2×10^9 1/M
        K_{nsp} 1×10^9 1/M
        K_{nsd} 1×10^5 1/M

If one assumes 50% of the non-specific DNA binding sites are unoccupied ($D_f = D/2$), then this is a system of three equations and three variables (E_f, cAMP, CRP$_f$). From the values of these three variables, we can calculate the efficiency factor, [28, Eq. 5]

$$(4) \quad \eta = \frac{[CRP:cAMP:E]}{[E]}$$

To avoid having to solve these equations at every time step, we noted that a plot of cAMP vs. η follows a typical saturation curve (Figure S1):

$$(5) \quad \eta = \frac{cAMP}{K_{fit} + cAMP}$$

Thus, we can calculate the efficiency as a function of cAMP using the fit equation above at a given time-step within the FEM solver (see below). Moreover, note that smaller values of K_{fit} sharpen the cAMP-dependent activation of mRNA transcription, thereby sharpening the effect of glucose on shutting off lactose metabolism. K_{fit} was one of the parameters adjusted in order to fit the lactose-glucose simulations to the data (see below).
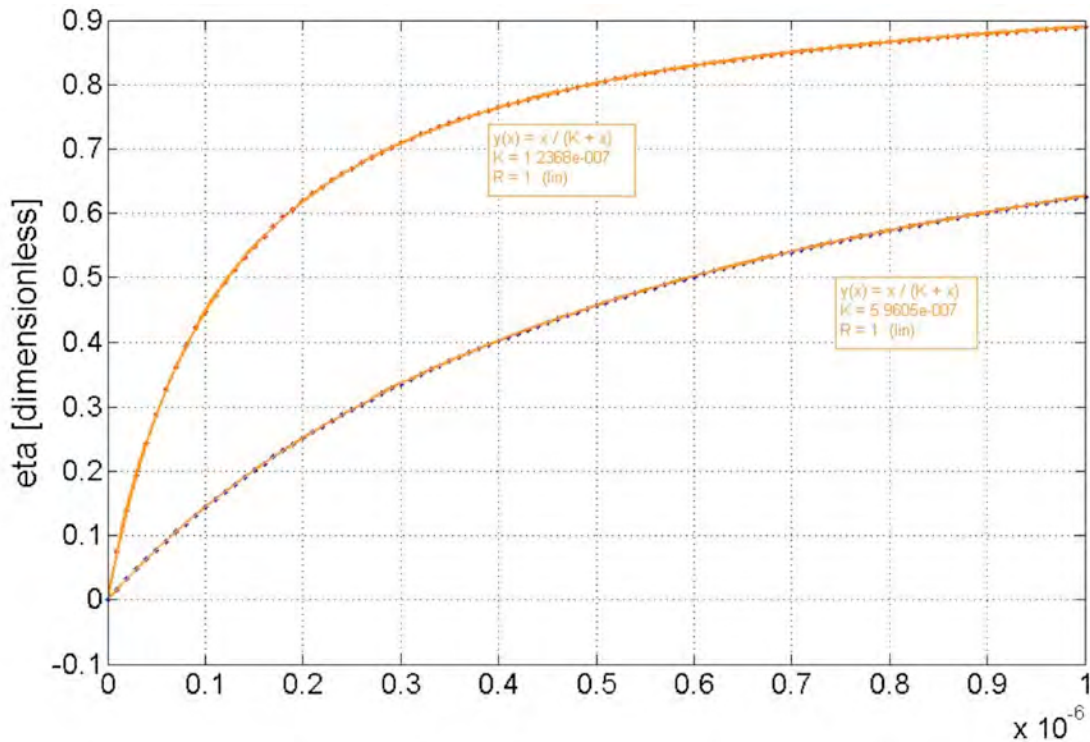

Figure S1: cAMP vs. η saturation curve
Blue dots plot η using Eqn. 4 and the analytical solution to the mass transfer equations (Eqns. 1 - 3); the orange line is the fit using Eqn. 5.

Finite Element Analysis
Finite element analysis was performed in COMSOL 3.4 using the *Stationary* and *Time Dependent Diffusion* modules. The reaction and diffusion terms in the equations shown in

Table 1 were entered into a rectangular area matching the size of the cell growth area in the experiments. Zero flux boundary conditions were used. Initial concentrations of lactose and glucose were set in the L_{ext} and G_{ext} variables, respectively. Sharp boundaries in initial concentrations were modeled using the logistic equation to avoid infinite slopes and aid convergence. When matching data to simulation, we varied diffusion rates and K_{fit} about their nominal values to obtain the best fit to all available data (i.e. the model was made to match all data sets presented in the paper). In most cases, better fits could be obtained if each data set was fit independently, which would be expected due to uncontrolled experimental variations (e.g. local temperature effects on diffusion, local cell density variations, etc.)

Validation

In addition to the fact that the model fits the experimental data fairly well, we also compared to it prior analytical models of *lac* behavior and found similar agreement. In particular, we verified the characteristic bistability of *lac,* demonstrating (Figure S2) that the bistable point occurs at an external lactose concentration of 60 μM [29, 30].
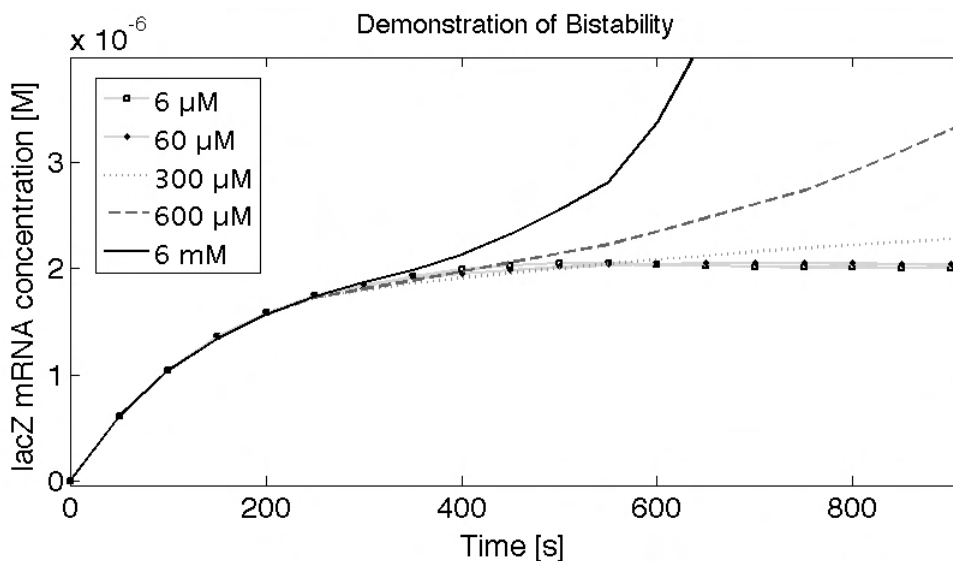

Figure S2: Demonstration of Bistability

Plot of lacZ mRNA concentration as a function of time for various external lactose (Le) doses. To generate this plot, an initial, homogenous concentration of lactose was applied over the simulated field and the resultant mRNA concentration was plotted over time (as the lactose was consumed). Our model exhibits the same bistability as those in [*,*]. Namely, the threshold concentration of external lactose (Le) required to trigger the 'ON' state of the lac operon is 60 uM. At or below this dose, the steady-state mRNA concentration is ~ 2uM. Above this those, the lac operon is strongly upregulated and the amount of mRNA produced is a function of the amount of lactose dosed. Once all lactose is consumed (around 3600 s), the mRNA levels return to the quiscent concentration of ~2 uM (not shown).

Supplementary Protocol Information

Cell-Specific Printing Protocols
Prior to an experiment, an overnight culture would be produced from the colony plate. A sterile loop was used to transfer a monoclonal colony to 5 mL containing 5% *Kanamycin*. This was incubated overnight for 12 hours. During the incubation period, LB Agar culture plates were produced. LB Agar (prepared as above) was autoclaved, cooled to 37 °C, inoculated with 5% *Kanamycin*, and poured into sterile, 100 mm x 100 mm square plates to a depth of 750 microns. The resulting plates were then wrapped with Parafilm and placed in a 4 °C refrigerator overnight.

At the beginning of each experiment, the overnight cultures were diluted with sterile LB to OD_{600} 0.8, and the plates were infiltrated with X-Gal (Sigma). An X-Gal solution was prepared by dissolving 20mg/ml in DMSO. Each plate received 200 μL of the X-Gal solution and bead-spreading was used to distribute this uniformly over the surface. Following this, the plates were allowed 10 minutes for the X-Gal to infiltrate the agar and the DMSO to evaporate. This procedure was implemented after it was noticed that shorter times resulted in X-Gal precipitation on the surface of the agar during the next step. After infiltration, 150 μL of *E. coli* were bead-spread onto the surface of each plate, and a further 10 minutes were allowed for stabilization, after which the plates were wrapped in two layers of Parafilm, and incubated at 37 °C for 3.5 hours. Two layers of Parafilm were found to be necessary owing to the angular geometry of square Petri dishes. A single layer tended to rupture too easily, resulting in non-uniform drying of the agar surfaces.

Inkjet Modification

Prior to any printing of custom inks, the printer was dissembled into its component parts, and vestigial components were removed to free-up space. This step was not strictly necessary, but it makes it simpler to sterilize the printer and manipulate samples. Specifically, the paper-feed tray, anterior-rail, anterior paper roller, top-cover, and primary paper roller were removed to allow easier access to the printing field.

The R280 was chosen for its ability to print on compact discs (CD). It does this by feeding a CD through a series of sprung, rubber rollers. These rollers apply pressure to the disc, and when they are turned the disc translates in exactly the same way that paper is normally fed through the printer. While this approach is fine for standard CDs, care must be taken to keep the rollers from coming into contact with the sample area. While it is reasonable to assume that keeping the samples below the surface of the disc will protect them from the rollers, the rollers, by virtue of being sprung, tend to pitch down into the wells as they go over them, resulting in sample contamination and deformation. To counteract this problem, 1 mm high masking tape stand-offs (see Figure 1, main text) were placed along either side of the wells and provided sufficient clearance to prevent the rollers contacting the samples.

In order to prepare the Epson R280 to print custom inks, the ink lines must first be flushed. To do this, the ink cartridges must first be removed, and flexible tubing must be connected

to each of the ink-input ports. Flushing itself is accomplished with a standard syringe pump that is attached to the tubing. The lines were cleaning by flushing 10 ml of room temperature, de-ionized water through them, followed by 10 ml of 70% ethanol. This protocol was generally sufficient, and final assessment of its success was based upon whether or not any color was apparent on white filter paper held under the head during flushing. Ultimately, this process results in there being no residual ink anywhere downstream of the ink cartridges.

Once the lines were flushed, the print-head itself needed to be primed. Proper priming of a piezo print-head implies that the reservoirs downstream of the ink cartridges are filled with the desired custom inks. Priming is achieved the same way as flushing, except now each line is filled with a specific ink. In this case, the Black and Yellow lines were selected for lactose and glucose, respectively, owing to their ease of specification in software. Solutions of 1g of lactose or glucose per 10 ml of sterile DI were prepared and syringed into the Black and Yellow lines. Again, 10 ml of fluid were flushed through each line, and care was taken to ensure that no air entered the lines (this creates blockages). The remaining lines were filled with sterile DI. It is crucial to note that the priming process must take place at a very specific moment in the printer's initiation protocol. In the case of the Epson R280, priming must be performed immediately prior to actually printing, because this is the window where the printer drivers expect that the system is fully primed and ready to print. Modifying the inks during this phase essentially tricks the system. This means the print-head must be primed while the printer is powered on and ready to print, otherwise the printer will re-initialize and flush the lines with ink.

While it is possible to clean and prime the print-head by flushing fluid through the print-head and into the printer's internal waste collection system, this is not recommended as it can overflow the waste-ink tank. Rather, it is better to perform all flushing in a manner that keeps the excess fluid from collecting in the printer. We achieved this through a combination of absorbent towels and manually repositioning the print-head during the cleaning and priming procedures. Movie S1 presents this procedure in greater detail.

The printer can be controlled through the use of its default label-making software, or through any graphics program, such as Photoshop. Here, Photoshop was used, along with a custom template file that printed over the surface of the CD. Printing requires nothing more than drawing a pattern in the desired colors and sending the file to the printer. However, care must be taken when colors are selected. All graphics programs and printers employ default color profiles. These profiles are particular dangerous when single color resolution is required. For instance, black on a CMYK printer actually consists of varying percentages of C, M, and Y. This is done to enhance the appearance of the color on a printed page, and can be disastrous for this type of experiment. To circumvent this, customized color profiles were created to uniquely address Black and Yellow. Additionally, all non-essential colors were flushed with DI. Finally, all two-chemical experiments were performed by flushing all the lines but the lactose line, printing the first stage of the pattern, and then flushing all the lines but the glucose line. While non-rigorous experiments suggest that this is unnecessary, it acts as a failsafe in case the color addressing does not perform as expected.

The fluid volume being delivered per linear centimeter can be approximated from the technical datasheets for the printer. The volume of liquid printed ranges between 1.5 – 10 pL per drop; at the 1440 linear dpi resolution we used, this corresponds to approximately 8×10^3 pL / cm. That said, a caveat to consider with all consumer inkjets is that they utilize proprietary droplet-placement algorithms that determine the droplet spacing, volume/droplet, and number of droplets/dot.

Preparation of the Custom-Dishes from Compact Disks

The R280 can natively print on the surfaces of CDs, making CD-like substrates the perfect medium for bio-printing. Rather than physically altering the spacing between the printer and the substrate to introduce standard Petri dishes (a difficult procedure), we directly machined actual compact disks, thereby requiring no complex modifications to the printer itself. Specifically, disks were placed in a milling machine and 800 micron deep wells were milled directly into the surface. The size, geometry, and position of the wells were selected so as not to interfere with the printer mechanisms (feed rollers or print-head carriage). Post-machining, the disks were cleaned of all debris and washed in ethanol—steps that were performed prior to every experiment.

Printing of chemicals onto cultured E. coli

After 3.5 hours of incubation, the bacteria plates were removed from the incubator and prepared for printing. We used sterile shim-stock to cut out individual pieces of cell-bearing agar and transfer them to the appropriate wells on the surface of the CD. The CD was then loaded into the printer and the print job sent. No run lasted longer than 2 minutes, and at no point did the cells come into contact with any components of the printer. Post-printing, the agar slices were transferred to hydrated Petri-dishes (containing sterile agar in their lids), placed in the incubator, and observed over 12 hours.

Appendix B: Galvanotaxis and chamber design

Galvanotaxis

For a full discussion of the most likely mechanism and a thorough investigation of relevant parameters, please consult Allen et al. (2013). Here, we will only briefly summarize the key details. First, galvanotaxis occurs at field strengths far below that required to apply significant mechanical force to the cell bodies themselves. In other words, galvanotactic cues do NOT function by pulling or pushing on cells. However, the most likely explanation based on current data is that the field is strong enough to force the electrophoretic migration of several membrane components. As these are concentrated in a specific region of the membrane, such as the rear of the cell, they begin to affect signaling pathways, of which PI3K is one. These pathways, in turn, override the native migration cues. As a final reminder, it is not so much the magnitude of the electric field itself that matters, as it is the magnitude of the current density. This subtlety can be better understood by examining the equation that links field (*E,* Volts/distance) to current density (*J,* Amps/cross-sectional area, units of flux), as seen in Eqn. S1.

$$E = J\rho \tag{S1}$$

E and *J* are proportionally linked by 'ρ', which is the *resistivity* of the media in which the current is flowing. As over 99% of the current flows through the media rather than the cells (highly resistive relative to the media), we can assume that ρ is dictated by the properties of the media itself. The clearest experiment that confirms that *J*, rather than *E* is the key variable for galvanotaxis was shown in Allen et al. where they reduced salt levels (increasing ρ) while maintaining a constant field strength (decreasing *J*). The result was that the cells galvanotaxed more weakly, implying that *J*, rather than *E* is dominant parameter.

Chamber Design Parameters

Power Supply: Given the importance of *J,* we specifically opted to use a *current-controlled* power supply. This is less common than voltage controlled supplies. This scarcity, along with the subtlety about *E* vs. *J* may be why most galvanotaxis work uses voltage-controlled supplies and ignores the current density. In these cases, parameters such as media evaporation, electrode corrosion, or pH changes from cell metabolism can alter ρ, to which a voltage controlled supply will respond by varying *J.* In contrast, a current-controlled supply maintains a stable current (and fixed *J*) regardless of environmental fluctuations. Using a power supply with data I/O has the additional advantages of being able to program stimulation courses as well as constantly log and monitor the system voltage required to

drive the desired current. An increase in voltage indicates a rising ρ, and this can be used as an indicator of the need to change media or electrodes.

Chamber geometry: Eqn. S1 links the field to the current density, but these can also be linked to the geometry of the channel itself. Consider that *J,* current density, represents current/area, and that area comes from the cross sectional area of the chamber. This parameter is crucial for an efficient, predictable chamber for several reasons.

1. **Resistance vs. voltage drops:** When constructing our chambers, we created the highest resistance region directly around where the cells were cultured. We did this by using a 150 um-thick foundation layer on top of which we placed our acrylic frames (see Fig. 1). The frames contained reservoirs on either side that effectively increase the channel depth to many orders of magnitude higher than the depth of the enclosed channel in the center. From Ohm's law ($V = IR$), we know that the voltage drop across a resistor, for a constant current, scales with the resistance. We also know that all of the voltage must drop by the time the current returns to the power supply. Given this, if we have a resistance in the stimulation zone that is much higher than anywhere else in the system, we can drop the majority of the voltage through the stimulation zone (high efficiency). After the stimulation zone, the highest resistances occurred in the salt bridges themselves, and we took care to design these so that a minimum of 50% of the system voltage still dropped through the stimulation zone. This is important because lower system voltages produce electrochemical products more slowly and extend the life of the electrodes.

2. **Joule heating:** A troubling detail noted by Allen et al. is that many studies report increased migration speeds during galvanotaxis without controlling for temperature effects. By contrast, Allen et al. observed no increase in migration speed when they controlled against temperature variations. They attributed the discrepancy to Joule heating, a phenomenon they suspected had occurred in previous studies that would heat the cells and increase metabolic and migration rates. Anticipating this, we controlled and monitored thermal dissipation and do not believe it affected our data, as will be explained here.

   Simply put, Joule heating describes energy that is dissipated as heat when current flows through a conductor. The equation itself is relatively straightforward: $P = IV$, where P is power dissipated, and IV is current*voltage. This can be rewritten as $P = I^2R$, using Ohm's law, and now we see how resistance can affect Joule heating. R varies as $\rho\dfrac{L}{A}$, where ρ is the resistivity, L is the channel length, and A is the cross-sectional area. From this, we can see how varying the channel geometry can affect the thermal dissipation into the system. This is a valid design concern, and one we addressed by directly measuring heating in our system during typical stimulation. To do this, we conducted a full trial on the microscope with our temperature control set to 37.5 °C in the incubation chamber. To detect Joule heating, we also embedded a micro-thermocouple directly into the center of the stimulation zone in a manner that did not disrupt flow but

would monitor the temperature in the stimulation zone. We used data acquisition tools to monitor this temperature and then activated the power supply. We observed no apparent heating of the channel when sweeping through the currents we used during our experiments. Monotonic increases in temperature occurred only at significantly higher currents than were used during experiments. As a secondary test, we can look at the data shown in Fig. 3, where we see that larger populations moved faster than smaller populations, despite both populations being within the same channel and distributed uniformly across the channel. This confirms that, even if Joule heating had occurred, the relative differences between large and small population migration dynamics still stand.

Chamber fabrication

All chambers were constructed similarly (as shown in Fig. 1). First, the chamber geometry was tuned by simulation (COMSOL) to achieve the desired electric field geometry. Once the geometry had been fine-tuned, a CAD file of the foundation tape layer was drawn (AutoCAD, Autodesk, Inc.). This file was then sent to a desktop computer-controlled cutter (Cameo, Silhouette, Inc.) and the design was cut into a 150 μm thick sheet of double-sided silicone adhesive with protective backing layers on either side (ARCare, Adhesive Research Global). One of the two backing layers was removed with forceps and the revealed adhesive surface was cemented to the center of a 100 mm tissue culture plastic Petri dish (BD Biosciences). To seed cell populations into the stimulation region of the chamber, a 250 μm thick silicone stencil (Bisco HT-6240, Stockwell Elastomers) was cut out and gently placed into the center of the stimulation region of the Petri dish. The silicone formed a reversible, watertight seal against the plastic substrate. Once bound, cells were pipetted into the stencil at a density sufficient to yield, by the time of the experiment, a final density of ~1500 cells/mm^2. Seeding dilutions were calculated such that 5 μL of media were added for every 5 mm^2 of area in the stencil. Additional hydration media was added around the periphery of the dish to maintain humidity in the dish. Standard populations (normal borders) were allowed to adhere to the substrate for 30 minutes, the stencil was removed, the cells bathed in additional media, and the ensemble incubated for 12-16 hrs. To inhibit leader cells, this same procedure was followed except that the stencil was not removed until immediately prior to the experiment. Once the cells had adhered and formed a fully junctioned monolayer, the media was aspirated, the remaining protective layer on the tape foundation was removed, and an acrylic frame (see Fig. 1) was affixed to the exposed adhesive, thus creating the full chamber. The acrylic frame was cut either by hand, milling machine, or laser cutter (we used a Versa 2.0, Universal Laser Inc.). Once assembled, media was added to hydrate the chamber and fill the reservoirs on either side. The dish was now ready to be mounted on the microscope and attached to the electrochemical system.